UNIVERSITÀ
DEGLI STUDI
DI PADOVA

Sede Amministrativa: Università degli Studi di Padova

Dipartimento di Ingegneria Industriale

SCUOLA DI DOTTORATO DI RICERCA IN: INGEGNERIA INDUSTRIALE
INDIRIZZO: FISICA TECNICA
CICLO: XXIV

Innovative Solutions For The Thermal Control Of Aeronautic Vehicles

Direttore della Scuola: Ch.mo Prof. PAOLO COLOMBO

Supervisore: Ch.mo Prof. CLAUDIO ZILIO

Dottorando: LUCA PATRICELLI

Abstract

The Environmental Control System and the anti-ice sub-system are two of the key energy consumers for an aircraft; they absorb together two times the sum of the power of all the other systems (electrical, mechanical and hydraulic). More efficient Environmental Control Systems and a more efficient anti-ice sub-systems would reduce the aircraft fuel consumption increasing the operative radius of the vehicle and also increasing the maximum useful load.

The anti-ice sub-system is not only a key energy consumer but it is also a system critical for the flight safety: a failure of this system means a mission abort and the landing on the nearest airport.

This thesis presents the results of several mathematical models which have been developed to study the performance of the aforementioned systems and the strategies to reduce their impacts on the aircraft fuel consumption. The models have been developed using AMEsim$^{®}$ and Simulink$^{®}$.

In particular a mathematical model, which describes the behavior of the inline pneumatic valves, have been created. The model uses the fundamental thermodynamic and mechanical differential equations to simulate the dynamic behavior of the valves. The mathematical model reproduces the results of the experimental tests within their uncertainty. The validated model has been used to explore the behavior of the valve and its own subcomponents proposing two possible solutions to increase the operative range of the valves and to decrease the influence of the pressure and temperature on the regulated pressure.

The second detailed mathematical model created calculates the performance of the plate and wavy fins compact heat exchangers. The model, based on the work of Kays and London [1984], includes some improvements related to the description heat exchanger geometry and related to the empirical correlations used to calculate the Stanton number. The tests performed on three different heat exchangers have been used to validated the developed model; the mathematical model is able to predict the performance of the performance of the heat exchangers with an accuracy compatible with most the industrial applications.

The developed detailed models have been used to simulate the behavior of the system where they are installed.

The behavior of an anti-ice system at extreme high bleed air temperature has been analyzed. An innovative architecture for anti-ice system is studied and the benefits on aircraft fuel consumption for a standard day mission are shown.

The performance of an reverse Brayton-Joule cycle has been analyzed and a new possible control strategy based on a line installed in series to the Air Cycle Machine is proposed. The limits of the proposed architecture are exposed studying the case of a system used to cool some electronic equipment. The benefits of the use of a reverse Brayton-Joule system which does not use the air bled from the engine (bleedless approach) are detailed with particular attention to the gain in terms of fuel penalty.

The thesis ends with the results of the Vapor Cycle System simulations. Some technical solutions to fit a fixed displacement compressor architecture into an aircraft are explained; the solutions are oriented to increase the reliability of the compressor avoiding a continuous switch on and off even with low heat loads. A variable displacement compressor improves the overall efficiency of the system on a full mission profile (high COP in the cruise phase). Two strategies, one for passenger compartments and one for electronic cooling, which are able to expand the working envelope (in terms of minimum heat load) of the variable displacement compressor architecture are proposed.

Keywords

ECS, aircraft, pneumatic valve, anti-ice system, fuel consumption, air cycle, vapor cycle, mathematical model

Sommario

I sistemi di controllo termico e i sistemi antighiaccio sono due delle utenze che assorbono maggiore energia su un aeroplano; questi due sistemi assorbono insieme due volte la somma di tutta la potenza assorbita dagli altri systemi (elettrico, meccanico ed idraulico). Dei sistemi di controllo termico ed antighiaccio più efficienti ridurrebbero il consumo specifico dell'aeroplano incrementandone il raggio operativo ed il massimo carico pagante.
Il sistema antighiaccio è inoltre anche un sistema critico per la sicurezza del volo: un suo guasto implica l'annullamento della missione e l'atterraggio nel più vicino aeroporto.
Questa tesi presenta i risultati di alcuni modelli matematici sviluppati per studiare le prestazione dei sistemi sopramenzionati e le strategie per ridurre i loro impatti sul consumo di carburante del velivolo. I modelli sono stati sviluppati utilizzando AMEsim® e Simulink®.
In particolare il modello matematico che descrive il comportamento delle valvole pneumatiche in linea è stato creato. Il modello usa le equazioni fondamentali della termodinamica e le equazioni differenziali della meccanica per simulare il comportamento delle valvole. Il modello matematico riproduce i risultati sperimentali all'interno della loro incertezza. Il modello, così validato, è usato per esplorare il comportamento delle valvole e dei loro sottocomponenti proponendo due possibili soluzioni per allargare il campo di utilizzo delle valvole e diminuire l'influenza della pressione e della temperatura sulla pressione regolata.
Il secondo modello di dettaglio creato calcola le prestazioni degli scambiatori compatti a piastre a alette ondulate. Il modello basato sul lavoro di Kays and London [1984] include alcuni miglioramenti relativi alla dscrizione geometrica degli scambiatori ed alle correlazioni empiriche utilizzate per calcolare il numero di Stanton. I tests eseguiti su tre differenti scambiatori sono stati utilizzati per validare il modello sviluppato; il modello matematico è capace di predire le prestazioni degli scambiatori con una accuratezza compatible con la maggioranza delle applicazioni industriali.
I modelli di dettaglio sviluppati sono stati utilizzati per simulare il comportamento dei sistemi dove sono installati.
Il comportamento di un sistema antighiaccio che opera a temperature estremamente alte è stato analizzato. Una architettura innovativa è proposta

ed i suoi benefici sul consumo di carburante in una missione standard sono presentati.
Le prestazioni di un ciclo inverso Brayton-Joule sono state analizzate ed è proposta una nuova possibile strategia di controllo basata su di una valvola installata in serie al compressore ed alla turbina. I limiti dell'architettura proposta sono esposti studiando il caso di un sistema utilizzato per raffreddare dell'equipaggiamento elettronico. I benefici dell'uso di un sistema Brayton-Joule inverso che non utilizza aria spillata dai motori (approccio bleedless) sono dettagliati con particolare attenzione al guadagno ottenuto sul consumo di carburante.
La tesi si conclude con i risultati delle simulazioni del sistema a compressione di vapore saturo. Alcune soluzioni tecniche per adattare un'architettura basata su di un compressore a cilindrata fissa sono spiegate; queste soluzioni sono orientate ad aumentare l'affidabilità del compressore evitando la continua accensione e spegnimento anche con bassi carichi termici. Un compressore a cilindrata variabile migliora l'efficienza globale del sistema sull'intero profilo di missione (alto COP nella fase di crociera). Due strategie, una per il compartimento passeggeri ed una per il raffreddamento dell'avionica, che ampiano l'inviluppo operativo (in termini di carico termico minimo) di un sistema equipaggiato con un compressore a cilindrata variable sono presentati.

Contents

List of Figures

List of Tables

Nomenclature

A Area, m^2

A_p Projected area, m^2

ACM Air Cycle Machine

alt Altitude, m

bbars HX blocking bars thickness ,m

c friction coefficient, $\mathrm{J\,m^{-1}}$

c_1 coefficient of viscous friction, $\mathrm{N\,m^{-1}\,s^{-1}}$

c_2 Coulomb friction force, N

c_3 stiction force, N

c_h specific heat, $\mathrm{J\,kg^{-1}\,K^{-1}}$

c_L latent heat, $\mathrm{J\,kg^{-1}}$

c_p Specific heat transfer at constant pressure, $\mathrm{J\,kg^{-1}\,K^{-1}}$

c_s Specific heat transfer, $\mathrm{J\,kg^{-1}\,K^{-1}}$

c_m orifice flow coefficient, $\mathrm{kg^{0.5}K^{0.5}J^{-0.5}}$

c_q orifice discharge coefficient

C_c heat exchanger capacity-rate ratio

COP Coefficient Of Performance

CRU Centralized Refrigerator Unit

d diameter, m

$d_{\mathbf{hyd}}$ hydraulic diameter, m

$d_{\mathbf{spring}}$ spring external diameter, m

$d_{\mathbf{wire}}$ spring wire diameter, m

DAIV DAIVDownstream Anti-Ice Valve

E electrical power, W

ECS Environmental Control System

EXV Electronic Expansion Valve

e_w skin emissivity, []

F force, N

F_a configuration factor, []

F_{up} Upstream pressure closure force, N

FMSOV Flow Modulating and Shut-Off Valve

$\boldsymbol{f_f}$ Fanning factor

fh HX passage heigh, m

fpi fin per inch (fin rate), in^{-1}

ft fin thickness, m

G material shear modulus, $\mathrm{N\,m^{-2}}$

G_s solar irradiance per unit of area, $\mathrm{W\,m^{-2}}$

h specific enthalpy, $\mathrm{J\,kg^{-1}}$

H enthalpy, J

HX heat exchanger

I electrical current, A

ISA International Standard Atmosphere

k spring rate, $\mathrm{N\,m^{-1}}$

$\hat{k}_t$ thermal conductivity, $\mathrm{W\,m^{-2}\,K^{-1}}$

J moment of inertia, $\mathrm{kg\,m^2}$

j Colburn factor, $j = \mathrm{StPr}^{\frac{2}{3}}$

L work, J

L/D Lift to drag ratio

L' work done by external forces, J

LC Length cold (HX), m

LH Length hot (HX), m

LNF Length no flow (HX), m

n polytropic index

$n_{\mathbf{coils}}$ number of spring active coils

m mass flow rate, $\mathrm{kg\,s^{-1}}$

$m_{\mathbf{corr}}$ corrected mass flow rate, $\mathrm{kg\,K^{0.5}\,s^{-1}\,kPa^{-1}}$

M mass, kg

Ma Mach number

$Npass$ HX number of passages (one side)

$N_{\mathbf{tu}}$ Number of heat transfer unit of a HX

OAP Outside Air Pressure, Pa

OAT Outside Air Temperature, K

P pressure, Pa

$P_{\mathbf{dyn}}$ dynamic pressure, Pa

PHX Primary Heat Exchanger

ppt HX parting plate thickness ,m

PET Pilot Envelope Temperature, °C

PRSOV Pressure Regulating & Shut-Off Valve

PRV Pressure Regulating Valve

q heat exchanged, W

Q heat, J

r radius, m

R specific gas constant, $\mathrm{J\,kg^{-1}\,K^{-1}}$

SH Superheating, °C

SHX Secondary Heat Exchanger

SFC_p Specific Fuel Consumption for power, $\mathrm{lb\,h^{-1}\,hp^{-1}}$

SFC_t Specific Fuel Consumption for thrust, $\mathrm{lb\,h^{-1}\,lb^{-1}}$

SOV Shut-Off Valve

t time, s

T temperature, K or °C

T_r recovery temperature, K or °C

TAS True Air Speed, kn

V volume, $\mathrm{m^3}$

$\dot{V}$ volumetric flow rate, $\mathrm{m^3\,s^{-1}}$

$\vec{v}$ Fluid speed, $\mathrm{m\,s^{-1}}$

W work, W

$W_{\mathbf{f,0}}$ Take-off fuel weight penalty, lb

WBGT Wet Bulb Globe Temperature, °C

U internal energy, J

$\hat{U}$ overall heat transfer coefficient, $\mathrm{Wm^{-2}K^{-1}}$

UAIV Upstream Anti-Ice Valve

VCS Vapor Cycle System

x linear displacement, m

Greek symbols

α angle, °

α_L coefficient of linear thermal expansion, $\mathrm{°C^{-1}}$

$\hat{\alpha}$ thermal-convection heat transfer coefficient, $\mathrm{Wm^{-2}K^{-1}}$

β Pressure ratio

$\Delta_{\mathbf{ISA}}$ Variation respect to ISA, °C

ϵ heat exchanger effectiveness

γ specific heat ratio

φ relative humidity, %

δ measurement uncertainty

$\eta_{\mathbf{fin}}$ efficiency of the fins

κ heat exchange coefficient, $\mathrm{WK^{-1}m^{-2}}$

μ viscosity, $\mathrm{Nm^{-2}s}$

ρ fluid density, $\mathrm{kg\,m^{-3}}$

τ torque, $\mathrm{N\,m}$

$\hat{\tau}$ Overall solar transmissivity of transparent areas, []

ω rotary speed, $\mathrm{rad\,s^{-1}}$

Ξ engine throttle, %

χ specific humidity, $\mathrm{kg_{water}kg^{-1}{}_{air}}$

Subscripts

amb external ambient condition

bleed air bled from the engine

co compression

cold HX cold fluid

cpt compartment

dry referred to a transformation with no humidity

el electrical

ex expansion

fl flight

hot HX hot fluid

iso isentropic process

LE engine Leading Edge

ref reference or standard conditions

sat referred to saturation conditions

skin aircraft external surface

wet referred to a transformation with humidity

Physic Constants

σ Stefan Boltzmann constant, $5.6704\mathrm{e}{-8}\,\mathrm{W\,m^{-2}\,K^{-4}}$

Nu Nusselt number, $\mathrm{Nu} = \frac{\hat{\alpha} d_{\mathrm{hyd}}}{\hat{k}_t}$

Pr Prandtl number, $\mathrm{Pr} = \frac{\mu c_p}{\hat{k}_t}$

Re Reynold number, $\mathrm{Re} = \frac{4 d_{\mathrm{hyd}} m}{A \mu}$

St Stanton number, $\mathrm{St} = \frac{A \hat{\alpha}}{c_p m}$

Chapter 1

Pneumatic valves

1.1 Introduction

Pneumatic valves are used on aircraft mainly to control the flow rate of the air bled by the engines and to modulate it.
The valves can be divided in two main categories:

- External powered valves
- Internal powered valves

The *external powered valves* utilize the electrical current to generate the actuating force. Motor valves and solenoid valves belong to this category. These valves are the preferred to create the control loop of the systems.
The *internal powered valves* utilize the air pressure to generate the motion force. Relief valves and in-line valves belong to this category. This category is used when the valve is critical for flight safety.

1.1.1 Pneumatic volume

All the pneumatic systems to be described need the use of variable or fixed volumes.
Equation (1.1.1) is one of the form of real gas state equation.

$$\rho = f(P, T, R) \tag{1.1.1}$$

The evolution of the gas state in the time is fully described if pressure (P) and temperature (T) evolutions in the time are described, so a system of two partial differential equations has to be solved (under the hypothesis that the gas does not change its property during the time).
The first equation is the law of conservation of mass applied to a generic variable volume (V) with jj mass flow rate (m). Equation 1.1.2 is the mass

balance of the V (the mass (M) inside the volume is $V\rho$).

$$V\frac{d\rho}{dt} + \rho\frac{dV}{dt} = \sum_{\text{jj}} m_{\text{jj}} \tag{1.1.2}$$

The time derivative of the fluid density (ρ) with respect to the time is written as shown in equation 1.1.3.

$$\frac{d\rho}{dt} = \frac{\partial\rho}{\partial P}\frac{dP}{dt}\bigg|_T + \frac{\partial\rho}{\partial T}\frac{dT}{dt}\bigg|_P \tag{1.1.3}$$

The partial derivatives of ρ with respect to the P and T depend on the fluid model selected. If the hypothesis of ideal gas is used, they are easily calculated (see equation 1.1.4a and 1.1.4b);

$$\frac{\partial\rho}{\partial P}\bigg|_T = \frac{1}{RT} \tag{1.1.4a}$$

$$\frac{\partial\rho}{\partial T}\bigg|_P = -\frac{P}{RT^2} \tag{1.1.4b}$$

In the cases where the ideal gas approximation is not applicable, the results of those two partial differential equations are calculated using external models (like *REFPROP*® Lemmon et al. [2010]).
The final form of the of the mass balance for V is obtained introducing equation 1.1.3 into equation 1.1.2.

$$V\,\frac{\partial\rho}{\partial P}\frac{dP}{dt}\bigg|_T + V\,\frac{\partial\rho}{\partial T}\frac{dT}{dt}\bigg|_P = \sum_{\text{jj}} m_{\text{jj}} - \rho\frac{dV}{dt} \tag{1.1.5}$$

The second equation is the first law of the thermodynamic applied to V.

$$\frac{dU}{dt} = \frac{dQ}{dt} + \frac{dL}{dt} + \sum_{\text{jj}} m_{\text{jj}}(h_{\text{jj}} - h_V) \tag{1.1.6}$$

The internal energy (U) is defined as shown in equation 1.1.7a, and the work (L) is the sum of the work done by external forces (L') and the expansion/compression work.

$$U = H - pV \tag{1.1.7a}$$

$$\frac{dL}{dt} = \frac{dL'}{dt} - P\frac{dV}{dt} \tag{1.1.7b}$$

$$\Delta h_{\text{jj}} = h_{\text{jj}} - h_V \tag{1.1.7c}$$

The specific enthalpy (h) is the enthalpy (H) per unit of mass. The time derivative of h with respect to the time is written as function of P and T.

$$\frac{dh}{dt} = \frac{\partial h}{\partial P}\bigg|_T\frac{dP}{dt} + \frac{\partial h}{\partial T}\bigg|_P\frac{dT}{dt} \tag{1.1.8}$$

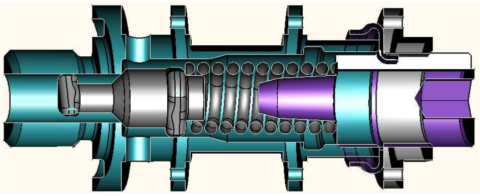

Figure 1.1: Relief valve cut-off view

The final form of the first law of thermodynamic for the volume V, is obtained introducing equations 1.1.8 and 1.1.7 into equation 1.1.6 and simplifying the equation.

$$\left(M \left. \frac{\partial h}{\partial P} \right|_T - V \right) \frac{dP}{dt} + M \left. \frac{\partial h}{\partial T} \right|_P \frac{dT}{dt} = \frac{dQ}{dt} + \frac{dL'}{dt} + \sum_{\mathrm{jj}} m_{\mathrm{jj}} \Delta h_{\mathrm{jj}} \tag{1.1.9}$$

The evolution of P and T inside V is calculated solving the system of equation 1.1.5 and 1.1.9.

1.2 Relief valve

The relief is a valve which keeps the pressure inside a chamber lower than a threshold value. Figure 1.1 shows a relief valve cut off view.
The valve is made by a plunger (generally it has a conical shape), by a body (which drives the plunger and contains also the spring), by a spring (which generates the force opposite to the pressure force) and by an adjustable nut used to set the cracking point of the valve, increasing or decreasing the pre-load on the spring.
The working principle of the valve is very easy. The spring keeps the plunger into the closed position as soon as the pressure on the other side is not sufficiently high to win the spring force and push the plunger to open. The plunger opening creates a flow rate from the chamber to the ambient; if the chamber is constantly supplied with pressurized fluid, the relief valve stays open into an equilibrium position, regulating the pressure inside the chamber, otherwise when the pressure goes below the relief valve cracking point, the valve closes.

1.2.1 Mathematical model

Flowing area

The relief valve under analysis uses a conical poppet, figure 1.2 is the sketch of the configuration under analysis. Equations (1.2.1) are derived from simple geometrical considerations (see Andersen [2001]).

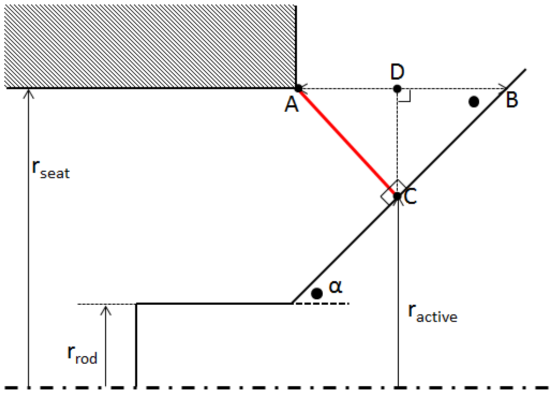

Figure 1.2: Conical poppet, geometrical data

$$\left.\begin{array}{r}\overline{AB} = x \\ A\widehat{B}C = \alpha\end{array}\right\} \Rightarrow \left\{\begin{array}{l}\overline{AC} = x\sin\alpha \\ \overline{BC} = x\cos\alpha\end{array}\right. \tag{1.2.1a}$$

$$\overline{DC} = \overline{BC}\sin\alpha = x\cos\alpha\sin\alpha \tag{1.2.1b}$$

$$A_{\text{lateral frustum}} = \pi\overline{AC}(r_{\text{seat}} + r_{\text{active}}) \tag{1.2.1c}$$

$$d_{\text{active}} = 2(r_{\text{seat}} - \overline{DC}) = d_{\text{seat}} - 2x\sin\alpha\cos\alpha \tag{1.2.1d}$$

The flow area depends on the x. If the poppet is too far from the seat edge ($d_{\text{active}} \leq d_{\text{rod}}$), the frustum of cone degenerates in cylinder and the flow area is the annulus formed by d_{seat} and d_{rod}, otherwise the flow area is the lateral surface area of the frustum of cone having as slant height the distance from the poppet surface to the seat edge corner. The d_{active} is the diameter corresponds to the minor base of the frustum of cone (see equation 1.2.1d). The formula 1.2.2 to calculate the flow area is obtained from equations 1.2.1 and is valid if $0° \leq \alpha \leq 90°$.

$$A = \begin{cases} \pi x\sin\alpha(d_{\text{seat}} - x\sin\alpha\cos\alpha) & \Leftarrow x \leq \dfrac{d_{\text{seat}} - d_{\text{rod}}}{2\sin\alpha\cos\alpha} \\ \\ \dfrac{\pi}{4}\left(d_{\text{seat}} - d_{\text{rod}}\right) & \Leftarrow x > \dfrac{d_{\text{seat}} - d_{\text{rod}}}{2\sin\alpha\cos\alpha} \end{cases} \tag{1.2.2}$$

Equation (1.2.3) is the formula to calculate the flow through an orifice (see Bertin [2002]). T_1 and P_1 are the temperature and pressure before the throat, T_2 and P_2 are the conditions after the throat.

$$m_{12} = A_{12}C_qC_m\frac{P_1}{\sqrt{T_1}} \tag{1.2.3}$$

The orifice discharge coefficient (c_q) is a coefficient used to take into account the vena contraction due to the abrupt area change at the entrance of the section (Andersen [2001] suggests to use value between 0.72 and 0.87 for

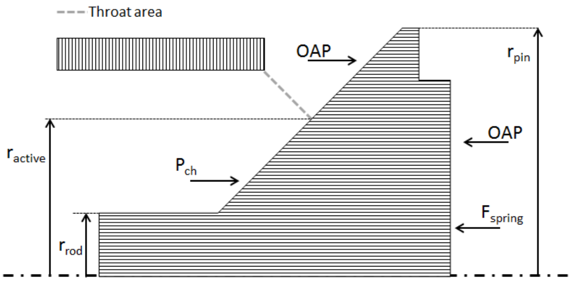

Figure 1.3: Force analysis on the relief valve pin

conical poppets); orifice flow coefficient (c_m) is calculated using equation (1.2.4): the first equation is used when the flow is subsonic, the second one when the flow is supersonic.

$$c_m = \begin{cases} \left(\frac{2\gamma}{(\gamma-1)R} \left(\left(\frac{P_2}{P_1}\right)^{\frac{2}{\gamma}} - \left(\frac{P_2}{P_1}\right)^{\frac{\gamma+1}{\gamma}} \right) \right)^{\frac{1}{2}} & \text{if } \frac{P_2}{P_1} > \left(\frac{2}{\gamma+1}\right)^{\frac{\gamma}{\gamma-1}} \\ \left(\frac{\gamma}{R} \left(\frac{2}{\gamma+1}\right)^{\frac{\gamma+1}{\gamma-1}} \right)^{\frac{1}{2}} & \text{if } \frac{P_2}{P_1} \leq \left(\frac{2}{\gamma+1}\right)^{\frac{\gamma}{\gamma-1}} \end{cases} \tag{1.2.4}$$

Plunger movement equation

The relief plunger moves following the equations of motion (1.2.5).

$$M\frac{d^2x}{dt^2} + c\frac{dx}{dt} = F(t) \tag{1.2.5}$$

The force (F) acts on the plunger it is divided into:

- spring force (F_{spring})
- pressure forces ($F_{\text{pressures}}$)
- external forces (F_{external})

F_{external} includes all the forces due to external accelerations (i.e gravitational force, airplane vibrations, airplane manoeuvres, etc.); the influence of these forces is neglected ($F_{\text{external}} = 0$).

The spring force is proportional to plunger stroke x. x_0 is the difference between the spring free length and the working spring length (when no other forces are applied), hence the product kx_0 is the spring pre-load.

$$F_{\text{spring}} = k(x - x_0) \tag{1.2.6}$$

Two pressures act on the pin surfaces: the Outside Air Pressure (OAP) and P_{ch} (the pressure of the pressurized chamber). The P_{ch} acts on the pin

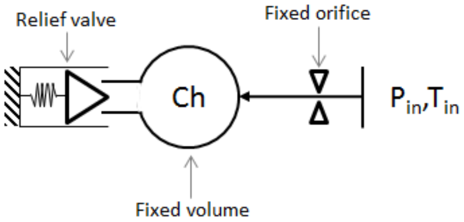

Figure 1.4: Relief valve mathematical model and test rig schematic

surface before the throat area, OAP acts on all the pin surface after the throat area[1].

$$F_{\text{pressures}} = \frac{\pi d_{\text{active}}^2}{4} \left(P_{\text{ch}} - OAP\right) \tag{1.2.7}$$

The throat area shifts on the pin surface following x, when d_{active} becomes smaller than d_{rod} the area where either OAP and P_{ch} act is the circle area defined by d_{rod} otherwise is the circle area defined by d_{active}.

$$d_{\text{active}} = \begin{cases} d_{\text{rod}} & \Leftarrow x > \dfrac{d_{\text{seat}} - d_{\text{rod}}}{2\sin\alpha\cos\alpha} \\ \\ d_{\text{seat}} - 2x\sin\alpha\cos\alpha & \Leftarrow x \leq \dfrac{d_{\text{seat}} - d_{\text{rod}}}{2\sin\alpha\cos\alpha} \end{cases} \tag{1.2.8}$$

Equation 1.2.9 is the formula to calculate F for a relief valve (see equations 1.2.6 and 1.2.7).

$$F(t) = \underbrace{k(x - x_0)}_{F_{\text{spring}}} + \underbrace{\frac{\pi d_{\text{active}}^2}{4} \left(P_{\text{ch}} - OAP\right)}_{F_{\text{pressures}}} \tag{1.2.9}$$

The x_0 is used to set the valve cracking point; this value is set by the operators acting on the valve nut, during the valve acceptance tests. The spring force decreases increasing x_0 (so un-screwing the nut) and the relief valve cracking pressure decreases. An active control valve could be created simply connecting a step motor to the nut: the motor controls the relief valve cracking point modifying x_0.

0d model

The equations here above detailed have been used to create a 0d model of a relief valve. Figure 1.4 shows the sketch of the model created. It simulates an ideal air pressure and temperature source; the gas flows through an calibrated orifice into a fixed volume (see paragraph 1.1.1 and equation

---

[1] under the hypothesis that all the pressure drops are concentrated in the throat area

Parameter	Unit	Value
Plunger M	g	1.05
V	dm^3	0.1
spring rate (k) at 20 °C	$\mathrm{N\,m^{-1}}$	7650.0
Fixed orifice d	mm	0.8
d_{rod}	mm	3.0
d_{seat}	mm	5.0
α	°	45.0
x_0	mm	1.18
T_{air}	K	298.15
$c_{\mathrm{q,fix}}$		0.8
$c_{\mathrm{q,pin}}$		0.72

Table 1.1: Relief valve model main parameter

Parameter	Unit	Value
P_{ch}	kPa	101.3
T_{ch}	K	298.15
v_{plunger}	$\mathrm{m\,s^{-1}}$	0.0
x_{plunger}	mm	0.0

Table 1.2: Relief valve model, initial simulation conditions

(1.2.3)). The pressure inside the volume is controlled by a relief valve. Table 1.1 summarizes the main parameters, and table 1.2 reports the initial conditions of the simulations.

The simulations have been performed varying the value of P_{in} from 101.3 kPa to 2500 kPa and waiting the achievement of steady state conditions.

1.2.2 Model results analysis

The simulation at $P_{\mathrm{in}} = 1000\,\mathrm{kPa}$ is analyzed to describe the behavior of the valve in unsteady conditions.

The pressure difference across the fixed orifice ($P_{\mathrm{in}} - P_{\mathrm{ch}}$) creates an inlet air flow rate to the chamber ($m_{\mathrm{ch,in}}$). The inlet flow rate is not equalized by an outlet flow rate from the chamber ($m_{\mathrm{ch,out}}$) in the first part of the simulation (figure 1.5(b)) since the relief plunger is closed ($x_{\mathrm{plunger}} = 0$). That flow rate lack of balance causes the increase of P_{ch} (figure 1.5(a)).

The plunger does not move until the P_{ch} is not sufficiently high to win F_{spring} (figure 1.5(d)); as soon as $F_{\mathrm{pressures}} > F_{\mathrm{spring}}$ (around $t = 0.4\,\mathrm{s}$) the plunger moves (figure 1.5(c)) and the air starts to flow out from the chamber. The plunger opening creates a small unbalancing of the forces $F_{\mathrm{pressures}} < F_{\mathrm{spring}}$

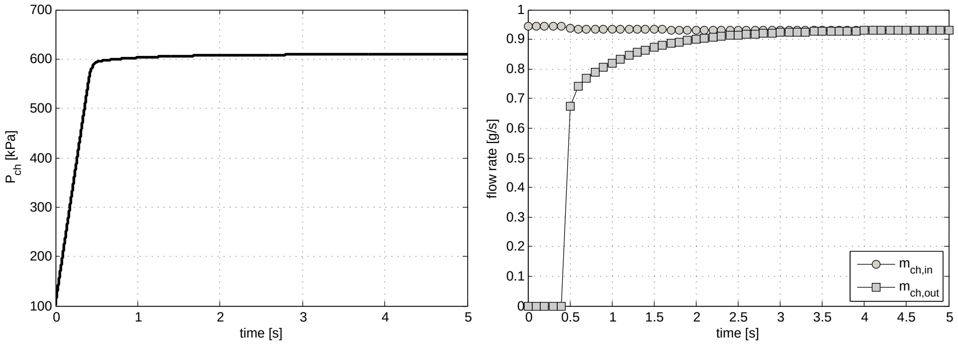

(a) P_{ch} **(b)** chamber inlet and outlet flow rates

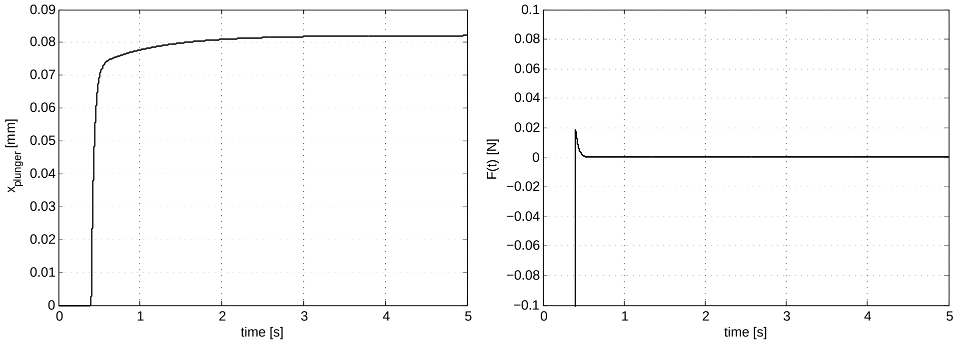

(c) plunger stroke **(d)** $F_{\mathrm{pressures}} - F_{\mathrm{spring}}$

Figure 1.5: Relief valve model. Analysis of dynamic behavior at $P_{in} = 1000\,\mathrm{kPa}$

which stops the plunger stroke into the equilibrium position.
The derivative of P_{ch} with respect to the time decreases as soon as $m_{\mathrm{ch,out}} > 0$ and became 0 when $m_{\mathrm{ch,out}} = m_{\mathrm{ch,in}}$ (steady state conditions).
Figure 1.6(a) shows the trend of P_{ch} at all simulated P_{in}. The time to reach the steady state conditions depends on the P_{in}. The flow rate which enters inside the chamber at high P_{in} is bigger than at low P_{in} (see equation 1.2.3), $\frac{dP_{\mathrm{ch}}}{dt}$ is proportional to $m_{\mathrm{ch,in}} - m_{\mathrm{ch,out}}$ (note that $m_{\mathrm{ch,out}} = 0$ in the first part of the simulation), so the P_{ch} rises faster at high P_{in} than at low P_{in}.
Figure 1.6(a) shows also that the P_{ch} at steady state conditions increases as P_{in} increases. Figure 1.6(b) shows this trend for steady state conditions.
The chamber inlet and outlet flow rates are calculated applying equation 1.2.3.

$$m_{\mathrm{ch,in}} = A_{\mathrm{fix}} c_{\mathrm{q,fix}} c_{\mathrm{m,fix}} \frac{P_{\mathrm{in}}}{\sqrt{T}} \tag{1.2.10a}$$

$$m_{\mathrm{ch,out}} = A_{\mathrm{pin}} c_{\mathrm{q,pin}} c_{\mathrm{m,pin}} \frac{P_{\mathrm{ch}}}{\sqrt{T}} \tag{1.2.10b}$$

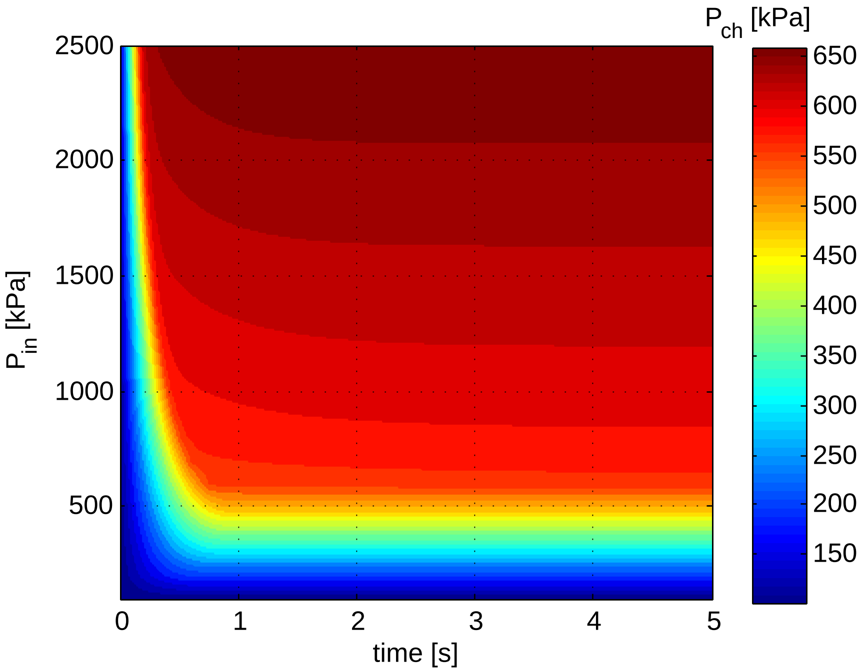

(a) P_{ch} time trend at various P_{in}

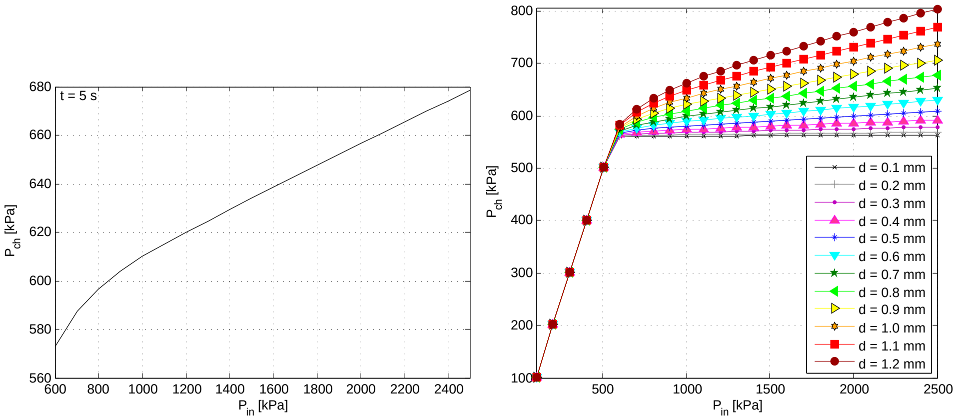

(b) $P_{\text{ch}} = f(P_{\text{in}})$ at t=5 s

(c) fixed orifice dimension influence

Figure 1.6: Relief valve model. P_{ch} time trend at various P_{in}

In steady state conditions $m_{\text{ch,in}} = m_{\text{ch,out}}$, so merging equations 1.2.10a 1.2.10b equation 1.2.11 is obtained.

$$P_{\text{ch}} = \underbrace{\frac{A_{\text{fix}} c_{\text{q,fix}} c_{\text{m,fix}}}{A_{\text{pin}} c_{\text{q,pin}} c_{\text{m,pin}}}}_{\text{curve slope}} P_{\text{in}} \tag{1.2.11}$$

Equation 1.2.11 shows that the increase of P_{ch} as P_{in} increases is the normal behavior for a chamber having 2 orifices in series. In the case one of these 2 orifices is a relief valve (so a variable area) the equation is implicit (A_{pin} is a function of P_{ch}).

The change of the fixed orifice area has a strong influence on the slope of the curve (see figure 1.6(c)). As predicted by equation 1.2.11 decreasing the fixed orifice diameter the slope of the curve tends to zero, otherwise increasing the diameter of the fixed orifice the slope increases. The selection of the fixed orifice diameter is a compromise between valve time response (small diameter means longer time response) and the variation of the regulated pressure with respect to the inlet pressure.

1.2.3 Temperature influence of relief valve working point

The temperature has a great influence on the behavior of a relief valve, since it changes the spring rate.

The k is calculated from the geometrical (d_{spring}, d_{wire}, n_{coils}) and material (G) properties of a spring using equation 1.2.12.

$$k = \frac{G d_{\text{wire}}^4}{8 d_{\text{spring}}^3 n_{\text{coils}}} \tag{1.2.12}$$

All the parameters of equation 1.2.12 are influenced by the temperature except the number of spring active coils (n_{coils}). The change of diameter (δd) and material shear modulus (δG) with respect to the temperature are calculated using equation 1.2.13, where T_0 is the reference temperature (generally room temperature) and α_L is the coefficient of linear thermal expansion for the spring material.

$$\delta d = \alpha_L (T - T_0) d_{T_0} \tag{1.2.13a}$$

$$\alpha_G = \frac{G_{T \neq T_0}}{G_{T_0}} \tag{1.2.13b}$$

$$\delta G = \alpha_G G_{T_0} \tag{1.2.13c}$$

The variation of k with respect to the temperature is obtained combining equation 1.2.12 and 1.2.13.

$$k(T) = \frac{G_{T_0} d_{\text{wire},T_0}^4}{8 d_{\text{spring},T_0}^3 n_{\text{coils}}} \alpha_G (1 + \alpha_L (T - T_0)) \tag{1.2.14}$$

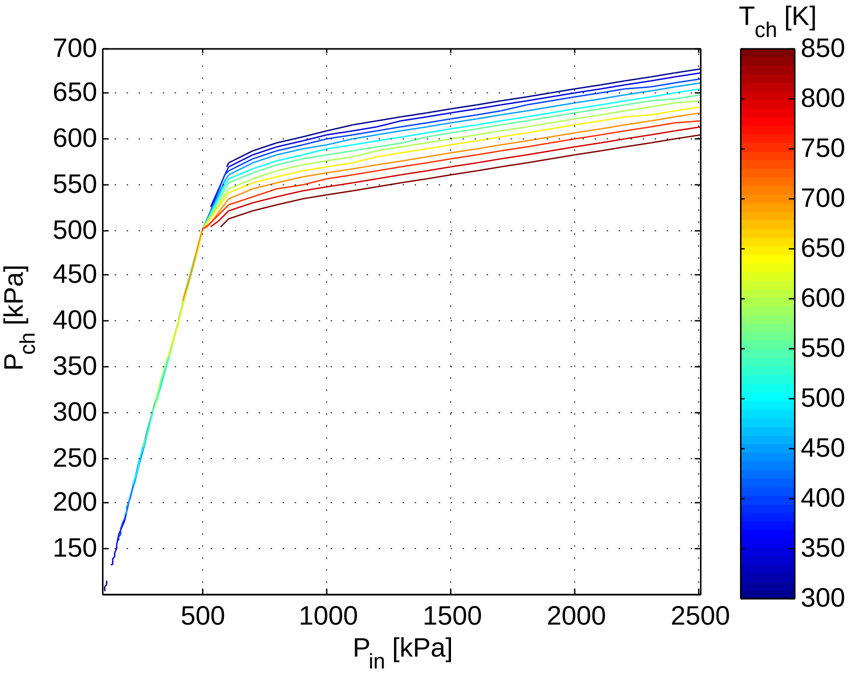

Figure 1.7: Effects of the bleed air temperature on relief valve

The product $\alpha_L(T - T_0)$ has an order of magnitude of 1e$-$3 for Inconel alloy[2], so its influence on k is negligible. On the other hand α_G change dramatically with respect to the temperature[3]. The final form to calculate k at various temperatures (equation (1.2.15)) is obtained introducing the above consideration into equation (1.2.14).

$$k(T) = k(T_0) \quad \alpha_G(T) \tag{1.2.15}$$

The mathematical model of the relief valve has been refined introducing the influence of the bleed air temperature on k. The hypothesis that the temperature of the spring is equal to the temperature inside the chamber drives this additional feature. The model assumes that the temperature has the same effects either on material shear modulus (G) and on the tensile yield strength.

Several simulations were run at different temperatures (T_{ch}), figure 1.7 shows the results of these simulations.

The relief valve cracking point shifts to lower values with the increase of the temperature. In fact in steady state conditions $F_{\text{pressures}}$ is equal to F_{spring}.

---

[2] i.e. Inconel X718 has a coefficient of linear thermal expansion (α_L) of 4.615e$-$6 °C^{-1}, so considering a ΔT of 600 °C the product $\alpha_L(T - T_0)$ is equal to 0.0028

[3] i.e. for Inconel X718 $G_{600\,°\mathrm{C}} = 0.8 G_{20\,°\mathrm{C}}$

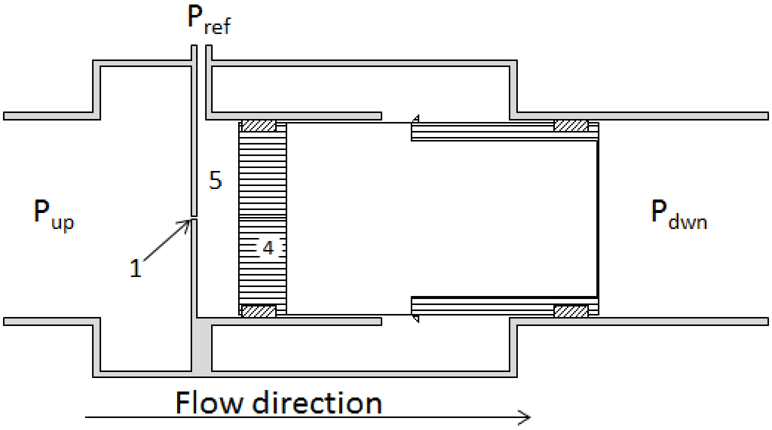

Figure 1.8: PRSOV cut off view.(1) control orifice, (2) relief valve, (4) main piston, (5) reference chamber

So the P_{ch} is:

$$P_{\text{ch}} = \frac{4}{\pi d_{\text{throat}}^2} k(x - x_0) + OAP \tag{1.2.16}$$

k decreases with the increase of the temperature and thus the pressure inside the chamber, in steady state conditions, decreases.
Figure 1.7 shows also as the temperature does not affect the influence of P_{in} on P_{ch} (previously discussed): the slope of the curves do not change with the respect of the temperature.

1.3 In-line valve

Figure 1.8 shows the sectional view of an in-line valve.
Valve consists of the following main parts: control orifice (1), reference chamber (2), and main piston (3). When the reference chamber is vented to ambient the resulting force that acts on the main piston keeps it into closed position.
The piston goes to open position when the reference chamber is pressurized. If the pressure inside the reference chamber (P_{ch}) is lower than the valve inlet pressure (P_{up}) the main piston is pushed into a regulating position (somewhere between full open and full close position), the position of the piston is such that the P_{ch} is equal to the pressure downstream the valve (P_{down}). When $P_{\text{ch}} \geq P_{\text{up}}$ the piston is pushed to go into full open position.
In-line valve architecture is very flexible, and various valve configuration can be arranged. A Shut-Off Valve (SOV) is obtained installing a shut-off solenoid to pressurize or vent the reference chamber; if a relief valve is added to a SOV, in order to limit the pressure inside the reference cham-

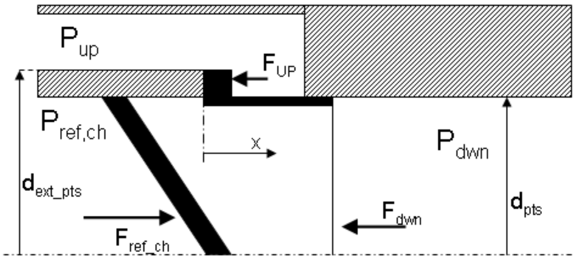

Figure 1.9: Force analysis on the valve main piston

ber, the valve becomes a PRSOV; substituting the shut-off solenoid with a proportional solenoid, the valve is a Pressure Regulating Valve (PRV).

1.3.1 Mathematical model

The reference chamber pressure and the downstream pressure (P_{dwn}) act on the same area of the piston creating two opposite forces ($F_{\text{ref,ch}}$ and F_{dwn}). The upstream pressure (P_{up}) acts on an annulus to keep the piston in closed position when the valve is commanded closed. Gravitational forces and aerodynamic forces are neglected.
The resulting force is:

$$F_{\text{net,pts}} = (P_{\text{ref,ch}} - P_{\text{dwn}})\frac{\pi}{4}d^2_{\text{pst}} - \frac{\pi}{4}P_{\text{up}}(d^2_{\text{ext,pst}} - d^2_{\text{pst}}) - F_{\text{up}} \tag{1.3.1}$$

F_{up} is a force generated by a small step (see Figure 1.10) on the piston and it is used to keep closed the piston. On this step the upstream pressure pushes to keep closed the piston creating a force opposite to the one generated by the pressure inside the reference chamber. F_{up} is calculated using equation (1.3.2).

$$F_{\text{up}} = \begin{cases} 0 & \text{if } \Theta > \Upsilon \\ \frac{\pi}{4}(P_{\text{up}} - P_{\text{dwn}})((d_{\text{ext,pts}} - \Theta)^2 - d^2_{\text{pts}}) & \text{if } \Theta \leq \Upsilon \end{cases} \tag{1.3.2}$$

Where:

$$\Theta = 2x\cos\alpha\sin\alpha \tag{1.3.3a}$$

$$\Upsilon = d_{\text{ext,pts}} - d_{\text{pts}} \tag{1.3.3b}$$

The piston slides on the valve body on two carbon O-rings to decrease either the friction forces and the internal leakage of the valve (leakage mainly between the reference chamber and the valve downstream region). Several models have been developed for control valve friction (see Garcia [2008] for an overview of the main models). In this case, since no data is available to create a detailed model, the friction phenomena has been simulated dividing it into 3 different aspects:

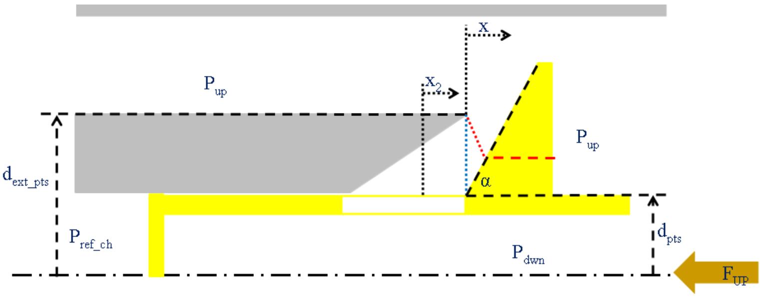

Figure 1.10: Magnification of where F_{up} is generated

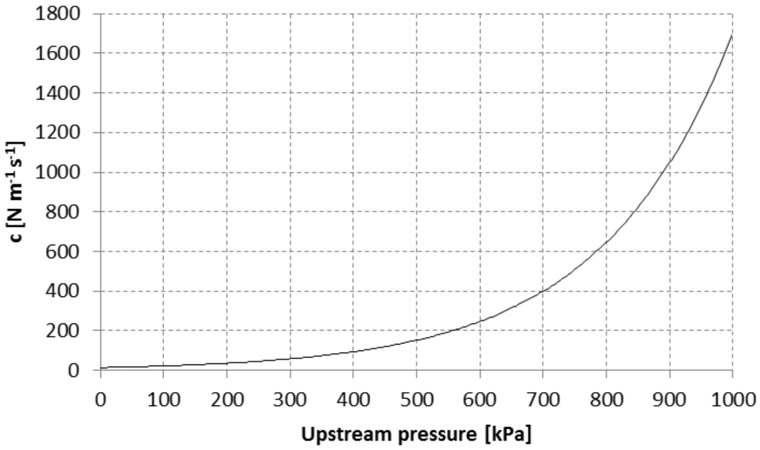

Figure 1.11: Viscous friction factor trend respect to upstream pressure

- Coulomb friction force
- Stiction friction force
- Viscous friction

The first two are constant the last one (viscous friction) is a function either of the piston speed and of the upstream pressure (since higher pressure means more force pushing the seals against the valve body surface, see Figure 1.11). Therefore main piston move equation is:

$$\begin{cases} M_{\text{pts}} \frac{d^2x}{dt^2} + c_2 \frac{dx}{dt} = F_{\text{net,pts}} - \text{sgn}\left(\frac{dx}{dt}\right) c_1 & \text{if } F_{\text{net,pts}} < c_3 \\ \frac{dx}{dt} = 0 & \text{if } F_{\text{net,pts}} \geq c_3 \end{cases} \tag{1.3.4}$$

End stops

Equations (1.2.5) and (1.3.4) do not consider the finite stroke of the mass. There is a discontinuity into movement equation when the piston reaches either $x = 0$ or $x = x_{\max}$ due to the hammering of the movement part against the mechanical stops. This discontinuity is handled by equation (1.3.5).

$$\left.\begin{aligned} x(t-dt)&=0\\ \frac{dx}{dt}&\leq 0\\ \frac{d^2x}{dt^2}&\leq 0 \end{aligned}\right\} \Longrightarrow \begin{cases} x(t)=0\\ \dfrac{dx}{dt}=0\\ \dfrac{d^2x}{dt^2}=0 \end{cases} \tag{1.3.5}$$

Regulating area

The regulating area is the area through which the bleed air flows; it is a function of the piston stroke.
Due to the step which creates F_{up} (see Figure 1.10), the regulating area is calculated using equation (1.3.6).

$$A = \begin{cases} 0.5\Lambda(d_{\text{ext,pts}} + d_{\text{pts}})\sqrt{\left(x - \frac{\Upsilon}{2\tan\alpha}\right)^2 + \left(\frac{\Upsilon}{2}\right)^2} & \text{if } \Theta > \Upsilon \\ x\Lambda\sin\alpha(d_{\text{ext,pts}} - x\sin\alpha\cos\alpha) & \text{if } \Theta \leq \Upsilon \end{cases} \tag{1.3.6}$$

Λ is a coefficient which reduces the flow area taking into account the presence of the rays on the piston[4].

$$\Lambda = \pi - \frac{n_{\text{raz}} r_{\text{raz}}}{d_{\text{ext,pts}}} \tag{1.3.7}$$

Where n_{raz} and r_{raz} are respectively the number of the rays and the thickness of the rays.
The flow rate is computed using equation (1.2.3).
Equation (1.3.8) shows the formula assumed to calculate the c_q of the valve. The assumption is that the loss due to abrupt change of the flowing section increases linear with the distance of the position from the full closed position.

$$c_q = \frac{0.1 - 0.7}{x_{\max}} x + 0.7 \tag{1.3.8}$$

0d model

A 0d model has been created using the above equation. Figure 1.12 shows the sketch of the model created.
The model simulates an ideal gas source (P_{up}, T_{up}); two branches are connected to this source: a branch goes into a fixed orifice (A_1) which pressurizes the reference chamber variable volume (V_{ch}), the other branch goes into the variable orifice (A_2) which simulates the opening of the valve piston. The air flowed through the variable orifice enters into the downstream volume (V_{dwn}) and then is discharged into the ambient passing through an orifice

---

[4] Λ is an approximation, however it could be correct using an appropriate formula to c_q

Parameter	Unit	Value
Piston M	g	150
$d_{\mathrm{ext,pts}}$	mm	43.2
d_{pts}	mm	42.03
V_{dwn}	dm^3	3.5
α	°	60
$x_{\max}$	mm	12.25
A_1	mm^2	0.503
A_3	mm^2	254.5
A_4	mm^2	254.5
P_{amb}	kPa	101.3
T_{amb}	K	298.15
$c_{\mathrm{q,4}}$		0.8
r_{raz}	mm	5.0
n_{raz}		4.0

Table 1.3: In-line valve model main parameter

Parameter	Unit	Value
P_{ch}	kPa	101.3
T_{ch}	K	298.15
v_{piston}	$\mathrm{m\,s^{-1}}$	0.0
x_{piston}	mm	0.0
P_{dwn}	kPa	101.3
T_{dwn}	K	298.15
V_{ch}	m^3	0.0

Table 1.4: In-line valve model, initial simulation conditions

(A_4) which limits the maximum flow rate. The reference chamber is connected, thanks by a calibrated orifice (A_3) to an ideal gas sources (P_{ref}, T_{ref}).

The simulations have been performed for P_{up} from 101.3 kPa to 1000 kPa, and for P_{ref} from 200 kPa to 700 kPa. The temperature of the ideal sources has been kept constant at 298.15 K.

1.3.2 Mathematical model results

Steady state simulations

Figure 1.13 shows the steady state behavior of a in-line valve at different P_{up} and P_{ref}. The valve piston remains in full open position ($x = x_{\max}$) when the inlet pressure is lower than the reference chamber pressure. In

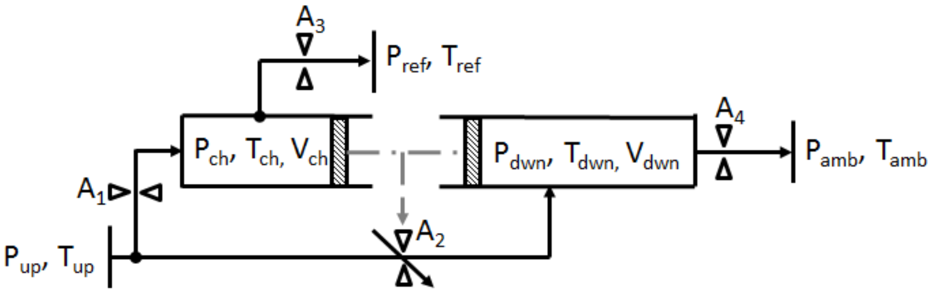

Figure 1.12: In-line valve model schematic

these cases the pressure downstream the valve is simple set by the pressure drop across the valve. At higher inlet pressure the valve starts to limit the downstream pressure.
Figure 1.13(b) shows how the transition from full open position to regulating position is abrupt, in fact the piston moves from 12.25 mm to 4 mm for a P_{up} variation of less than 100 kPa.
It is useful define the equivalent diameter (d_{eq}), to better understand the reason of this behavior; the equivalent diameter is the diameter of the circular orifice having the same area of the valve[5] (see equation (1.3.9)).

$$d_{\mathrm{eq}} = \sqrt{\frac{4}{\pi}A} \tag{1.3.9}$$

$$A_2 c_{\mathrm{q},2} c_{\mathrm{m},2} \frac{P\mathrm{up}}{\sqrt{T\mathrm{up}}} = A_4 c_{\mathrm{q},4} c_{\mathrm{m},4} \frac{P\mathrm{dwn}}{\sqrt{T\mathrm{dwn}}} \tag{1.3.10}$$

The equivalent diameter of the valve is calculated rearranging equation (1.3.10), assuming that $T_{\mathrm{up}} = T_{\mathrm{dwn}}$, and imposing that $\frac{P_{\mathrm{dwn}}}{P_{\mathrm{up}}} \leq 0.528$ and $\frac{P_{\mathrm{amb}}}{P_{\mathrm{dwn}}} \leq 0.528$[6].

$$d_{\mathrm{eq}} = d_4 \sqrt{\frac{P_{\mathrm{dwn}}}{P_{\mathrm{up}}} \frac{c_{\mathrm{q},4}}{c_{\mathrm{q},2}}} \tag{1.3.11}$$

Equation (1.3.11) shows that the valve equivalent orifice has to be smaller than the downstream orifice, when the valve has to limit the pressure. The valve has an equivalent orifice similar to the downstream orifice when the piston stroke is less than 3 mm (see figure 1.14), this is the reason why the transition from full open position to regulating position is so abrupt.
A different shape of the piston openings creates a smoother transition. The rectangular openings have the advantage of maximize the flow area when the valve is fully open, thus reducing the pressure drop of the valve in this

---

[5] to calculate the flow rate, the orifice has to have the same c_q of the valve
[6] Orifice are considered sonic, see equation (1.2.4)

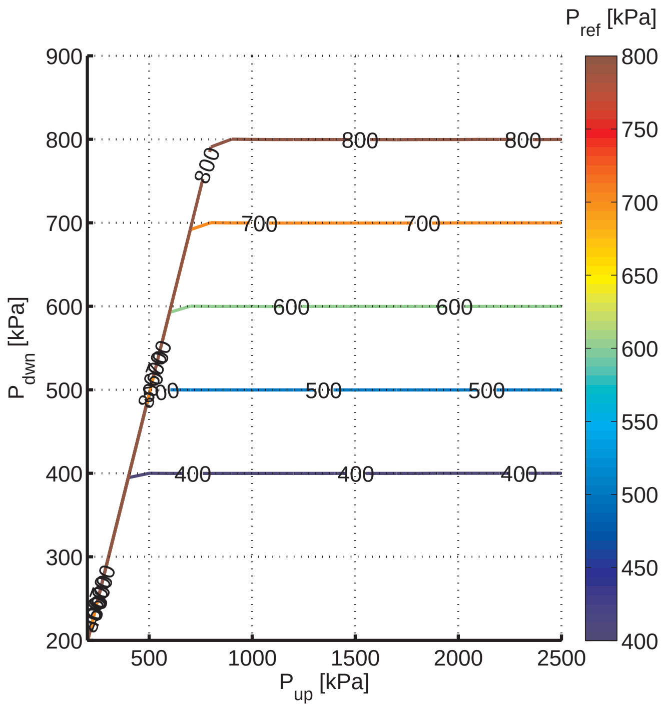

(a) Regulated pressure

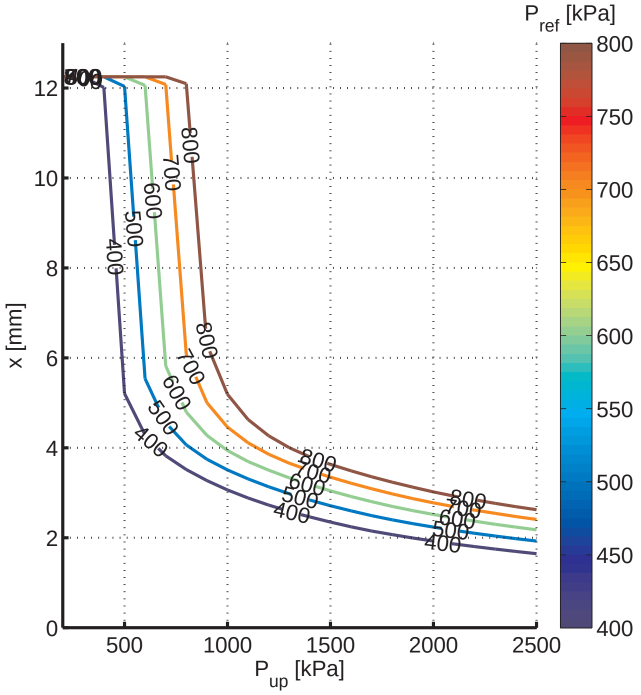

(b) piston position

Figure 1.13: In-line valve steady state simulation results

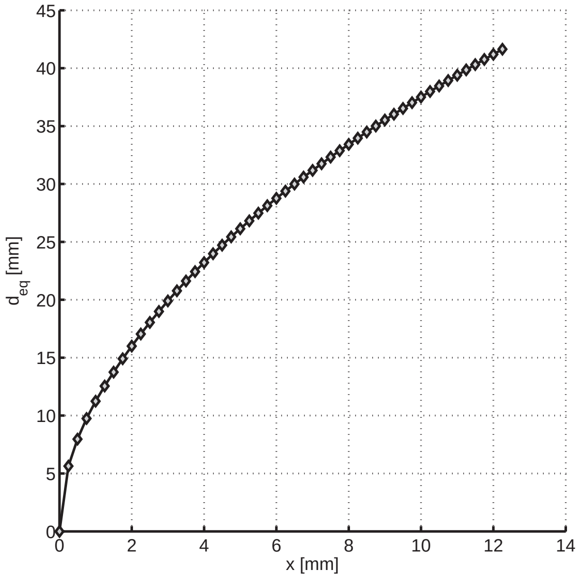

Figure 1.14: In-line valve d_{eq} at various piston stroke. The curve has been obtained combining equation (1.3.6) and (1.3.9)

operating conditions. The triangular openings have the advantage of create a more progressive area variation with the respect of the piston stroke. The solution to be adopted is a compromise between these two configuration; probably an elliptical shape is the best compromise, but it is difficult to be manufactured. The solution analyzed is based on trapezoidal openings having a bigger base of $r_{\mathrm{raz,maj}}$, and a minor base $r_{\mathrm{raz,min}}$.
The definition of Λ has to be revised in order to simulate the behavior of a valve equipped with trapezoidal openings (see equation (1.3.12)); equation (1.3.6) is still valid for a trapezoidal openings.

$$\Lambda = \pi - \frac{n_{\mathrm{raz}}}{d_{\mathrm{ext,pts}}} \left(r_{\mathrm{raz,maj}} - \frac{\left(r_{\mathrm{raz,maj}} - r_{\mathrm{raz,min}}\right) x}{2 x_{\mathrm{max}}} \right) \tag{1.3.12}$$

The advantages and drawbacks of the use of a trapezoidal openings are clearly shown in figure 1.15. The trapezoidal opening have a smoother area change with the respect of the piston stroke than the rectangular openings; on other hands the rectangular openings develop a larger equivalent diameter when the piston moves to fully open position. The simulations, performed at various inlet pressures, show the above effect in terms of pressures. The valve equipped with trapezoidal openings increase the piston stroke more progressively than the valve equipped with rectangular openings (figure 1.16(b)), but the drawback is an higher pressure drop when the valve is fully open (figure 1.16(a)).
A valve equipped with trapezoidal openings (or exotic shape openings) can be used on system where the pressure drops of the valve in fully open position

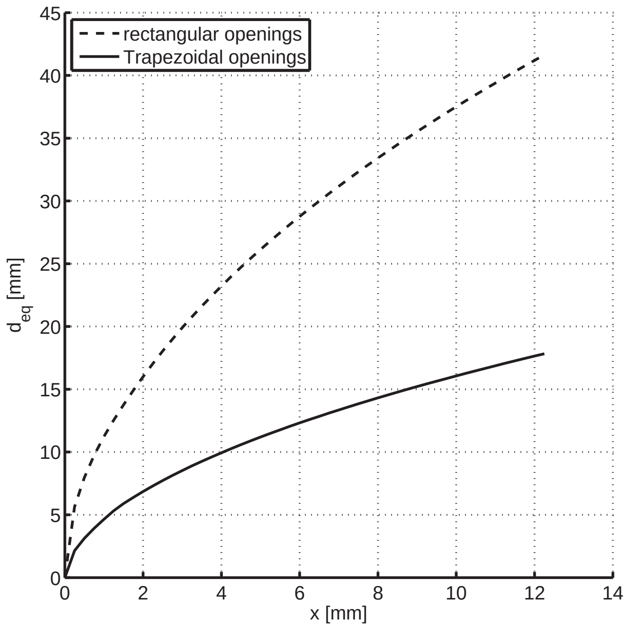

Figure 1.15: In-line valve d_{eq} for rectangular and trapezoidal opening

(and so when the inlet pressure is already low) are not vital and where a more accurate and stable control is needed; for all the applications where the pressure drops are the Achilles' heel of the system the valves with rectangular openings is still the best solution.

Time dependent simulations

Figures 1.17(a) and 1.17(b) reports the results of the unsteady state simulations. The simulations have been performed commanding the valve into closed position (by forcing $P_{\text{ref}} = 101.3\,\text{kPa}$) for the first 2 s, and then the commanding the valve open (by forcing $P_{\text{ref}} = 500\,\text{kPa}$).

At low pressure ($P_{\text{up}} \leq P_{\text{ref}}$) the piston is pushed to full open position in less than 0.2 s.

With higher inlet pressure ($P_{\text{up}} > P_{\text{ref}}$) the valve starts to limit the downstream pressure, so the piston does not reach the full open position. The pressure downstream the valve shows a spike after the valve opening; this spike increases with respect to the P_{up} and it is due to the abrupt change of regulation area: the equivalent diameter changes dramatically in a short band of piston stroke, the piston overpass the equilibrium point creating an equivalent diameter bigger than the needed and so the pressure spike. The valve recovers the control of the pressure after the passage through the critical area.

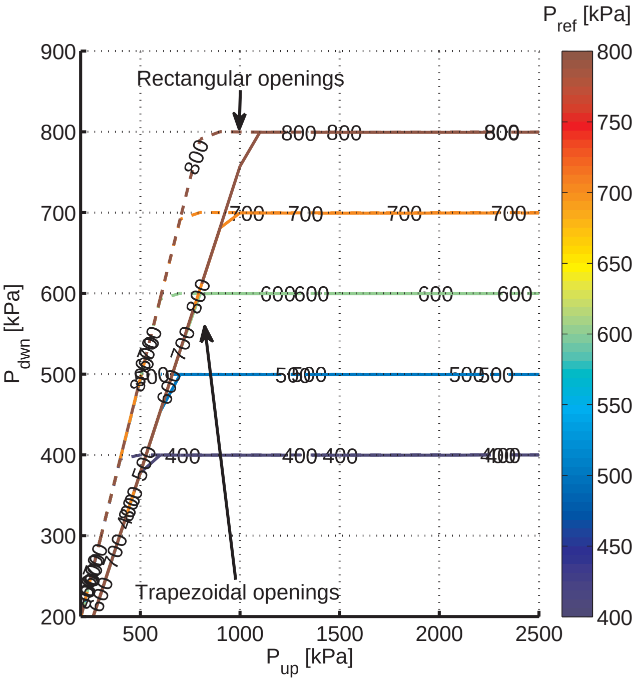

(a) Regulated pressure

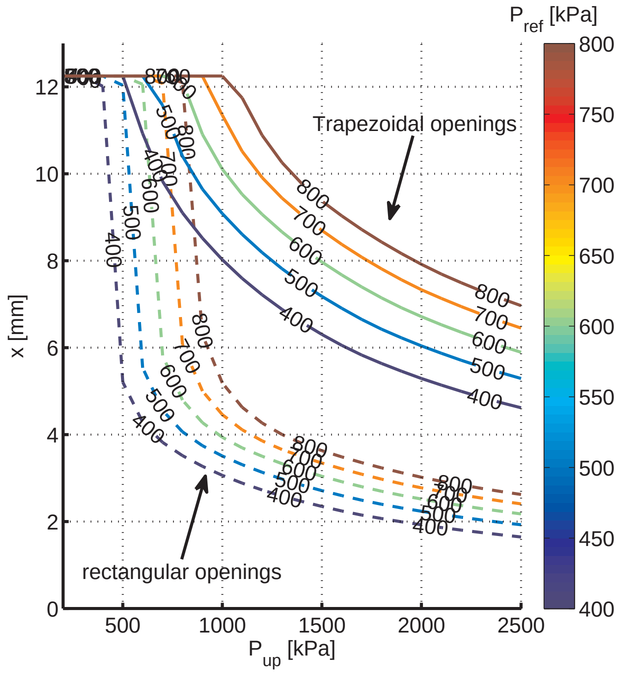

(b) piston position

Figure 1.16: Trapezoidal openings in-line valve steady state simulation results

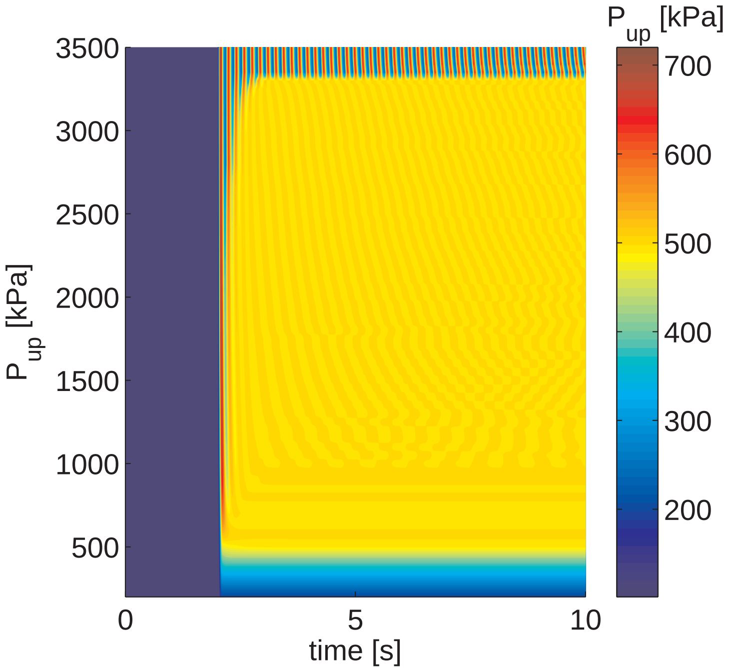

(a) Regulated pressure

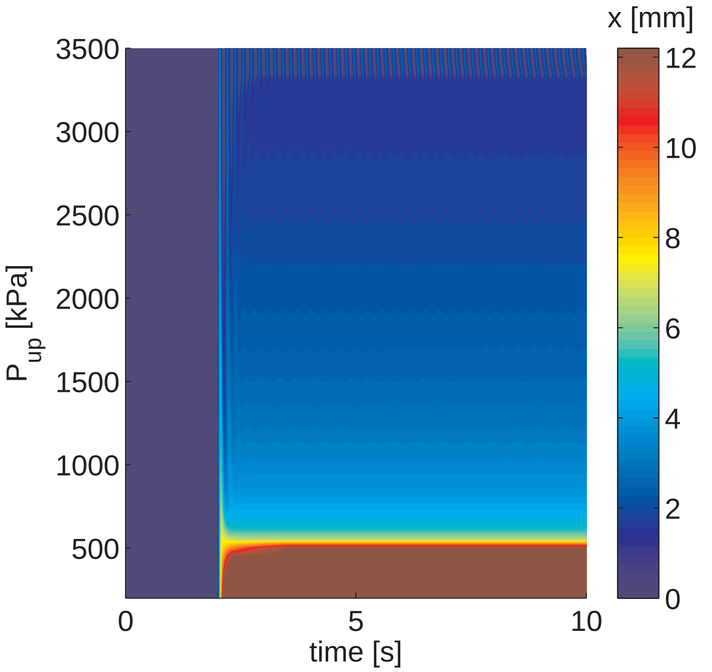

(b) Piston position

Figure 1.17: In-line valve unsteady state simulation results

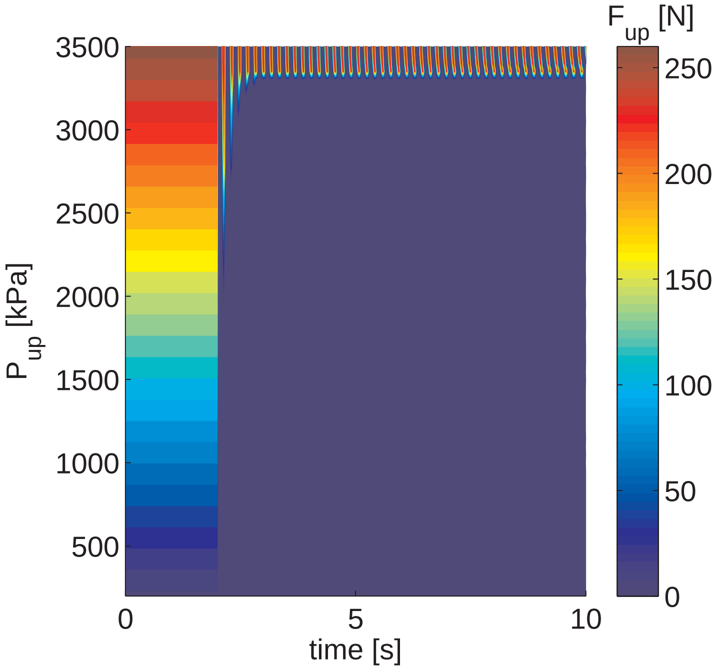

Figure 1.18: F_up trend at various valve inlet pressures

At very high pressure the valve becomes instable[7]. This instability phenomena is coupled with F_{up}.

F_{up} is the force generated by a small step on the piston and its own primary scope is to generate a force that keeps the piston in full closed position when the reference chamber is depressurized[8]. F_{up} is generated only when the piston is very near to the fully closed position. When the piston stroke is sufficient small, F_{up} becomes higher than 0 and push the piston to full closed position; the pressure downstream the valve falls down, since there is no more inlet flow into the downstream volume, and the piston moves to open, but it closes as soon as the downstream pressure rises (see figure 1.18). This hammering of the piston against the end stops easily bring the piston to breakage.

The instability cannot be avoided (since F_{up} is fundamental to keep the valve in fully closed position), but the P_{up} at which the phenomena starts can be increased, or increasing the size of the downstream orifice, or increasing the regulating pressure level, or adopting a piston with trapezoidal openings[9].

---

[7] the small fluctuation at intermediate pressure are due to the pneumatic coupling of the orifice-volume-orifice, and are not imputable to the valve; this is also confirm since the piston stroke does not change in these conditions.

[8] to avoid that external acceleration force the piston to move

[9] all these tricks bring the piston to operate farer from the full closed position

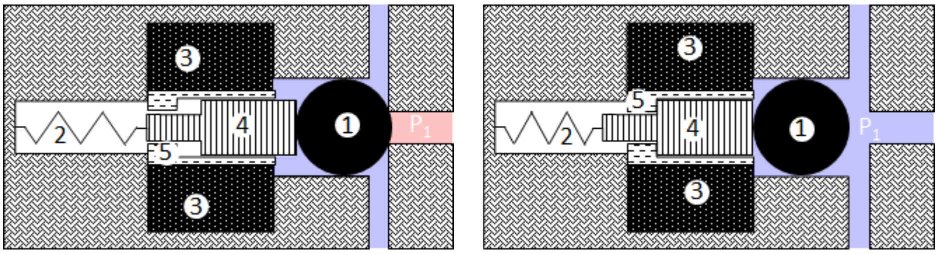

(a) direct acting solenoid valve - closed position

(b) direct acting solenoid valve - open position

Figure 1.19: Direct acting solenoid valve schematic. (1) sphere, (2) spring, (3) coil, (4) plunger
, (5) core

1.4 Direct acting solenoid valves

Figure 1.19 shows a sketch of a direct acting solenoid valve. The sphere (1) is forced into closed position by the spring (2) when the coil is de-energized; so the valves is equivalent to a normal relief valve. When the coil (3) is energized, the magnetic force generated by the coil forces the plunger (4) to compress the spring countering the force which keeps closed the sphere. The pressure on valve inlet (P_1) opens the valve.

In shut-off solenoids, the force of attraction increases with decreasing of the air gap between the plunger and the coil. The plunger and the coil can be shaped such that the force of attraction is relatively constant over the stroke. The constant force plus the spring creates a *proportional solenoid*, a solenoid generating a force on the sphere proportional to the electrical current applied.

A valve equipped with a proportional solenoid is equivalent to a relief valve with variable cracking point.

The proportional solenoids are affected by hysteresis issues. The hysteresis is generated by the combination of the magnetic hysteresis and the mechanical hysteresis. The magnetic hysteresis is due to the plunger residual magnetization. In fact a ferromagnetic material which has been magnetized introducing it into a electrical field, gradually decreases its magnetization over the time when the external field is removed. On the solenoid this phenomena does not allows to associate unambiguously the electrical current supplied to the force generated by the solenoid (and so to the controlled pressure). The mechanical hysteresis is due to the friction phenomena.

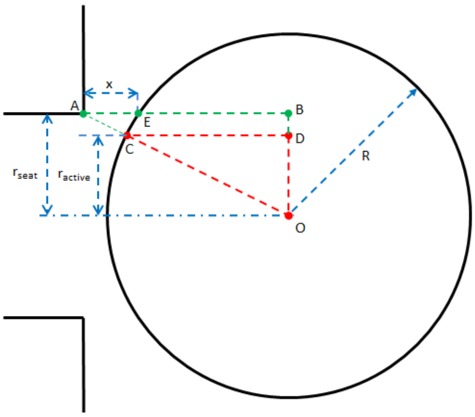

Figure 1.20: Spherical poppet configuration

1.4.1 Mathematical model

Flowing area

The solenoid valve under analysis uses a spherical poppet, figure 1.20 is the sketch of the configuration under analysis. Equations (1.4.1) are derived from simple geometrical considerations (see Andersen [2001]).

$$\overline{AB} = x + \sqrt{R^2 - r_{\text{seat}}^2} \tag{1.4.1a}$$

$$\overline{AO} = \sqrt{\overline{AB}^2 + r_{\text{seat}}^2} \tag{1.4.1b}$$

$$d_{\text{active}} = 2r_{\text{active}} = 2(Rr_{\text{seat}}\overline{AO}^{-1}) \tag{1.4.1c}$$

Equation (1.4.2) is the formula to calculate the flowing area for a spherical poppet; this formula has been obtained introducing into equation (1.2.1c) the equations (1.4.1) and writing the resulting equation in terms of diameters.

$$A = \frac{\pi d_{\text{seat}}^2}{4} \frac{\left(2xd_{\text{seat}}^{-2} + \sqrt{D^2 d_{\text{seat}}^{-2} - 1}\right)^2 + 1 - D^2 d_{\text{seat}}^{-2}}{\sqrt{\left(2xd_{\text{seat}}^{-2} + \sqrt{D^2 d_{\text{seat}}^{-2} - 1}\right)^2 + 1}} \tag{1.4.2}$$

Equation (1.4.2) is valid if the calculated area is smaller than the area of the seat; in the opposite case, the throat area is the seat area.

Equation (1.2.3) is used to calculate the flow rate through the solenoid. In this case the area is calculated using equation (1.4.2), the c_q according to Andersen [2001] is between 0.75 and 0.88.

Magnetic force

The magnetic force (F_{magnetic}) is calculated using equation (1.4.3).

$$\iota_1 = \frac{\mu_0 A_{\text{gap}}}{2 f_{\text{flux}}} n^2 \tag{1.4.3a}$$

$$F_{\text{magnetic}} = \iota_1 \left(\frac{I_{\text{eff}}}{x_{\text{gap}} + l_e} \right)^2 \tag{1.4.3b}$$

Where:

- μ_0 is the permeability of free-space [$\mathrm{W\,A^{-1}\,m}$]
- A_{gap} is the cross sectional area of the gap [$\mathrm{m^2}$]
- f_{flux} is the factor for flux leakage and area replacement
- I_{eff} is the effective electrical current [A]
- x_{gap} is the linear gap between the armature and the core [m]
- l_e is the equivalent reluctance length [m]
- n_{coil} is the number of coil turns

The x_{gap} is directly proportional to the plunger movement, in an on/off solenoid, it is constant for a proportional solenoid.

I_{eff} is the parameter which takes into account the hysteresis and non-linearity phenomena. The effectiveness electrical current acts on the solenoid is limited using a hyperbolic tangent function (see equation (1.4.4)), and if the derivative of the input current with respect to the time change sign, I_{eff} will be constant until the value calculated using equation (1.4.4) is not equal to the last I_{eff} value before the change of sign (see Simulink® model in figure 1.21(a) and the result trend in Figure 1.21(b)).

$$I_{\text{eff}} = \begin{cases} \tanh \frac{I-b_1}{b_2} & \text{if } \frac{\partial I}{\partial t} \geq 0 \\ \tanh \frac{I+b_1}{b_2} & \text{if } \frac{\partial I}{\partial t} < 0 \end{cases} \tag{1.4.4}$$

The coefficient b_1 and b_2 are derived from experimental tests.

Generally the hysteresis model is based on the Jiles-Atherton model. It is a model for ferromagnetic hysteresis, based upon a theory of reversible and irreversible motion of domain walls in the material. This model reproduces pretty well the phenomena, but it requires a not negligible computation effort. To reduce simulation time the simplified approach here above presented has been adopted[10].

---

[10] The hysteresis is not fundamental to develop the control rules since the control loops are generally closed on the regulated pressure or system performance and not on the solenoid plunger position

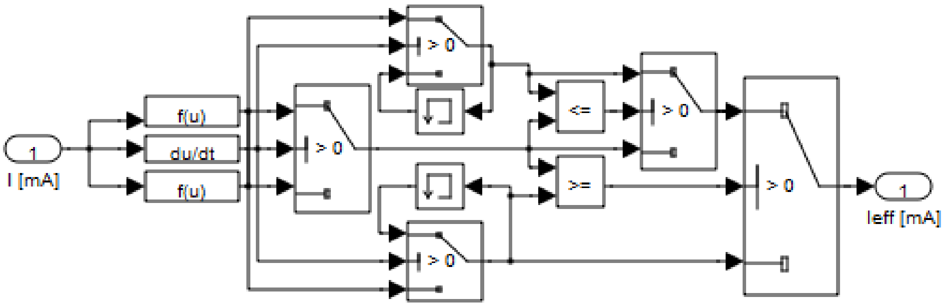

(a) Hysteresis Simulink® model

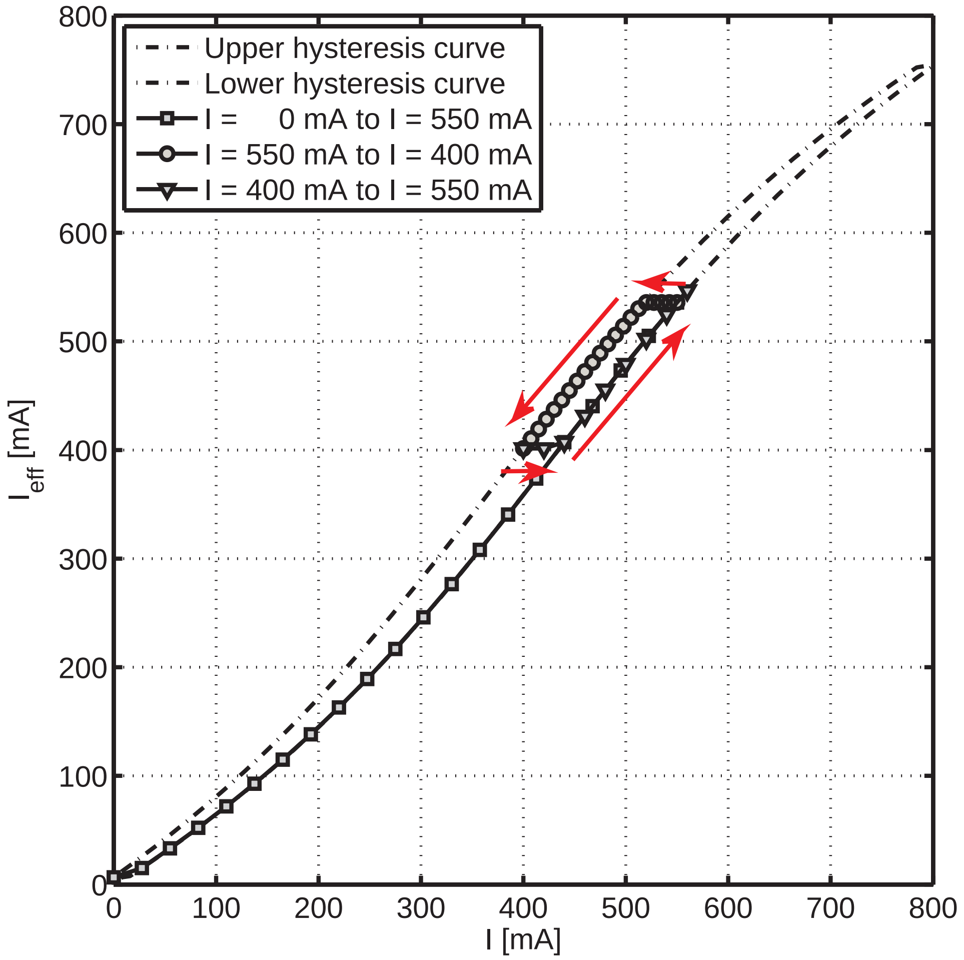

(b) Hysteresis Simulink® model results

Figure 1.21: Magnetic hysteresis model

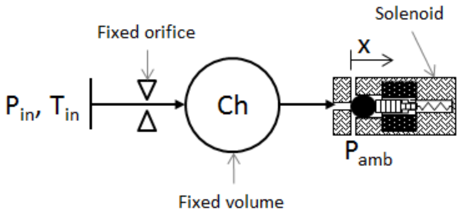

Figure 1.22: Solenoid valve mathematical model and test rig schematic

Sphere movement equation

The solenoid sphere moves following the equation of the motion (1.2.5); the plunger and the sphere are considered as a single body (rigidly connected) and the mass M is the sum of the two masses. The F acts on the plunger is divided into:

- spring force (F_{spring}, see equation (1.2.6))
- pressure forces ($F_{\text{pressures}}$, see equation (1.2.7))[11]
- external forces ($F_{\text{external}} = 0$)[12]
- magnetic forces (F_{magnetic})

So the force acting on the solenoid plunger is:

$$F(t) = \underbrace{k(x - x_0)}_{F_{\text{spring}}} + \underbrace{\frac{\pi d^2_{\text{active}}}{4}\left(P_{\text{ch}} - OAP\right)}_{F_{\text{pressures}}} - \underbrace{\iota_1 \left(\frac{I_{\text{eff}}}{x_{\text{gap}} + l_e}\right)^2}_{F_{\text{magnetic}}} \tag{1.4.5}$$

0d model

The equations here above detailed have been used to create a 0d model of a solenoid valve. Figure 1.22 shows the sketch of the model created. It simulates an ideal air pressure and temperature source which flows the gas through an calibrated orifice into a fixed volume (see paragraph 1.1.1 and equation (1.2.3)). The pressure inside the volume is controlled by a solenoid valve. Table 1.5 summarizes the main parameters, and table 1.6 reports the initial conditions of the simulations. The simulations have been performed:

- at fixed electrical command to the solenoid changing the Pin
- at fixed P_{in} changing the electrical command to the solenoid

---

[11] d_{active} for a spherical poppet is calculated using equation (1.4.1c)

[12] neglecting all the forces due to external accelerations (i.e gravitational force, airplane vibrations, airplane manoeuvres, etc.)

Parameter	Unit	Value
Plunger M	g	5.0
V	dm^3	0.1
k at 20 °C	$\mathrm{N\,m^{-1}}$	7650.0
Fixed orifice d	mm	0.8
d_{seat}	mm	5.0
R	mm	3.25
x_0	mm	2.18
T_{air}	K	298.15
$c_{\mathrm{q,fix}}$		0.8
ι_1	$\mathrm{W\,A^{-1}\,m}$	582e−6
l_e	mm	1

Table 1.5: Solenoid valve model main parameter

Parameter	Unit	Value
P_{ch}	kPa	101.3
T_{ch}	K	298.15
v_{plunger}	$\mathrm{m\,s^{-1}}$	0.0
x_{plunger}	mm	0.0

Table 1.6: Solenoid valve model, initial simulation conditions

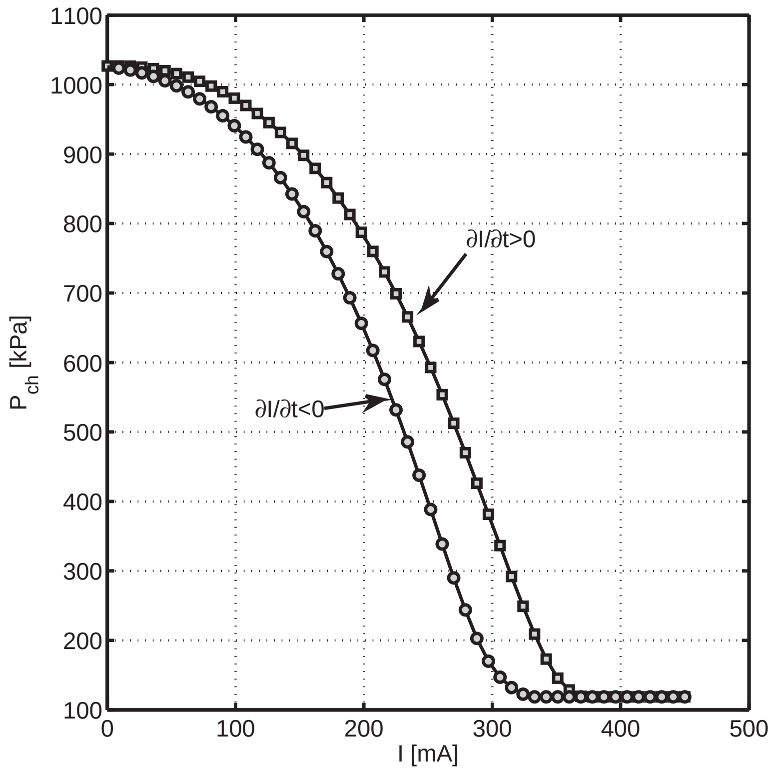

Figure 1.23: Solenoid valve regulated pressure to a variable input command ($P_{\text{in}} = 2100\,\text{kPa}$)

1.4.2 Mathematical model results

The first simulation has been performed keeping P_{in} constant at 2100 kPa, and modulating the electrical current (I) from 0 mA to 450 mA and then back to 0 mA. Figure 1.23 shows the trend of the P_{ch} with the respect of I.

With no input current the solenoid does not generate any force and the valve setting point is set only by the spring pre-load. Increasing the input current the force generated by the solenoid adds to the pressure force, acting on the sphere, and the regulated P_{ch} decreases. At high input current ($I \geq 350\,\text{mA}$) the force generated by the solenoid is higher than the force the spring can generated and the sphere is pushed into full open position; the pressure inside the chamber drop to ambient level, since the equivalent orifice generated by the sphere is one order of magnitude higher than the fixed orifice.
When the current increases the force generated by the solenoid is lower than when the current decreases (see hysteresis model in figure 1.21(b)) and so the regulated pressure is higher; viceversa when the input current decreases. Figure 1.24 shows the trend of the P_{ch} at various P_{in} at various I. The trend of P_{ch} reflects the results of figure 1.23, and the trend of P_{ch} with respect

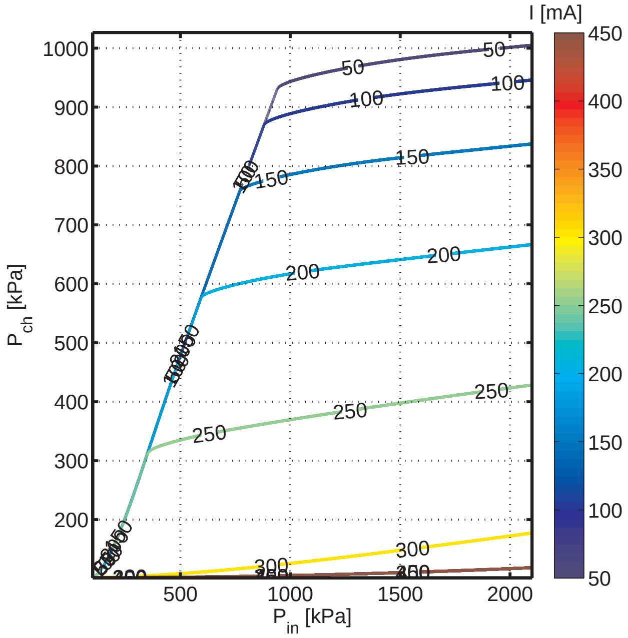

Figure 1.24: Solenoid valve regulated pressure at various I and P_{in}

to P_{in} is identical to a relief valve behavior (see figure 1.6(b)): in fact the solenoid valve is a relief valve with a variable cracking pressure (adjustable modulating I). All the explanations and the remarks done on the relief valves are applicable also to the solenoid valves (refer to paragraph 1.2.2 and paragraph 1.2.3).

One of the critical point of the relief valves is the the influence of the temperature. The use of a solenoid can solve, or at least mitigate, the issue controlling actively the P_{ch}.

A simple PID controlled has been created to modulate the solenoid input current using as control variable the pressure inside the reference chamber. Table 1.7 summarizes the main parameters of the controller.

Figure 1.25 shows the comparison between the active controlled system and a system with no active control. The use of the solenoid valve with a simple control loop allows a perfect control of the pressure inside the chamber; the control modulates the solenoid force compensating the effect of the temperature on the spring and the effect of the inlet pressure. Since the control loop is closed on P_{ch} the hysteresis does not influence the achievement of the target.[13]

---

[13] a control loop based on the plunger position could be influenced by hysteresis

Parameter	Unit	Value
Anti-windup method	-	clamping
Proportional gain	-	2.1
Integrative gain	-	10.0
Derivative gain	-	0.115
Minimum permitted value	mA	0
Maximum permitted value	mA	450
Input signal	kPa	P_{ch}
Output signal	mA	I
Target	kPa	600

Table 1.7: Solenoid valve model, PID parameters

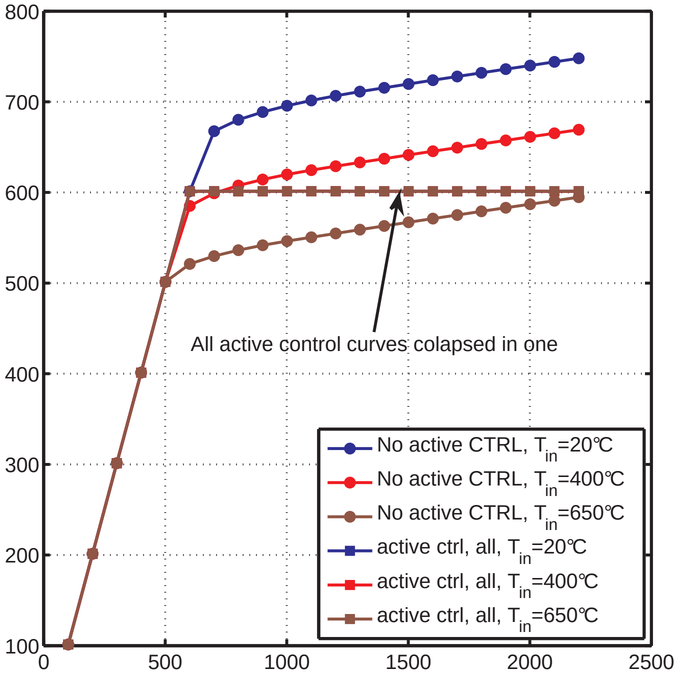

Figure 1.25: Active controlled solenoid simulation results

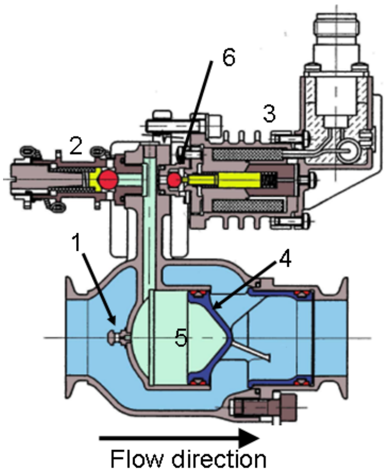

Figure 1.26: Valve cut off view.(1) control orifice, (2) relief valve, (3) ON/OFF solenoid, (4) main piston), (5) reference chamber, (6) solenoid venting hole

1.5 Mathematical model validation

To validate the mathematical models here above described a commercial in-line PRSOV has been tested. The valve under analysis is equipped with a relief valve to limit the downstream pressure and with a ON/OFF solenoid to allow a remote control of the valve (a simple ON/OFF control). Figure 1.26 shows the cut off view of the valve under analysis.

1.5.1 Experimental data

Figure 1.27(a) shows the experimental setup for the test. The setup simulates a cluster of 2 PRSOV installed in series. The first valve is called Upstream Anti-Ice Valve (UAIV) and the second valve is called DAIV (DAIV). The fixed orifice installed downstream the cluster simulates a piccolo tube. The valves are connect to a 2500 kPa air pressured line. The pressure at valve inlet is set thanks to a valve controlled by the operator. The test rig has the following characteristics:

- V1 = 0.155 l
- V2 = 1.560 l
- Fixed Orifice diameter = 18 mm

The parameters listed in table 1.8 are recorded at 1 kHz.
The dynamic response of the pressure sensors used, has been verified with a piezoelectric pressure transducer on a separate test rig. The sensors demonstrate the capability to detect pressure oscillation over 1 kHz.

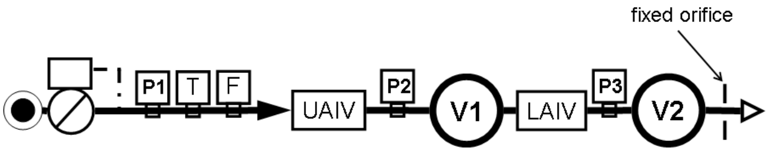

(a) Test rig schematic

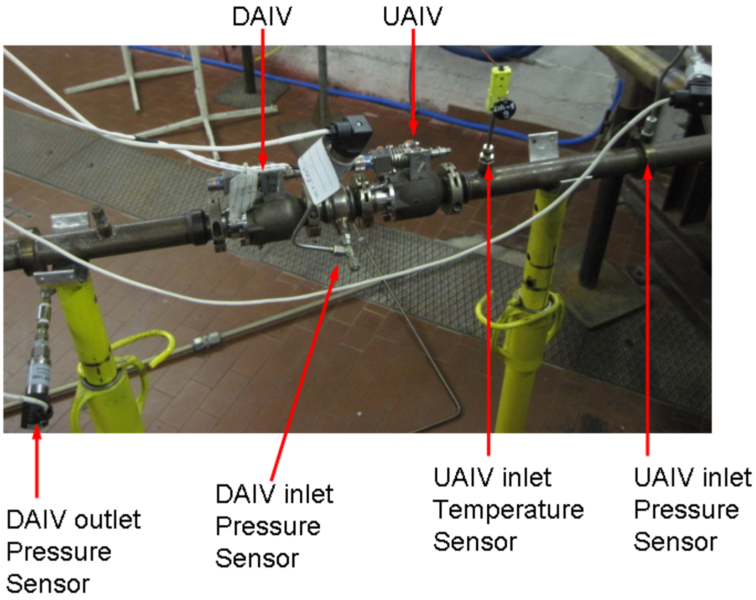

(b) Valves test rig picture

Figure 1.27: Valves test rig

Parameter	Sensor Type	Unit	Sensor Range	Accuracy
P1	Druck PMP 1400	kPa	0 to 2500	3.75
P2	Druck PMP 1400	kPa	0 to 1000	1.5
P3	Druck PMP 1400	kPa	0 to 1000	1.5
T1	Thermocouple type K	K	273.15 to 773	0.5

Table 1.8: Valve test rig sensors

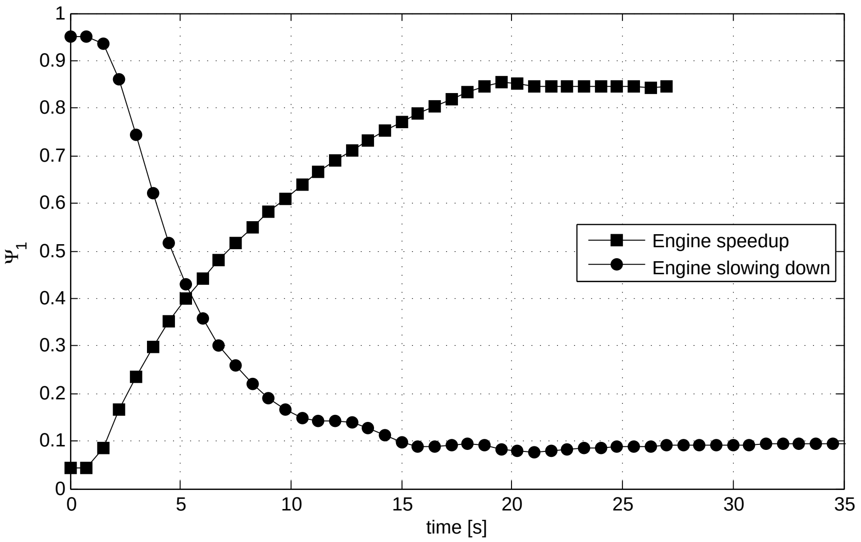

Figure 1.28: Transient cases under analysis

The accuracy reported in table 1.8 includes the combined non-linearity, hysteresis and repeatability. The accuracy reported for the thermocouple includes also the uncertainty due to the electronic ice point.

Pressure sensors are affected also by error due to temperature. This is the major component of a pressure measurement uncertainty; adding this error to the accuracy of the sensor, the total error band on the measured pressure is ±1.5%.

Four cases has been taken into consideration for model validation; two cases wants to simulate the behavior of the bleed pressure during engine speedup at take off and during engine slowing down after the landing (see figure 1.28). Two cases analysis the behavior of the valves when commanded closed and open (one at high pressure and one at medium pressure).

1.5.2 Computer model

A 0-d model uses the equations here above detailed has been created using *AMEsim*®. The model reproduces the test setup described in figure 1.27(a).

1.5.3 Mathematical model and test results comparison

The results of the mathematical model are presented using two dimensionless coefficients:

$$\zeta = \frac{x}{x_{\max}} \tag{1.5.1a}$$

$$\Psi = \frac{P_1}{P_{1,\max}} \tag{1.5.1b}$$

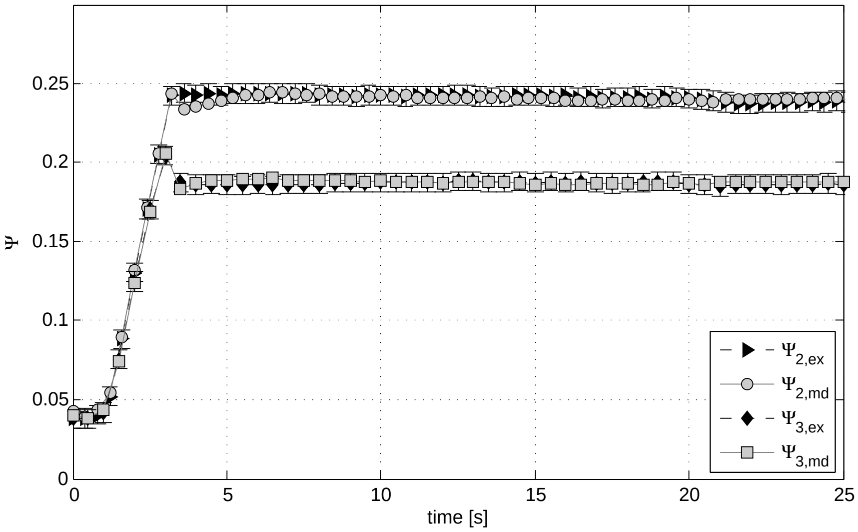

(a) Engine speedup

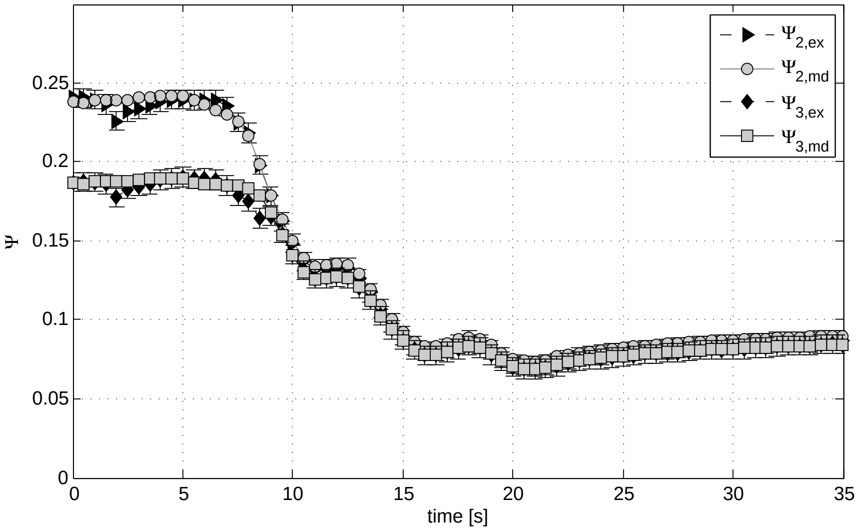

(b) Engine slowing down

Figure 1.29: Valve transient cases - pressure trends

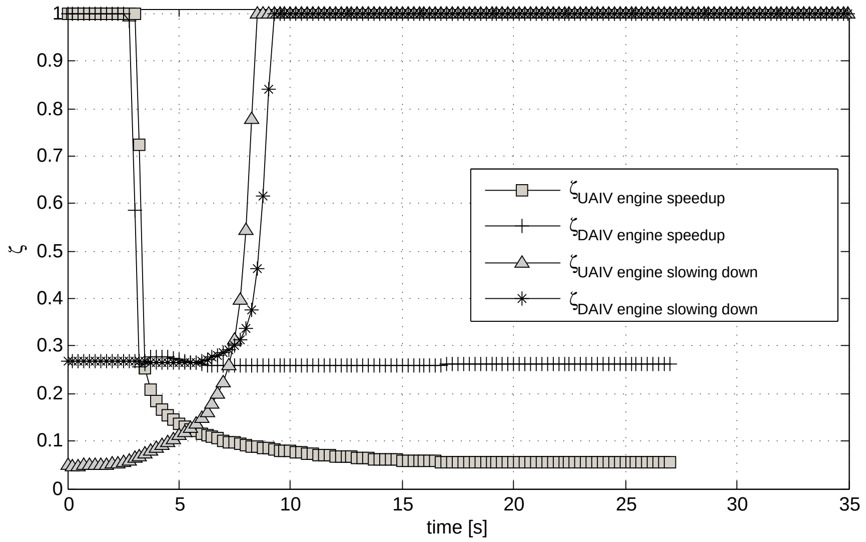

Figure 1.30: Valves transient cases - main piston stroke (model prediction)

In the engine speedup case (see figure 1.29(a)) the pressure downstream the two valves (P_2 and P_3) increases following P_1 until the cracking point of the DAIV relief valve is reached. At this point the pressure inside the reference chamber is kept constant by the opening of the relief valve; P_2 continuous to increase and the resulting force on the main piston (see equation 1.3.4) moves the piston to close. The flow area is reduced (see figure 1.30) and the pressure drop across the valve inncreases, thus the P_2 decreases.

The variation of the flow area of the DAIV implies that the air flows out from V_1 decreases, the inlet flow rate is not changing, therefore the pressure inside V_1 increases and that push the UAIV to close (UAIV behavior is similar to the DAIV behavior described here above). When the UAIV closes the air flowing into V_1 decreases and an equilibrium point between position of the pistons and system pressures is reached.

In the engine slowing down case (see figure 1.29(b)), the pressure downstream the two valves remains constant and than when P_1 goes down the regulation point the pistons reach the full open position (see figure 1.30), P_2 and P_3 follow the behavior of P_1 (the difference between P_1 and the other pressure is due to the pressure drop of the valves).

In the open/close cases (refer to figures 1.31 and 1.32) the UAIV is commanded closed and then open. When the UAIV is commanded closed, the solenoid opens and the reference chamber is vented to ambient pressure. On the main piston acts only forces push the piston into close position (F_{up} and P_{dwn}), so the piston moves to full closed position. At this point P_2 falls down (since there is no inlet flow rate) and the DAIV flow rate, so the flow rate entering V_2, decreases (see equation 1.2.3); the V_2 outlet flow rate becomes

higher than the inlet flow rate and P_3 decreases. the pressure inside the reference chamber becomes higher than P_3 (the relief valve closes when the pressure inside the reference chamber goes under the cracking point) and the DAIV main piston moves to open position.
At the end the UAIV piston is in fully closed position (kept into closed position only by F_{up}), the DAIV piston is in fully open position (see figure 1.30)) and P_2 and P_3 are equal to ambient pressure.
When the UAIV is commanded open the solenoid closes, the reference chamber became pressurized and the UAIV piston opens. The air flows into V_1 and V_2 increasing rapidly the pressure in both the volumes (the inlet flow in the 2 volumes is higher than the outlet flow because of the pressure ratio along the system). When the pressures rise over the control pressure of the DAIV the phenomena is identical to the one described for engine speedup.
The model predictions match the experimental results. The shape of the response is well predicted as also the intensity of the overshoot. In the open/closing cases the model and experimental data are not completely inline, but considering the response time of the valve and the shape of the predicted response the model results are still good.

1.6 Valve behavior at different temperatures and pressures

The model has been used to predict the behavior of the valves at various inlet pressure (from $0.2P_{\text{max,engine}}$ to $P_{\text{max,engine}}$) and temperature (from 25 °C to 650 °C). Figure 1.33 shows the results of the analysis. There are some fluctuations on the regulated pressure, especially for the UAIV. These fluctuations are linked to the friction model used.
The use of a friction model which includes the stiction force allows to reproduce very well the behavior of the valve in transient conditions (see paragraph 1.5.3), but it introduces a dependency from the initial conditions and from the path (from a pure mathematical point of view the field is not conservative); this dependency is reflected in the results of figure 1.33. $F_{net,pts,UAIV}$ has to be equal to 0 in steady state conditions, but in the performed simulations the value is always less than 4 N (see figure 1.34) which is the value of stiction force (c_3). The fluctuations are explained analyzing the dynamic behavior of the valve. At time $t = 0$, both the pistons are set in full open position (initial conditions); as soon as the simulation starts, the pistons close to increase the pressure drop across the valves (since P_1 is higher than the valve regulated pressures). If the piston moves faster than the pressure increase in the volume downstream the valve (on other words $\frac{dx}{dt} \geq \frac{dP_2}{dt}$), the piston pass over the equilibrium point and a force that call back the piston to the equilibrium point is generated ($F_{net,pts}$ changes sign). This force first stops the piston and than, if $F_{net,pts} \geq c_3$, it pushes back the

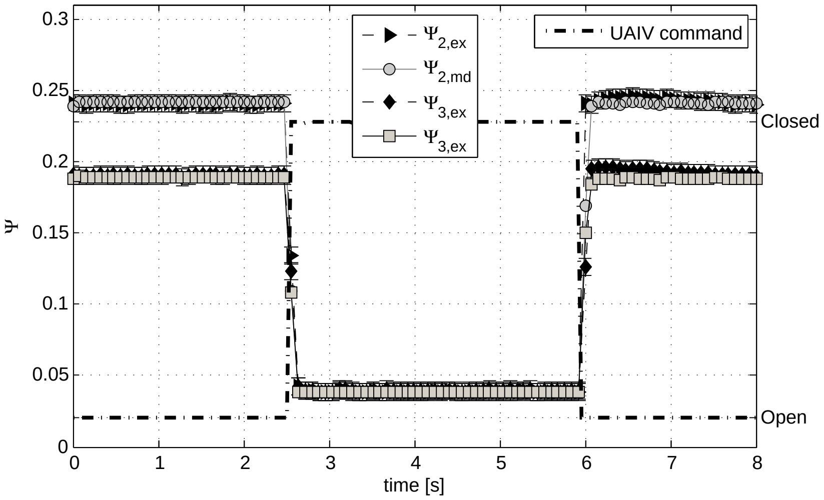

(a) $P_{bleedin} = 0.6P_{bleed_max}$

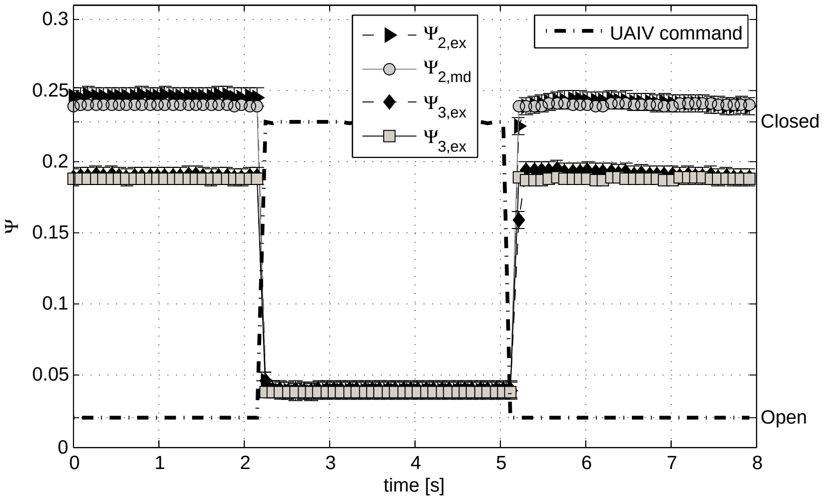

(b) $P_{bleedin} = 0.8P_{bleed_max}$

Figure 1.31: Open/closed cases - pressure trends

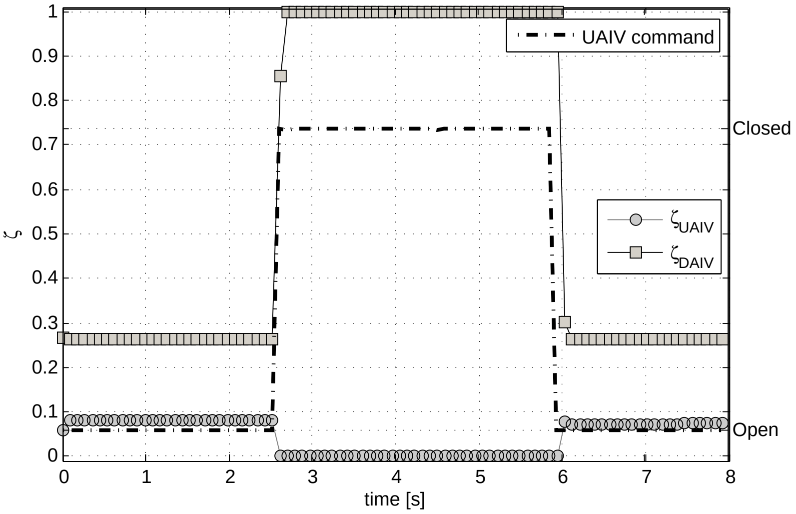

(a) $P_{bleedin} = 0.6P_{bleed_max}$

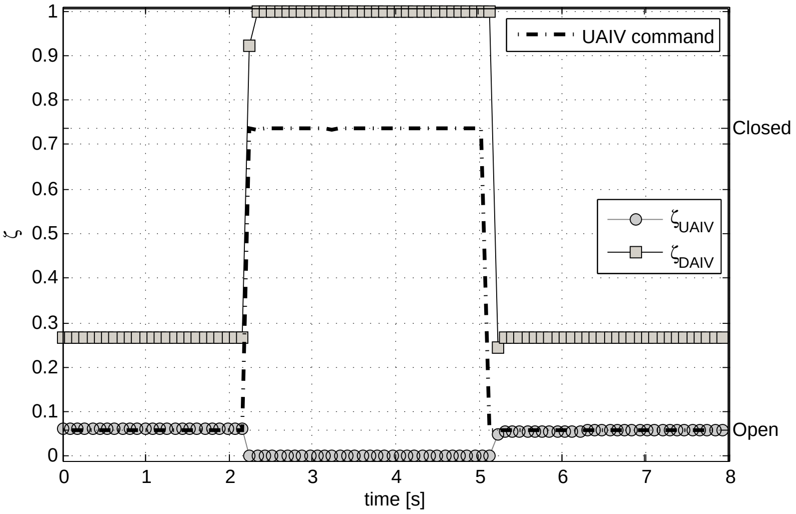

(b) $P_{bleedin} = 0.8P_{bleed_max}$

Figure 1.32: Open/closed cases - main piston stroke (model prediction)

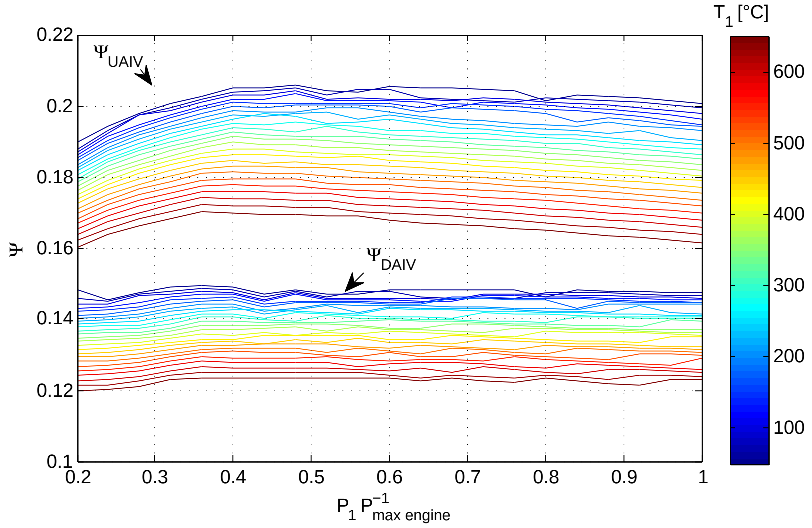

Figure 1.33: Valve behavior at different bleed pressure and temperature

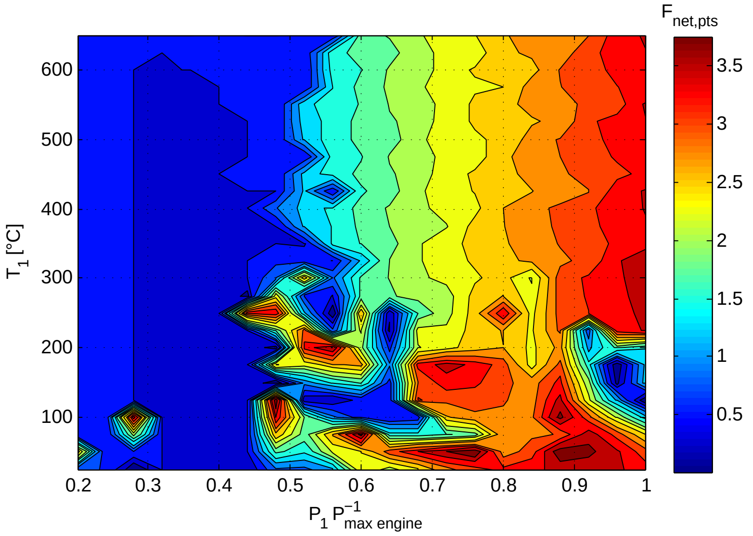

Figure 1.34: $F_{net,pts,UAIV}$ trend

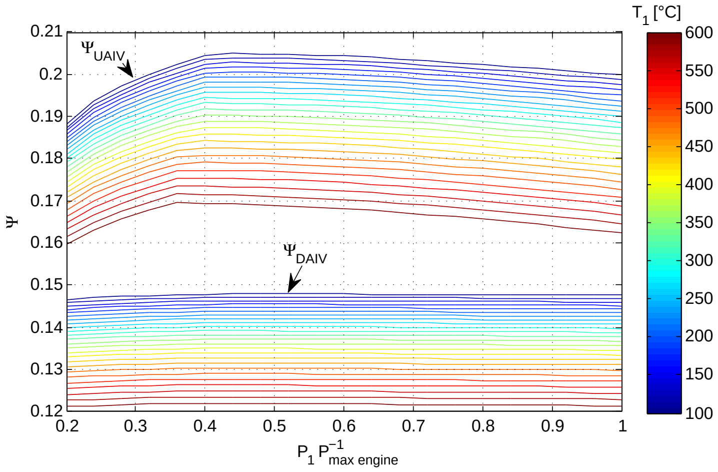

Figure 1.35: $F_{net,pts,UAIV}$ trend

piston to the equilibrium position; but, if $F_{net,pts} < c_3$, the piston remains in the closer position and the pressure drop of the valve remains higher than the expected so the regulated pressure stabilizes on a lower value. That explains the fluctuations on the regulated pressure see in figure 1.34.

This scenario is also confirmed by simulations performed with no friction (see figure 1.35). In these simulations the fluctuations disappear and only the influence of P_1 and T_1 are still present. Removed the unexpected fluctuations due to the friction model, the behavior of the system at various T_1 is analyzable.

At low Ψ_1 the P_2 increases follow P_1, then for $\Psi > 0.4$ (note that this knee depends on the T_1) P_2 has a negative slope. This is due to Upstream pressure closure force (F_{up}): at low Ψ_1 F_{up} is zero because the piston is still too far from the closed position (see figure 1.37 and equation 1.3.2), the valve follows the behavior of the relief valve (which increases its regulation point with the increase of the inlet pressure); at higher Ψ the piston is near to the full closed position, F_{up} became not negligible (see figure 1.36) and the valve change its trend.

The P_3 is more constant because the UAIV filters the P_1 variation keeping the pressure at DAIV inlet constant thus the DAIV is able to keep a very accurate control of the downstream pressure.

Both valves suffer of great influence of the temperature. The change in the regulated pressure is due to the spring rate decrease (see paragraph 1.2) and thus of the relief valve cracking point. Since the relief controls the pressure inside the reference chamber, the change of the cracking point modifies the equilibrium point of the piston (see equation 1.3.1) and so the values of P_2 and P_3.

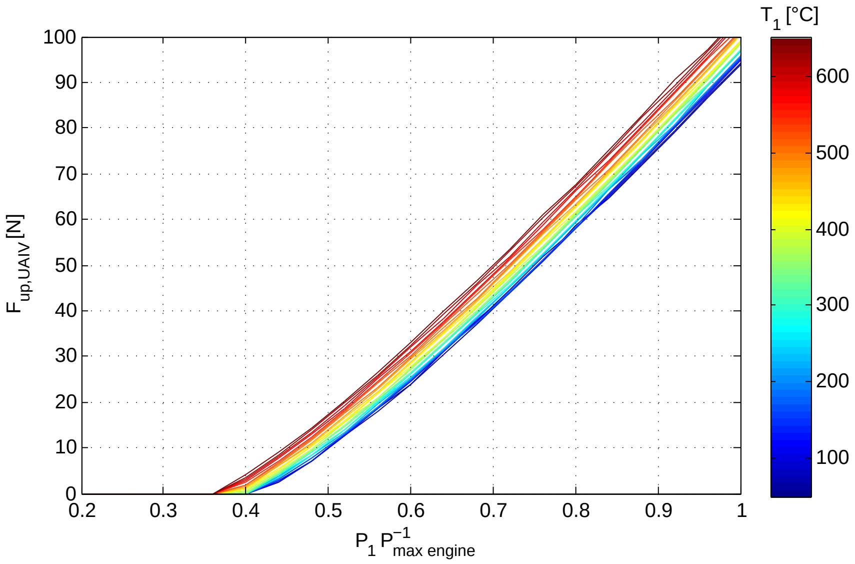

Figure 1.36: $F_{net,pts,UAIV}$ trend

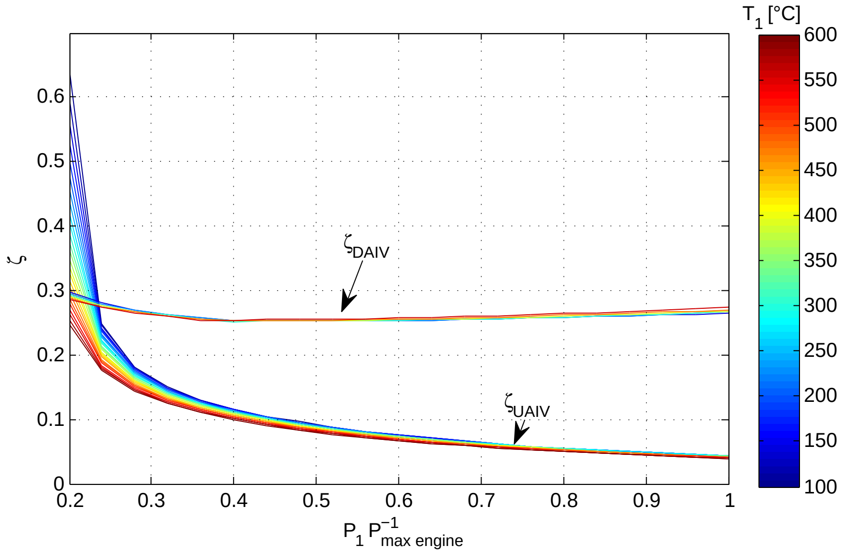

Figure 1.37: $F_{net,pts,UAIV}$ trend

Parameter	Unit	Value
$P_{t=0}$	kPa	101.325
$T_{t=0}$	°C	15
x	mm	0
$x_{solenoid,t=0}$	mm	$x = x_{\max}$
$\vec{v}_{t=0}$	$\mathrm{m\,s^{-1}}$	0
$P_{\mathrm{1,t=0}}$	kPa	200
$T_{\mathrm{1,t=0}}$	°C	15
$V_{\mathrm{1,t=0}}$	$\mathrm{m^3}$	0.001 55
$V_{\mathrm{ref,ch}}$	$\mathrm{m^3}$	0.000 02

Table 1.9: Valve stability simulation initial conditions. If not otherwise stated the initial values apply to all the relevant sub-component (i.e. x is applicable either for the relief piston and for the main piston)

1.7 Valve instability

The mathematical model has been used to predict the operating range of the valve and to investigate if there are conditions such that the valve shows instability. Figure 1.38 shows the simulated system and table 1.9 reports the initial conditions of the simulation.

The study has been performed simulating a valve opening at 2 s at various inlet pressure; figure 1.39 shows the results of the simulation.

At low inlet pressure ($P_1 < 400\,\mathrm{kPa}$) the valve is not regulating: the piston moves to opening position, and $P_2 \approxeq P_1$. Around $P_1 < 500\,\mathrm{kPa}$ the valve starts to regulate and the piston stroke reaches 4 mm. Continuing increasing P_1, the valve starts to have a small overshoot at the opening: the intensity of the overshoot and the time to reaches stabilization increase with the respect to P_1. Over 2400 kPa the valve does not reach a stability position and the piston continue to oscillate trying to control the downstream pressure. Over 2700 kPa the piston starts to hammer against the end-stop ($x = 0\,\mathrm{mm}$) creating an high risk working condition for the valve (continuous hammering dramatically reduces the life of the valve).

The instability in this case is due to the small piston stroke. In this operating condition a small change of the piston stroke means a great change of the forces acting on the piston (in particular F_{up}), thus the acceleration of the piston is huge and the piston continues to overpass the equilibrium position. This kind of instability cannot be avoided, but the pressure at which the instability occurs can be modified changing the pressure drop of the piston (by example adopting trapezoidal windows instead rectangular windows). Figure 1.40 shows the effect of piston shape change.

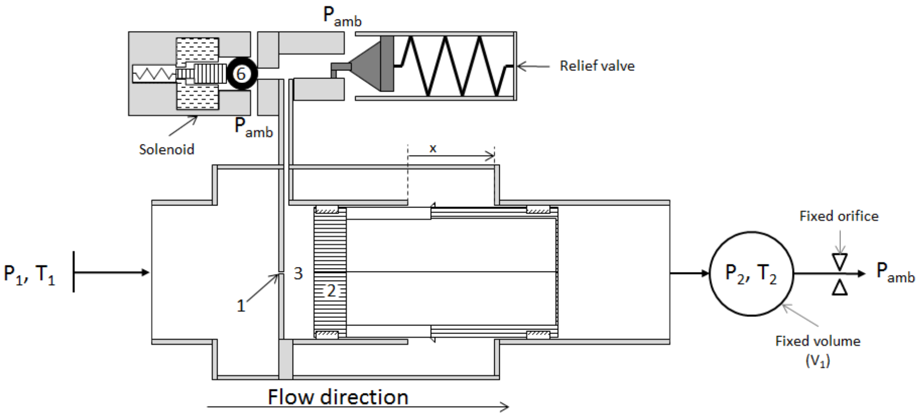

Figure 1.38: Valve instability model sketch. (1) is the fixed orifice which limits the flow rate to the reference chamber (3).

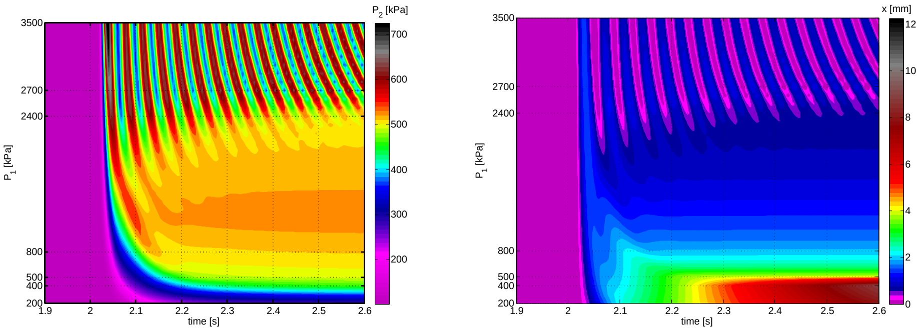

(a) Valve downstream pressure

(b) Valve piston stroke

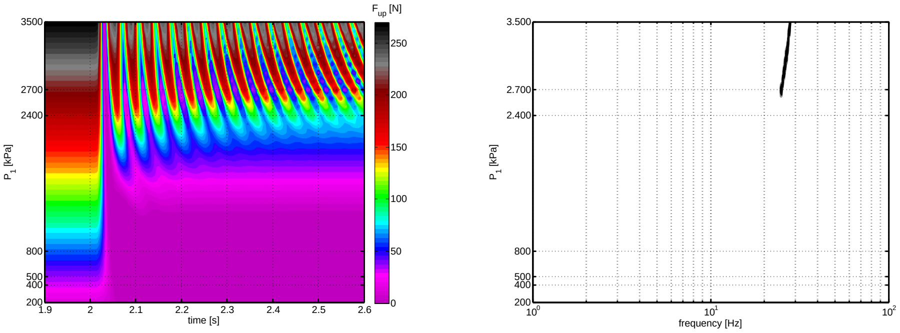

(c) F_{up}

(d) spectral map

Figure 1.39: Valve instability at high P_1. Valve command open at t=2 s, valve inlet pressure (P_1) from 200 kPa to 3500 kPa

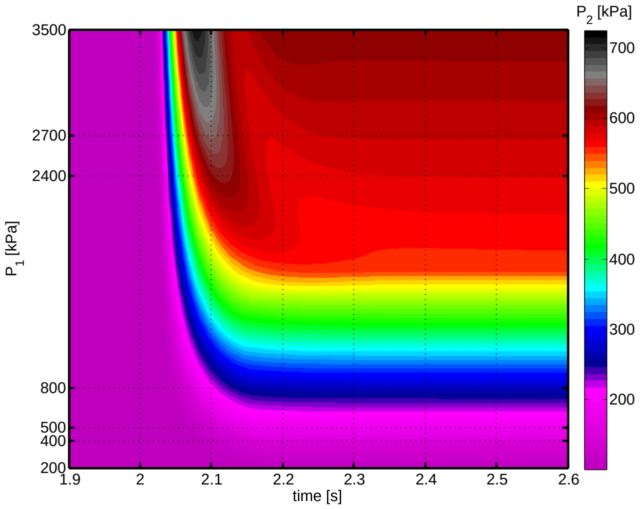

Figure 1.40: P_2 trend - piston with trapezoidal openings

A linear analysis has been performed to evaluate the response in frequency of the valve. The input signal is the P_1, the output signal is the regulated pressure (P_2); the input signal to the valve is shown in figure 1.41(a) and the linearization time is 9 s.
The analysis confirmed that the valve is instable at high inlet pressures, and also the frequency of the instability is compatible with previous results (compare figure 1.41 with figure 1.39(d)). The valve at all other frequency damps the signal oscillation acting as a filter. Considering that the normal speed for a commercial aircraft engine goes from $42\,970\,\mathrm{rad\,s^{-1}}$ to $90\,718\,\mathrm{rad\,s^{-1}}$, and assuming that the bleed pressure has a carrier frequency equal to the engine rotational speed, the stability of the valve is not influenced by the frequency but only by the input pressure level.

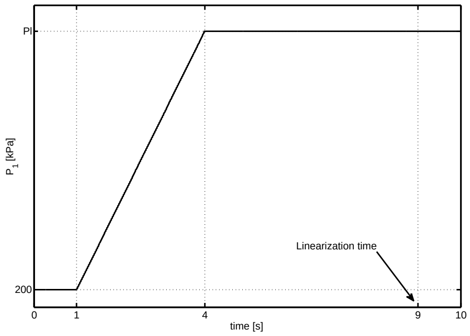

(a) Valve linear analysis input

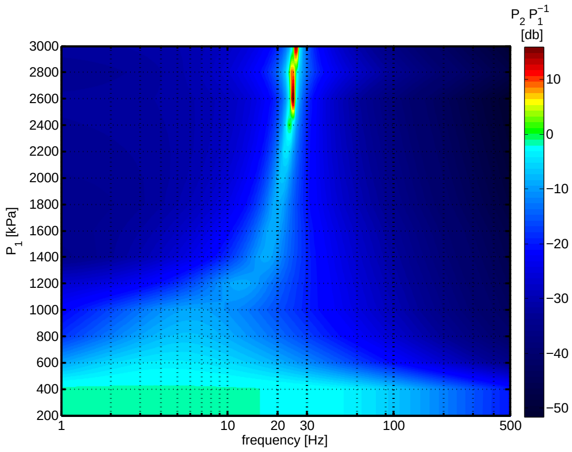

(b) Magnitude

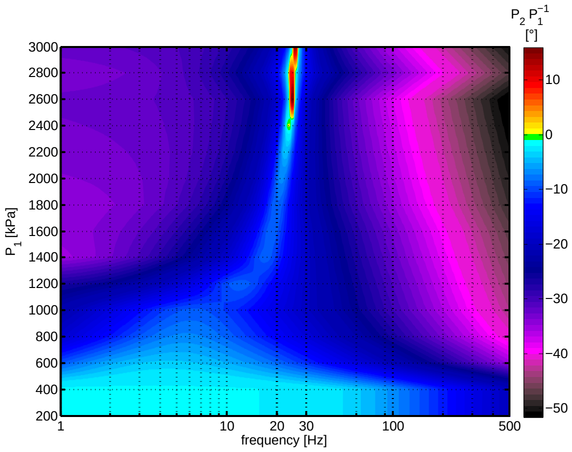

(c) Phase

Figure 1.41: Valve linear analysis, Bode diagram

Chapter 2

Compact Heat exchangers

2.1 Introduction

The typical configuration for the heat exchangers used for airplane air cycle is the plate and fins configuration. This family of heat exchangers grants a big exchange area with limited overall dimensions. The solid construction allows also high operation pressure.
The heat exchangers are generally made of stainless steel or aluminium. The material selection is mainly driven by the maximum operating temperature; if the maximum operating temperature is above 250 °C the aluminium (which combines lightness and good thermal performance) is not used due to the degradation of the material properties over this temperature.

2.1.1 Heat exchanger core geometrical parameters

Figure 2.1 defines the key geometrical parameters of a plate and fin heat exchanger core.[1]. The index *cold* identifies the parameters of cold fluid side, the index *hot* identifies the parameters of the hot fluid side. Three dimensions define the overall envelope of the heat exchanger core:

- Length cold (LC), is the length of the cold fluid channels
- Length hot (LH), is the length of the hot fluid channels
- Length no flow (LNF), is the third dimension which closes the Cartesian axes

The lateral bars (called blocking bars) avoids the mixing of the two fluid flows and from a mechanical point of view, they sustain the pressure forces and the acceleration forces.

---

[1] The general considerations on the influence of the parameters presented in this paragraph are deeply discussed in paragraph 2.2

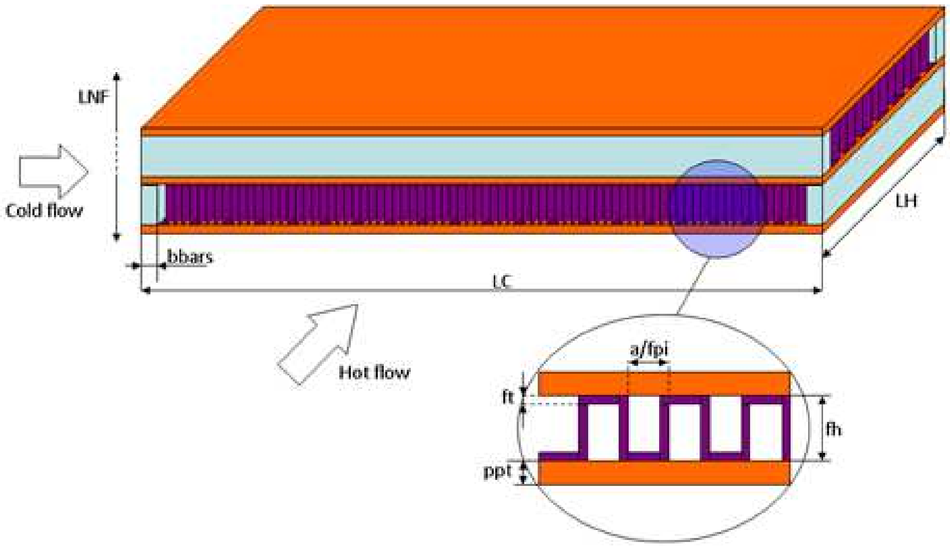

Figure 2.1: Plate and fins heat exchanger geometrical parameters

The parting plates divide the two flows creating the heat exchange area. If the difference of pressure between the two sides is high (as generally happens when one of the two fluids is the outside air) the parting plates have to withstand the differential pressure without any deformation. The first and last parting plates are generally called end plates and are thicker than other parting plates.

The fins should be as thickest as possible. A standard thickness for the fins is 0.0755 mm (generally cannot be smaller).

The fins rate (generally expressed as fins per inch) and the height of the passages are the key parameters of the heat exchanger optimization. The selection of these parameter is a compromise between heat exchange efficiency and core pressure drops. The limitation of these two parameters depends to the heat exchanger manufacturer. The minimum height of the passages goes with difficulty below 2 mm. The number of fins per inch generally is between 16 and 32. Higher fins rate cannot be associated to small passage heights.

2.2 Mathematical model

The mathematical model herein described is strongly based on the approach presented by Kays and London [1984].

2.2.1 Geometrical

The number of layers for cold fluid (n_{cold}) and hot fluid (n_{hot}) is determined by the available LNF ($LNF_{\text{available}}$) using equation 2.2.1. This equation is valid only if the external HX layers are cold. There are two reasons to adopt this configuration:

- performance - generally, the differential pressure available on the cold side is limited (i.e. fan or ejector pump), so an additional passage decreases the pressure drop and increases the cold flow rate increasing the performance of the HX
- human safety - the external surface of the HX reaches lower temperature reducing the risk of injuries.

$$n_{\text{cold}} = n_{\text{hot}} + 1 \tag{2.2.1a}$$

$$n_{\text{hot}} = floor\left(\frac{LNF_{\text{available}} - 4ppt}{fh_{\text{hot}} + fh_{\text{cold}} + 2ppt}\right) \tag{2.2.1b}$$

The LNF of the HX is calculated using equation 2.2.2.

$$LNF = n_{\text{cold}} fh_{\text{cold}} + n_{\text{hot}} fh_{\text{hot}} + ppt(n_{\text{hot}} + n_{\text{cold}}) \tag{2.2.2}$$

The frontal area (A) subjected to the flow is the heat exchanger frontal area (the LNF multiply by LC or LH) minus the frame area (blocking bars plus end parting plate). Equations 2.2.3 are valid if the thickness of the parting plates, which close the heat exchanger, is double of the parting plate thickness.

$$A_{\text{hot}} = (LNF - 4\text{ppt})\frac{LC - (N_{\text{pass}} + 1)\text{bbars}_{\text{hot}}}{N_{\text{pass}}} \tag{2.2.3a}$$

$$A_{\text{cold}} = (LNF - 4\text{ppt})(LH - 2\text{bbars}_{\text{cold}} \tag{2.2.3b}$$

The free flow area (A_{free}) is the frontal area minus the area occupied by the parting plates and by the fins.

$$\begin{aligned} A_{\text{free,hot}} = \quad & n_{\text{hot}} fh_{\text{hot}} \left(1 - \frac{ft_{\text{hot}}}{fh_{\text{hot}}}\right)(1- \\ & + \frac{0.0254 ft_{\text{hot}}}{fpi_{\text{hot}}}\Bigg) \frac{LC - (N_{\text{pass}} + 1)\text{bbars}_{\text{hot}}}{N_{\text{pass}}} \end{aligned} \tag{2.2.4a}$$

$$\begin{aligned} A_{\text{cold,hot}} = \quad & n_{\text{cold}} fh_{\text{cold}} \left(1 - \frac{ft_{\text{cold}}}{fh_{\text{cold}}}\right)(1- \\ & + \frac{0.0254 ft_{\text{cold}}}{fpi_{\text{cold}}}\Bigg) (LH - 2\text{bbars}_{\text{cold}}) \end{aligned} \tag{2.2.4b}$$

The total heat exchanger area (A_{tot}) is the wet surface of each fluid channel multiply by the number of channels.

$$\begin{aligned} A_{\text{tot,hot}} = & \left(2 + \frac{2fpi_{\text{hot}}\left(fh_{\text{hot}} - 2ft_{\text{hot}}\right)}{0.0254}\right)\left(\frac{LC}{N_{\text{pass}}} - \right. \\ & \left. + \frac{(N_{\text{pass}} + 1)\text{bbars}_{\text{hot}}}{N_{\text{pass}}}\right) n_{\text{hot}} LH \qquad (2.2.5a) \\ A_{\text{tot,cold}} = & \left(2 + \frac{2fpi_{\text{cold}}\left(fh_{\text{cold}} - 2ft_{\text{cold}}\right)}{0.0254}\right)\left(LH - \right. \\ & \left. + 2\text{bbars}_{\text{cold}}\right) n_{\text{cold}} LC \qquad (2.2.5b) \end{aligned}$$

There are other 2 geometrical parameters driving the sizing of a cross flow heat exchanger:

- the hydraulic diameter (d_{hyd}) (sometime defined also characteristic length of the exchange) calculated using equations 2.2.6
- the ratio between finned area and total area (rfa)

$$d_{\text{hyd,hot}} = \frac{\left(fh_{\text{hot}} - ft_{\text{hot}}\right)\left(0.0254 - fpi_{\text{hot}}fh_{\text{hot}}\right)}{2\left(0.0254 + fpi_{\text{hot}}fh_{\text{hot}} - 2fpi_{\text{hot}}fh_{\text{hot}}\right)} \qquad (2.2.6a)$$

$$d_{\text{hyd,cold}} = \frac{\left(fh_{\text{cold}} - ft_{\text{cold}}\right)\left(0.0254 - fpi_{\text{cold}}fh_{\text{cold}}\right)}{2\left(0.0254 + fpi_{\text{cold}}fh_{\text{cold}} - 2fpi_{\text{col}}fh_{\text{cold}}\right)} \qquad (2.2.6b)$$

$$\text{rfa}_{\text{hot}} = \frac{fpi_{\text{hot}}\left(fh_{\text{hot}} - ft_{\text{hot}}\right)}{0.0254 + fpi_{\text{hot}}fh_{\text{hot}} - 2fpi_{\text{hot}}ft_{\text{hot}}} \qquad (2.2.7a)$$

$$\text{rfa}_{\text{cold}} = \frac{fpi_{\text{cold}}\left(fh_{\text{cold}} - ft_{\text{cold}}\right)}{0.0254 + fpi_{\text{cold}}fh_{\text{cold}} - 2fpi_{\text{cold}}ft_{\text{cold}}} \qquad (2.2.7b)$$

2.2.2 Thermodynamic calculations

The approach used to size the heat exchanger is based on the $\epsilon - N_{\text{tu}}$ method. The heat exchanger effectiveness (ϵ) is defined as the ratio between the heat transfer rate and the maximum heat transfer rate achievable (see equation 2.2.8a).

$$\begin{aligned} \epsilon &= \frac{q}{q_{\max}} && (2.2.8a) \\ &= \frac{C_{\text{hot}}(T_{\text{in,hot}} - T_{\text{out,hot}})}{C_{\min}(T_{\text{in,hot}} - T_{\text{in,cold}})} && (2.2.8b) \\ &= \frac{C_{\text{cold}}(T_{\text{in,cold}} - T_{\text{out,cold}})}{C_{\min}(T_{\text{in,hot}} - T_{\text{in,cold}})} && (2.2.8c) \end{aligned}$$

$C_{\min}$ is the smaller between C_{hot} and C_{cold}.

The ϵ for the type of HX under analysis is approximate by equation 2.2.9 and increased, to take into account the multipass configuration, using equation 2.2.10 (in equation ϵ_p is the effectiveness calculated using equation 2.2.9).

$$\epsilon = \sum_{i=0}^{30} \left(\frac{2 - e^{-\mathrm{NTU}} \sum_{j=0}^{i} \left(\frac{\mathrm{NTU}^j + (C_C \mathrm{NTU})^j}{j!} \right)}{\mathrm{NTU} C_C} \right) \tag{2.2.9}$$

$$\epsilon = \left(\left(\frac{1 - C_C * \epsilon_p}{1 - \epsilon_p} \right)^{n_{\text{pass}}} - 1 \right) \left(\left(\frac{1 - C_C * \epsilon_p}{1 - \epsilon_p} \right)^{n_{\text{pass}}} - C_C \right)^{-1} \tag{2.2.10}$$

Where n_{pass} is number of passages (hot fluid).
Equation (2.2.11) reports the definition of Number of heat transfer unit of a HX (N_{tu}). The d_d is the distribution factor, a coefficient that reduces the performance of the HX to take into account flow maldistribution due to the header design[2].

$$N_{\text{tu}} = \frac{\hat{U} A_{\text{tot,hot}}}{C_c(1 + d_d)} \tag{2.2.11}$$

To calculate the overall heat transfer coefficient ($\hat{U}$) the thermal-convection heat transfer coefficient ($\hat{\alpha}$) and the efficiency of the fins (η_{fin}) for both cold and hot fluids have to be calculated. The calculation of these coefficients is based on experimental data summarized as dimensionless parameters; the dimensionless parameters are:

$$\mathrm{Re} = \frac{4 d_{\text{hyd}} m}{A_{\text{free}} \mu} \tag{2.2.12a}$$

$$\mathrm{St} = \frac{A_{\text{free}} \hat{\alpha}}{c_p m} \tag{2.2.12b}$$

$$\mathrm{Pr} = \frac{\mu c_p}{\hat{k}_t} \tag{2.2.12c}$$

Prandtl number (Pr) is, as first approximation, only a function of the fluid type. The product $\mathrm{StPr}^{\frac{2}{3}}$ is obtained by experimental maps. Several authors developed maps for various type of fins configuration (see Kays and London [1984]). In this publication the Stanton number (St) is calculated using equation 2.2.13. This equation derives from the experience of heat exchanger manufactures and it is valid for:

- wavy fins
- $1e2 \leq \mathrm{Re} \leq 2e5$
- $18 \leq fpi \leq 32$

---

[2] generally set to 0.5

$$\mathrm{StPr}^{\frac{2}{3}} = \left(0.07581\mathrm{Re}^{-0.1386} - 0.01498\right)\left(\frac{18}{fpi}\right)^{.234} \tag{2.2.13}$$

The $\hat{\alpha}$ is calculated re-arranging equation 2.2.12b.

$$\hat{\alpha} = \frac{\mathrm{St}mc_p}{\mathrm{Pr}^{\frac{2}{3}}A_{\mathrm{free}}} \tag{2.2.14}$$

The η_{fin} is calculated using the standard equations for finned surfaces (see Bonacina et al. [1989] and equations 2.2.15).

$$m = \sqrt{\frac{2\hat{\alpha}}{ft\hat{k}_{t\mathrm{fin}}}} \tag{2.2.15a}$$

$$L = \frac{fh}{n}\left(\frac{n-1}{2}+1\right) \tag{2.2.15b}$$

$$\eta_{\mathrm{fin}} = 1 - \left(1 - \mathrm{rfa}\frac{\tanh\left(mL\right)}{mL}\right) \tag{2.2.15c}$$

The $\hat{U}$ is calculated using equation 2.2.16.

$$\hat{U} = \left(\frac{1}{\eta_{\mathrm{fin,hot}}\hat{\alpha}_{\mathrm{hot}}} + \frac{ppt}{\hat{k}_{t\mathrm{fin}}} + \frac{A_{\mathrm{tot,hot}}}{A_{\mathrm{tot,cold}}\eta_{\mathrm{fin,cold}}\hat{\alpha}_{\mathrm{cold}}}\right)^{-1} \tag{2.2.16}$$

The temperatures at the outlet of the HX are calculated re-arranging equation 2.2.8b for the hot side (equation 2.2.17a) and the outlet temperature of the cold fluid is calculated imposing the same heat flow rate for the hot side and the cold side (equation 2.2.17b).

$$T_{\mathrm{out,hot}} = T_{\mathrm{in,hot}} - \frac{C_{\mathrm{min}}\epsilon(T_{\mathrm{in,hot}} - T_{\mathrm{in,cold}})}{m_{\mathrm{hot}}c_{p\mathrm{hot}}} \tag{2.2.17a}$$

$$T_{\mathrm{out,cold}} = T_{\mathrm{in,cold}} + \frac{m_{\mathrm{hot}}c_{p\mathrm{hot}}(T_{\mathrm{in,hot}} - T_{\mathrm{out,hot}})}{m_{\mathrm{cold}}c_{p\mathrm{cold}}} \tag{2.2.17b}$$

2.2.3 Pressure drops calculations

The pressure drops of the heat exchanger are written as loss of dynamic pressure (P_{dyn}). The P_{dyn} on each side of the HX is calculated using equation (2.2.18).

$$P_{\mathrm{dyn}} = \frac{(mA_{\mathrm{free}})^2}{2\rho_{\mathrm{in}}} \tag{2.2.18}$$

The HX pressure drops can be split up into 4 groups:

- core entrance pressure drops
- core pressure drops

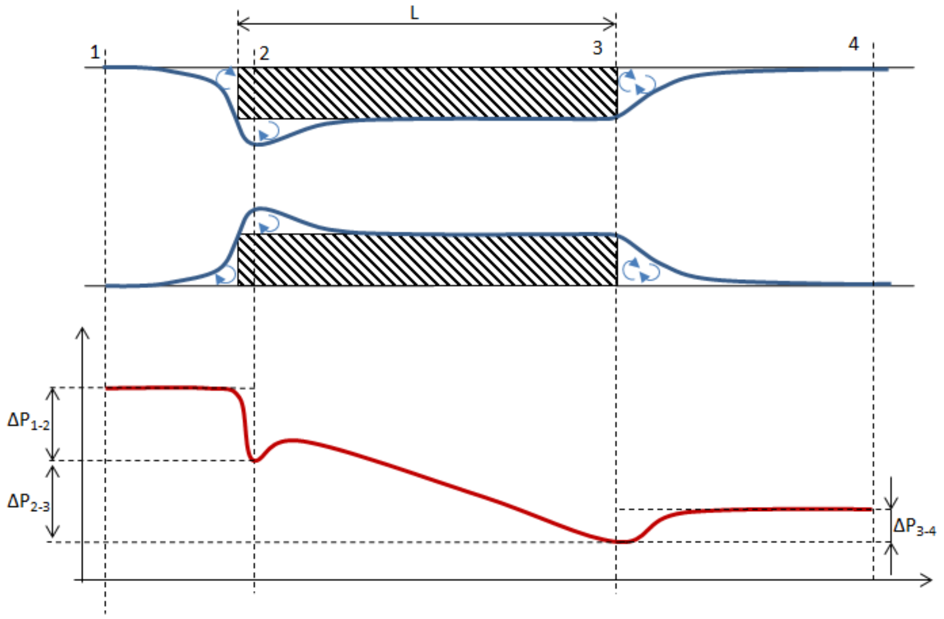

Figure 2.2: HX core pressure losses trend

- core exit pressure drops
- headers pressure drops

In this work the pressure drops of the HX headers are considered one order of magnitude lower than the core pressure drops and so neglected.
The core entrance pressure drops includes either the friction losses associated with fluid flow area change and the friction losses associated to the vena contraction that follows the sudden contraction. The pressure drops associated to the flow area change are calculated assuming that the fluid is incompressible (thus the flow speed far from sonic conditions) and isothermal; under these assumptions the Bernoulli formula can be rearranged as shown in equation 2.2.19.

$$\Delta P_{1\text{-}2'} = P_{\text{dyn}} \left(1 - \left(\frac{A_{\text{free}}}{A}\right)^2\right) \tag{2.2.19}$$

The contribution due to the vena contraction is computed using an entrance dynamic pressure recovery factor (K_c). This factor is a function of the geometrical configuration of the HX. Figure 2.3(a) shows the experimental maps used to extrapolate the K_c for the calculation. The total pressure drop of core entrance are:

$$\Delta P_{1\text{-}2} = P_{\text{dyn}} \left(1 - \left(\frac{A_{\text{free}}}{A}\right)^2 + K_c\right) \tag{2.2.20}$$

Small ratio of A_{free} to A implies higher pressure drops. Ratio of A_{free} to A near to 1 decreases the pressure drop.
The core exit pressure drops are similar to the core entrance pressure drops. In this case the positive change of area implies a reduction of fluid speed (the area increases), so a pressure rise. The sudden flow area variation creates a free flow expansion; the flow separation produces irreversible pressure losses which are calculated defining, from experimental maps (see 2.3(b)), an exit dynamic pressure recovery factor (K_e). The core exit pressure drops are calculated using equation 2.2.21.

$$\Delta P_{\text{3-4}} = P_{\text{dyn}} \left(1 - \left(\frac{A_{\text{free}}}{A}\right)^2 - K_e\right) \frac{\rho_{\text{in}}}{\rho_{\text{out}}} \tag{2.2.21}$$

The ratio of ρ_{in} to ρ_{out} is used to normalize the equation to the same P_{dyn} of other equations.
Shah and Dušan [2003] developed the formulas to calculate the contribution of the core pressure drops (see equation 2.2.22). The core pressure drops includes either the frictional losses associated with fluid flow over the heat transfer surface and the momentum effect. Respect to the formula developed by Shah equation 2.2.22 includes the HX number of passages ($Npass$).

$$\Delta P_{2-3} = \underbrace{2\left(\frac{\rho_{\text{in}}}{\rho_{\text{out}}} - 1\right)}_{\text{momentum effect}} + \underbrace{f_f \frac{LNpass}{d_{\text{hyd}}} \frac{\rho_{\text{in}}}{\overline{\rho}}}_{\text{core friction}} \tag{2.2.22}$$

The Fanning factor (f_f) is calculated or using the maps developed by several researchers or by data available from HX manufacturers. For wavy-fins a good equation approximates the pressure drops of the core is the 2.2.23.

$$f_f = \begin{cases} 0.060\text{Re}^{+0.100} \left(\dfrac{18}{fpi}\right)^{0.45} \\ 0.027\text{Re}^{-0.125} \left(\dfrac{18}{fpi}\right)^{0.45} \end{cases} \tag{2.2.23}$$

Finally the pressure drops of an HX are obtained summing all the contributions.

$$\Delta P = P_{\text{in}} P_{\text{dyn}} \left(\underbrace{1 - \left(\frac{A_{\text{free}}}{A}\right)^2 + K_c}_{\text{core entrance}} + \underbrace{2\left(\frac{\rho_{\text{in}}}{\rho_{\text{out}}} - 1\right)}_{\text{momentum effect}} + \right.$$

$$\left. + \underbrace{f_f \frac{LNpass}{d_{\text{hyd}}} \frac{\rho_{\text{in}}}{\overline{\rho}}}_{\text{core friction}} - \underbrace{\left(1 - \left(\frac{A_{\text{free}}}{A}\right)^2 - K_e\right) \frac{\rho_{\text{in}}}{\rho_{\text{out}}}}_{\text{core exit}} \right) \tag{2.2.24}$$

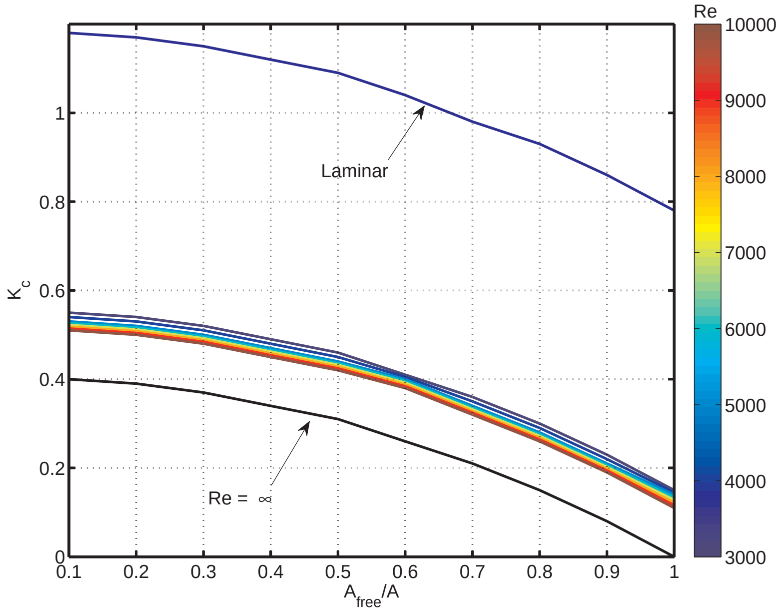

(a) entrance pressure loss coefficient (K_c)

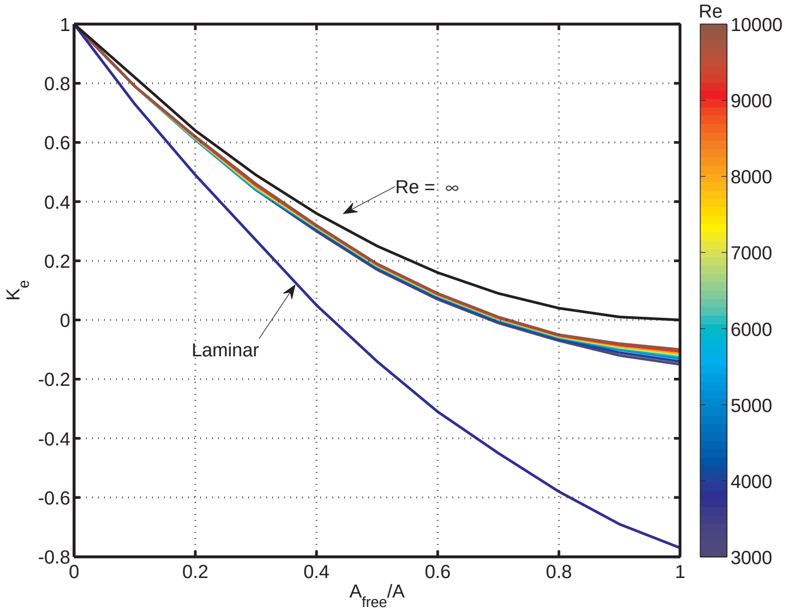

(b) exit pressure loss coefficient (K_e)

Figure 2.3: HX entrance and exit pressure loss coefficients, From Kays and London [1984]

Parameter	Unit	HX
LNF	mm	144.0
LH	mm	114.0
LC	mm	88.5
Fin Type		Wavy
fh_{hot}	mm	2.94
fpi_{hot}	in^{-1}	24
ft_{hot}	mm	0.0755
fh_{cold}	mm	8.92
fpi_{cold}	in^{-1}	16
ft_{cold}	mm	0.0755
$Npass$		2
ppt	mm	0.4
Material		Al
Fluid Cold side		air
Fluid Hot side		EG60W40

Table 2.1: Tested HX geometrical characteristics

2.3 HX experimental data

2.3.1 tests description

One HX has been tested to verify the outputs of the mathematical model. The HX tested is a liquid-to-air heat exchanger used to transfer the cooling effect of a bootstrap cycle to a secondary fluid. The hot fluid is Dowcal10®[3] mixed with water (40% of water and 60% of Dowcal10), the cold fluid is air. The geometrical characteristics of the HX are detailed in table 2.1.
The tests have been performed setting, on the air side, an inlet temperature of $19 \pm 3\,°\text{C}$ and an inlet pressure of $95 \pm 5\,\text{kPa}$, on the fluid side, an inlet temperature of $60 \pm 1\,°\text{C}$ and an inlet pressure of $400 \pm 15\,\text{kPa}$.
The hot flow rate has been set at three different values: $0.15\,\text{kg}\,\text{s}^{-1}$, $0.25\,\text{kg}\,\text{s}^{-1}$ and $0.35\,\text{kg}\,\text{s}^{-1}$. Foe each of these values a sweep of cold flow rate has been done; the sweep goes from $0.2\,\text{kg}\,\text{s}^{-1}$ to $0.7\,\text{kg}\,\text{s}^{-1}$ with a step of $0.1\,\text{kg}\,\text{s}^{-1}$.
The test has been performed setting the parameters, waiting for stabilization and then recording all the parameters for 120 s.

2.3.2 HX test rig

The test rig used is composed by an air circuit and a liquid circuit.

---

[3] an ethylene glycol-based heat transfer fluid. for further information and fluid properties see http://www.dow.com

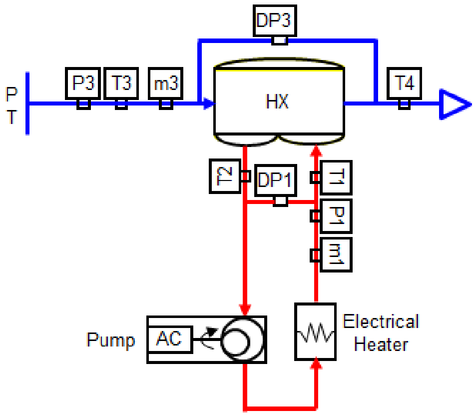

Figure 2.4: HX test rig schematic

The air side of the HX is connected to a pneumatic pressure source; the source provides pressurized air at ambient temperature (uncontrolled). The HX outlet (air side) is connected to a short duct, where the outlet temperature is measured, and then the air is discharged to ambient. The air flow rate is controlled by modulating the pressure at HX inlet.

The liquid side of the HX is connected to a liquid loop. A variable displacement pump forces the liquid to flow into the loop. A variable electrical heater installed before the HX heats up the liquid temperature at the HX inlet; the electrical heater acts also as reservoir.

Figure 2.4 shows the schematic of the test rig.

All the thermodynamic parameters (temperature, pressure and flow rate) are measured at the HX interfaces. The pressures are read using 4 static port annular chambers. Only one temperature sensor has been installed at each interface: the small dimensions of the HX does not allow the installation of multiple temperature sensors.

Table 2.2 summarizes the sensors utilized and their characteristics.

2.3.3 Measurement uncertainty evaluation

The accuracy of the sensors are reported in table 2.2.

The measured value is calculated making the average on the acquisition window of 120 s; the measurement uncertainty (δ) is calculated using equation (2.3.1), where $\delta_{\text{measurement}}$ is two times the standard deviation calculated over the acquisition window, and δ_{sensor} is the accuracy of the sensor.

$$\delta = \sqrt{\delta^2_{\text{measurement}} + \delta^2_{\text{sensor}}} \tag{2.3.1}$$

Pressure sensors are affected also by error due to temperature. This is the major component of a pressure measurement uncertainty; adding this error

Sensor	Parameter	Unit	Sensor Type	Sensor Range	Accuracy
T1	$T_{\text{in,hot}}$	°C	PT100	0 to 100	±0.5
T2	$T_{\text{out,hot}}$	°C	PT100	0 to 100	±0.5
P1	$P_{\text{in,hot}}$	kPa	ROSEMOUNT	0 to 1e3	±10
DP1	ΔP_{hot}	kPa	FUJI	0 to 100	±1
m1	m_{hot}	$\text{kg}\,\text{s}^{-1}$	MICROMOTION CNF100	0.1 to 1	±0.005
T3	$T_{\text{in,cold}}$	°C	PT100	0 to 100	±0.5
T4	$T_{\text{out,cold}}$	°C	PT100	0 to 100	±0.5
P3	$P_{\text{in,cold}}$	kPa	FUJI	0 to 250	±2.5
DP3	ΔP_{cold}	kPa	FUJI	0 to 50	±0.5
m3	m_{cold}	$\text{kg}\,\text{s}^{-1}$	MICROMOTION CNF100	0.1 to 1	±0.005

Table 2.2: HX test rig sensors characteristics. The accuracy reported in table includes the combined non-linearity, hysteresis and repeatability.

to the accuracy of the sensor, the total error band on the measured pressure is ±1.5%.
The uncertainty on the ϵ ($\delta\epsilon$) is calculated propagating the uncertainty on the single measurements by applying formula proposed by Kline and McClintock [1953] at equation (2.2.8b) (see equation (2.3.2)).

$$\delta\epsilon = \left(\left(\frac{(T_{\text{hot,out}} - T_{\text{cold,in}})}{(T_{\text{cold,in}} - T_{\text{hot,in}})^2} \delta T_{\text{hot,in}} \right)^2 + \left(\frac{\delta T_{\text{hot,out}}}{T_{\text{cold,in}} - T_{\text{hot,in}}} \right)^2 + + \left(\frac{(T_{\text{hot,in}} - T_{\text{hot,out}})}{(T_{\text{cold,in}} - T_{\text{hot,in}})^2} \delta T_{\text{cold,in}} \right)^2 \right)^{\frac{1}{2}} \tag{2.3.2}$$

The uncertainty calculated using equation (2.3.2) takes into account only the direct effects of the temperature measurement on the ϵ, but it neglects the influence of other parameters (like measurements of the flow rates, real HX geometrical parameters, headers influence, etc.). These parameters are taken into account adding to the uncertainty, calculated using equation (2.3.2), an additional contribution of the 2%.

2.3.4 HX Model validation

Two parameters have been used to evaluate the matching between the experimental results and the mathematical model prediction:

- ΔP, the pressure difference across the core
- heat exchanger effectiveness

The comparison of ϵ is shown in figure 2.5(b). The mathematical model results are fully inline with the experimental results.
The $\delta\epsilon$ increases with the increase of the hot fluid flow rate; at high hot flow rate the hot fluid temperature difference across the HX is small and so the uncertainty increases.
The comparison of ΔP is shown in figure 2.5(a). The ΔP is presented as a function of the corrected mass flow rate (m_{corr}) defined as per equation 5.2.7a.

$$m_{\text{corr}} = \frac{m\sqrt{T_{\text{in}}}}{P_{\text{in}}} \tag{2.3.3}$$

Also in this case the mathematical model results are inline with the experimental results; The discrepancy is more evident at very low m_{corr}. This is due to the fact that low m_{corr} means also low Reynold number (Re) and equation (2.2.23) starts to be marginal.

Other HXs available data

The performance of the model has been also verified against the experimental data of other HXs. These data comes from tests not dedicated to the HX performance evaluation, and so the points available are limited and only the temperature measurements are available.

The first HX (*LHX*) is a liquid-to-air HX similar to the one already described. Table 2.3 reports the main geometrical characteristics of this HX.
The tests have been performed with the following boundary conditions. The hot fluid inlet temperature is set to 31 ± 4 °C, and the hot flow rate is set to $250 \pm 5\,\mathrm{g\,s^{-1}}$; since this part of the HX is connected to a loop similar to the one described in 2.3.2, the input parameters are easily set. The cold side of the HX is connected to the turbine outlet of a bootstrap cycle and since the turbine outlet temperature and turbine flow rate are strictly correlated, only one of these two parameters can be fully controlled. The cold flow rate varies from $50\,\mathrm{g\,s^{-1}}$ to $250\,\mathrm{g\,s^{-1}}$ and cold side air temperature varies from 7.4 °C to −36.6 °C.
The scatter of experimental points at $100\,\mathrm{g\,s^{-1}}$ is very low, indicative of a low measurement uncertainty[4]. At this flow rate the mathematical model predicts an ϵ slightly higher than the test results, the deviation of the model from the experimental data is within the 10 %.

---

[4] note that a systematic error could still be present

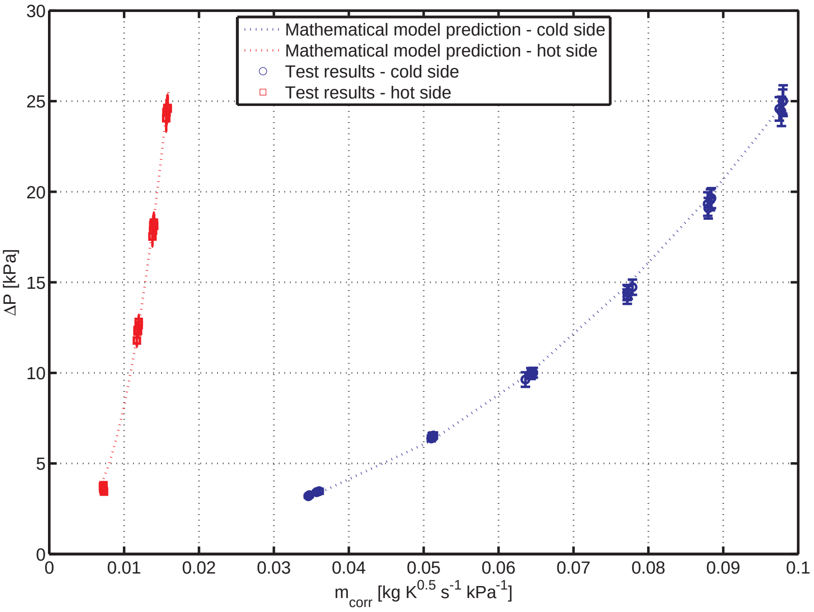

(a) HX Pressure drop hot and cold side

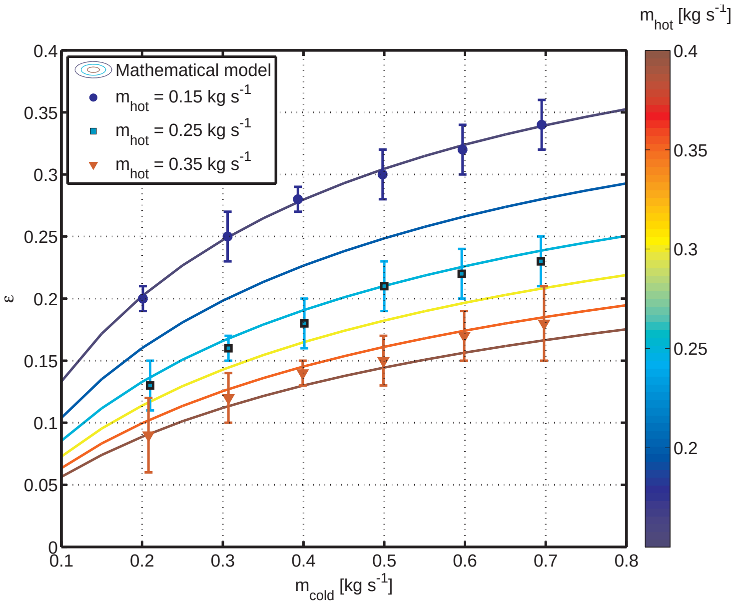

(b) ϵ of HX. The ϵ is calculated using equation (2.2.8b)

Figure 2.5: HX: comparison between mathematical model and test results

Parameter	Unit	LHX	IHX
LNF	mm	175.0	175.0
LH	mm	200.0	200.0
LC	mm	100.0	150.0
Fin Type		Wavy	Wavy
fh_{hot}	mm	1.5	3
fpi_{hot}	in^{-1}	22	32
ft_{hot}	mm	0.1	0.1
fh_{cold}	mm	5.35	3.0
fpi_{cold}	in^{-1}	32	32
ft_{cold}	mm	0.1	0.1
$Npass$		2	2
ppt	mm	0.4	0.4
Material		Al	Al
Fluid Cold side		air	air
Fluid Hot side		EG60W40	air

Table 2.3: Other tested HXs geometrical characteristics

At higher cold fluid flow rates the scatter of experimental data appreciably increases. The model better matches the clouds of points (the curve pass in the center of the cloud), and the deviation of the experimental data from the mathematical model prediction is lower than the 10 %.

The second HX (IHX) is an air-to-air HX used a recovery heat exchanger in a bootstrap system. The particularity of this HX is that in normal operation the hot and cold fluid flow rates are equal, since the same air pass as hot fluid and then, after been processed by the turbine and an intermediate HX re-enter into the IHX as cold fluid. Table 2.3 reports the main geometrical characteristics of this HX.
The tests have been performed with the following boundary conditions. 3 level of flow rate have been tested[5]: $0.1\,\text{kg}\,\text{s}^{-1}$, $0.2\,\text{kg}\,\text{s}^{-1}$, $0\,\text{kg}\,\text{s}^{-1}$ and $25\,\text{kg}\,\text{s}^{-1}$; The cold side inlet temperature was kept around 24 °C. The test rig does not allow any adjustment of the HX hot side inlet temperature; this parameter varies during the test from 81 °C to 240 °C.
Also in this case the scatter of the experimental point is very low: at intermediate flow rate ($0.2\,\text{kg}\,\text{s}^{-1}$) the scattering is mainly due to the difficulty of set the flow rate to the desired value; different cold flow rate means different hot fluid flow rates and so the experimental point does not move along the mathematical model curve (for which the hot fluid flow rate is set at $0.2\,\text{kg}\,\text{s}^{-1}$) but jump to other hot flow rate curves.

---

[5] remember that for this HX the hot and cold flow rate are the same

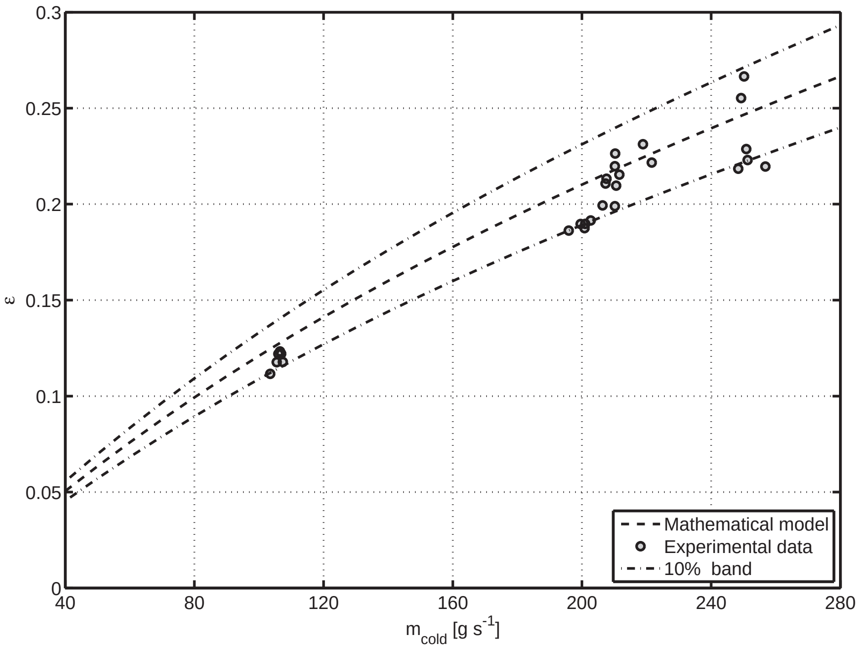

Figure 2.6: LHX test and mathematical model results. The ϵ is calculated using equation (2.2.8b)

The deviation of the mathematical model prediction from the experimental results is around the 10 %, confirming the results of the previous HX. The model is slightly optimistic predicting an ϵ greater than the output of the tests.

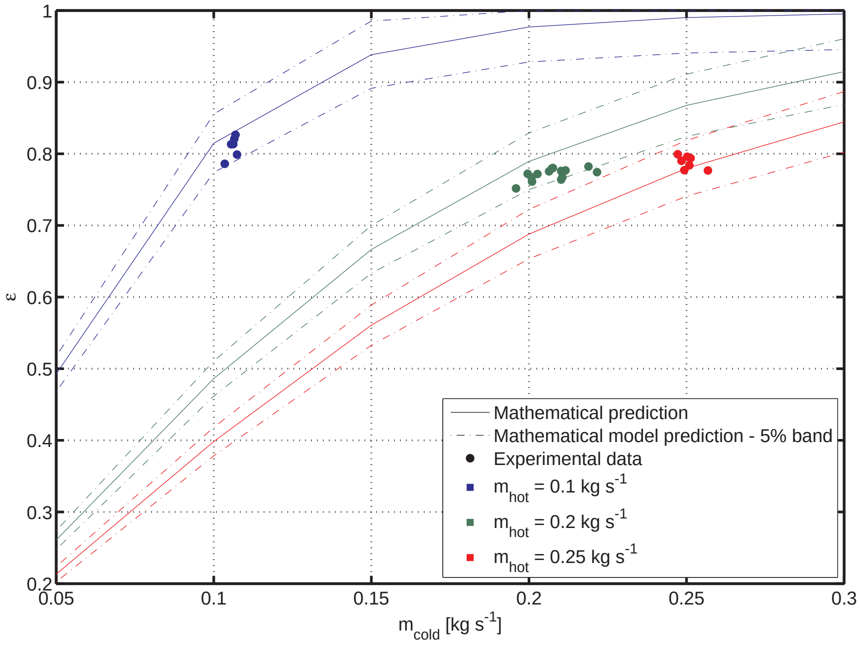

Figure 2.7: IHX test and mathematical model results. The ϵ is calculated using equation (2.2.8b)

Chapter 3

Anti-ice systems

The icing is a issue for commercial aircrafts which fly at high altitude. The temperature, when the airplane is in cruise, can reach −40 °C with a relative humidity near 0 %. The airplane flies in this conditions for all the cruise phase and so the temperature of the external surfaces of the airplane goes below 0 °C. In the descent phase the airplane could pass through altitudes where visible moisture is present (high relative humidity) and the total air temperature is below 10 °C: these are the typical icing conditions since the wet air imping the cold surface of the aircraft creating ice on the surfaces (see Mason et al. [2006]). The icing grows up on the wings leading edge and on the nacelle inlet creating performance degradation (loss of lift) and dangerous conditions (Engine ice ingestion). On north climate the aircrafts face with similar issues on the climbing phase (in this case the surfaces of the airplane are cooled down due to the low OAT on ground).

One of the techniques used to avoid these dangerous conditions is the warm-up of the wing leading edge and the nacelle inlet using the hot air bled from the engine. The air is bled typically from the 4^{th} stage of the compressor; one shut off valve (a pneumatic solenoid valve for reliability reasons) controls (only on/off) the hot air flow rate to the piccolo tube that creates the jets which impinge the wing/nacelle surfaces. The hot air jets warms up the nacelle surface over the sublimation temperature avoiding the formation of ice on the surfaces. The air is then blown away from the rear part of the wing/nacelle.

On new generation aircraft the engine bleed port is moving to higher compressor stage (i.e. from 4^{th} to 6^{th} compressor stage), which means an increase of bleed air temperature and pressure levels; in the same time the leading edges material is changing from stainless steel to aluminium or composite materials (for weight and cosmetic reasons). These new aspects imply a more precise control of the bleed flow rate to keep the leading edge temperature under the temperature where the performance of the material start to degrade (for aluminum is around 250 °C).

The need of new control techniques is also connected to the concept of "Green Aircraft", or for the airlines to the reduction of fuel consumption. In fact, the anti-ice system, which bled air from the engine, is one of the "key energy consumer" with all other system which uses air bled from the engine. Berlowitz [2010] shows that for a 40 MW engine, the power used for the pneumatic secondary power systems (ECS and anti-ice system) is around 1.2 MW, when all other secondary power systems (Electrical, hydraulic and mechanical systems) uses only 540 kW. Evans [1991] studied how the bleed air usage, influence the performances of an aircraft engine: he found that the specific fuel consumption increases approximately of 1 % for each percentage of bleed extraction.

3.1 Nacelle leading edge thermodynamic model

Several studies describes how to model the piccolo tube and the aero-thermal dynamics behavior of the engine leading edge when the anti-ice system is operating (see at example [Pellissier et al., 2011], [HHT and Hua, 2004], [Kato, 2006]); these models are very detailed and based on CFD analysis. To analyze and optimize the overall anti-ice system architecture a more simple model (0d model) of the nacelle is sufficient, keeping the optimization of the bleed air distribution split from the piccolo tube optimization problem.
The temperature of the nacelle is calculated using equation 3.1.1

$$\frac{dT_{nacelle}}{dt} = \frac{q_{ext} + q_{int}}{Mc_p} \tag{3.1.1}$$

q_{ext} is the heat exchanged between the nacelle and the external ambient, q_{int} is the heat exchanged between the nacelle and the anti-ice system, both are calculated with equation 3.1.2.

$$q = \kappa A(OAT - T_{nacelle}) \tag{3.1.2}$$

The heat exchange coefficient (κ) for the external surface of the nacelle has been estimated using equation 3.1.3, which is an approximated modified Reynolds analogy for a flat-plate (see Bertin [2002]).

$$Nu = 0.0292Re^{0.8}Pr^{1/3} \tag{3.1.3}$$

The κ for the internal surface of the nacelle has been estimated using equation 3.1.4. This equation derives from Goldstein et al. [1986] test results reducing the effect of the impingement to take into consideration the heat transfer also on the surfaces not directly heated by the jets. (see Massoud [2001] for a review of jet heat exchange principles)

$$Nu = 0.01Re^{0.75} \tag{3.1.4}$$

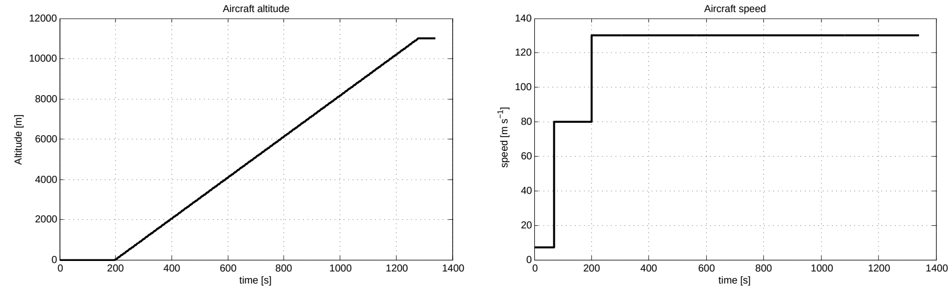

(a) Aircraft altitude **(b)** Aircraft speed

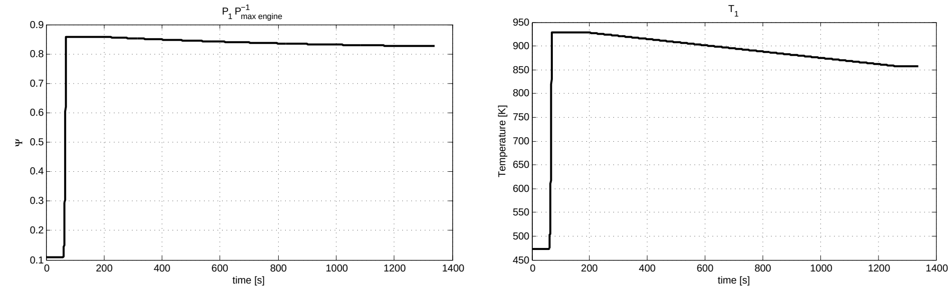

(c) $P_1 P^{-1}_{max\ engine}$ **(d)** T_1

Figure 3.1: Anti-ice systems - Take off simulation input profiles

The atmosphere model used to calculate the *OAP* and the *OAT* is based on [ICAO, 1993], but uses the simplified equations 4.1.1 and 4.1.2.

3.2 Anti-Ice system architectures

Using the mathematical model of the valves described in chapter 1 and adding a simple of model of the nacelle leading edge (see 3.1) is possible to analysis the performance of the various possible anti-ice system architectures. Two operating conditions have been taken into account:

- take-off and climbing (see simulation profiles in figure 3.1)
- descent and landing (see simulation profiles in figure 3.2).

Figure 3.3 shows the two typical configurations for anti-ice systems. The only difference between the two configurations is the type of control valve adopted: on the first configuration is a SOV, on the second configuration is a PRSOV.

Both the architectures are able to maintain the engine leading edge temperature over 0 °C in the simulated cases (see figure 3.4(a)). In the descent and landing case the performance of the two architectures are coincident since the P_{bleed} is lower than the PRSOV regulating pressure (set around

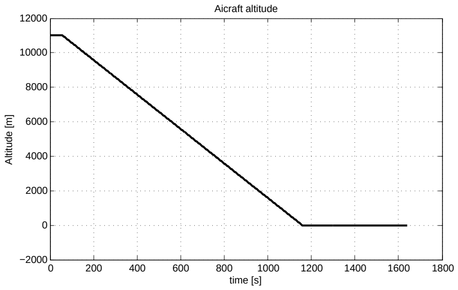

(a) Aircraft altitude **(b)** Aircraft speed

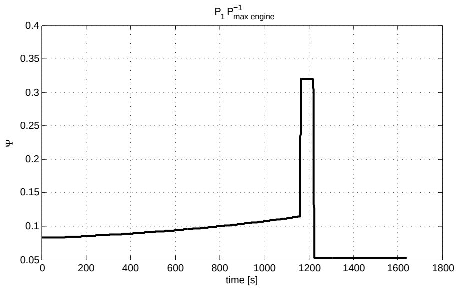

(c) $P_1 P^{-1}_{max\ engine}$ **(d)** T_1

Figure 3.2: Anti-ice systems - Descent simulation input profiles

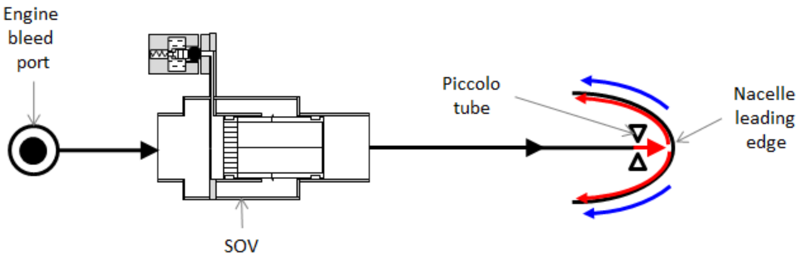

(a) architecture 1: SOV

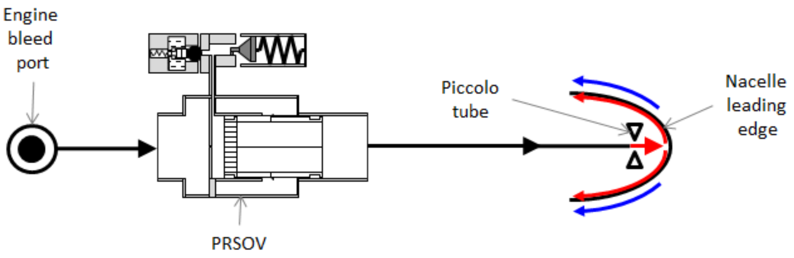

(b) architecture 2: PRSOV

Figure 3.3: Anti-ice system architectures

375 kPa); when the pressure rises over this threshold (reverse thrust) the PRSOV partially closes cutting the inlet pressure at piccolo tube, and so (see equation (1.2.3)) limiting the flow rate bled from the engines. The SOV does not close when the pressure rise and so the architecture 1 bled more air from the engine than the architecture 2.

The behavior of the two architectures during take-off and climbing is similar to the descent and landing case behavior, but since in this case the bleed pressure and temperature are dramatically high, the performance difference between the two architectures is more evident (see figure 3.4(b)). At the beginning of the simulation (first 60 s) the two architecture are equivalent: the engine is in idle conditions and the P_{bleed} is lower than the PRSOV regulating pressure. During acceleration (60 s to 70 s) the P_{bleed} increases going over the PRSOV regulating point; the valve partially closes keeping the pressure at piccolo tube inlet constant. The mass flow rate decreases a little bit since the temperature at piccolo tube inlet increases dramatically (more than 200 °C). The system equipped with a SOV does not limit the pressure at piccolo tube inlet and so the flow rate bled is very high. For both the architecture the flow rate is constant during the climbing phase; the temperature of the leading edge decreases because of the decrease of the OAT with the altitude (see equation (4.1.1)).

The fuel consumption increases of 1 % for each percentage of bleed air extraction (see Evans [1991]), so an airplane equipped with an anti-ice system adopting a SOV consume more fuel than an airplane equipped with an anti-ice system adopting a PRSOV when the anti-ice system is active[1].

3.3 Optimized anti-ice system

An anti-ice system equipped with a PRSOV is more efficient (in terms of fuel consumption) than a anti-ice system equipped with a SOV, but it still wastes a lot of energy since it brings the engine leading edge over 150 °C when a temperature of 65 °C[2] is sufficient to avoid the ice formation on the surfaces.

A more "green" anti-ice system can be realized creating an active control on the engine leading edge temperature.

To introduce an active control the PRSOV has to be replaced with a Flow Modulating and Shut-Off Valve (FMSOV): this type of valve uses a proportional solenoid to control the pressure inside the reference chamber and so the pressure downstream the valve.

When the P_{bleed} and T_{bleed} are elevated the control commands the FMSOV to close reducing the bleed air flow rate and keeping the engine leading edge

---

[1] the weight difference between of a SOV and a PRSOV is negligible for the nacelle overall weight

[2] this number is still a conservative approach

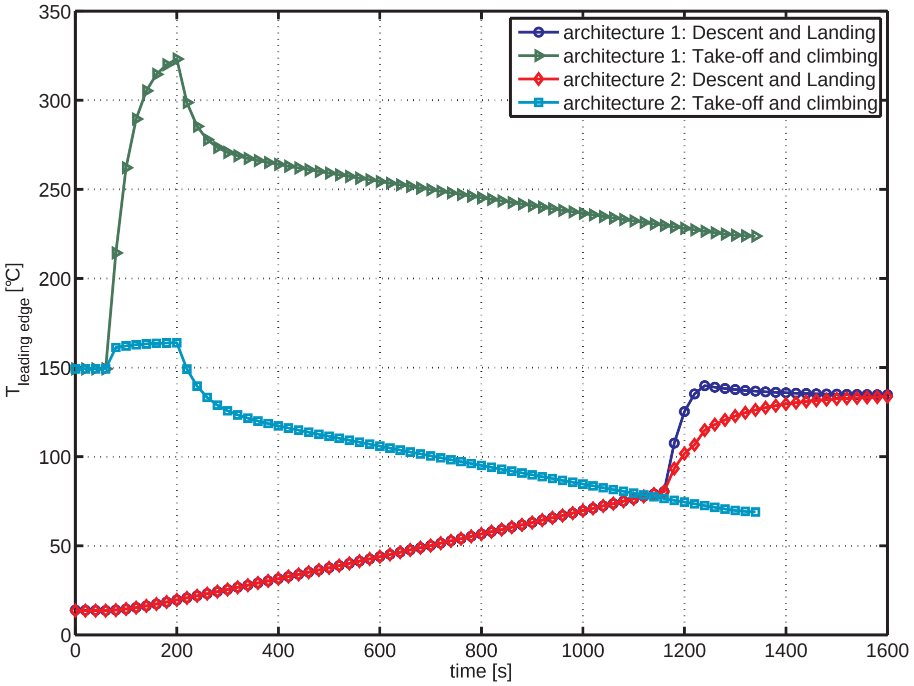

(a) Engine leading edge temperature

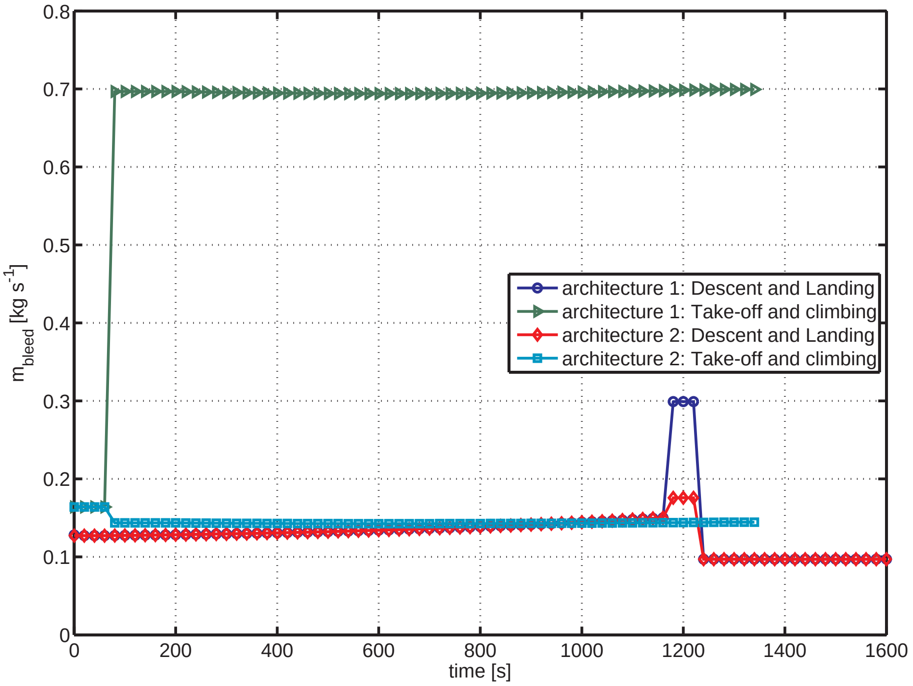

(b) Air flow rate bled from the engine

Figure 3.4: Performance comparison of anti-ice system architectures

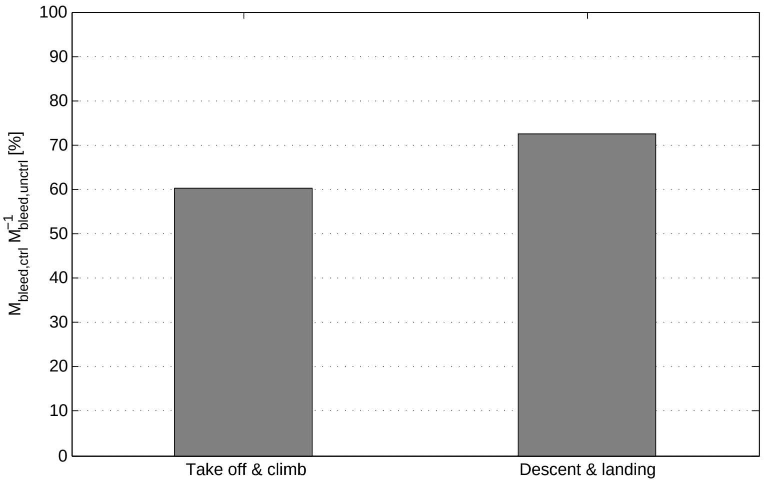

Figure 3.5: Fuel consumption reduction with green anti-ice system architecture

temperature within the desired band. On the opposite side, when the P_{bleed} and T_{bleed} are low the controls commands the FMSOV to open increasing as much as possible the pressure at the piccolo tube inlet, thus the bleed flow rate.

In the landing phase, when the airplane touches the ground, the anti-ice system is not more useful and can be switched off during the taxi when the OAT is higher than 0 °C.

To verify the above strategies a simple PID with clamping as anti windup method has been introduced into the model and the relief valve of the PRSOV has been replaced with a proportional solenoid.

The active control limits the m_{bleed} when the airplane is on ground reducing the bleed air flow rate (see figure 3.6(b)). The m_{bleed} increases during the climb phase to compensate the increase of heat flux to the external ambient due to OAT reduction.

The active control of the T_{LE} reduces the total mass of air bled from the engine in the take-off/climbing phase of about the 40 % (see figure 3.5).

In the descent phase the active control does not influence the anti-ice system behavior since they are driven by the very low value of P_{bleed} (minimum throttle conditions).

Below 2000 m the heat flux from the nacelle to the ambient is low enough that the T_{LE} reaches the target value ((see figure 3.6(a)). From this point the control acts to keep the T_{LE} to the desired value reducing the m_{bleed} (see figure 3.6(b)). When the airplane touches the runway the valves close stopping the bleed air flow extraction. The active control and the switch off strategy reduce the total mass of air bled from the engine in the descent/landing phase of about the 30 % (see figure 3.5).

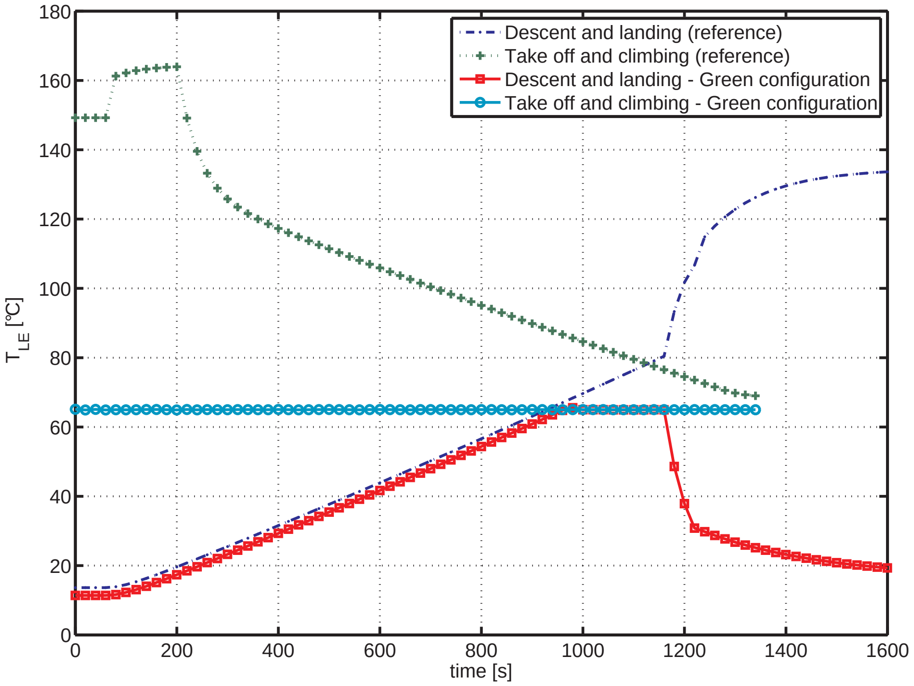

(a) T_{LE} during take off and descent phase

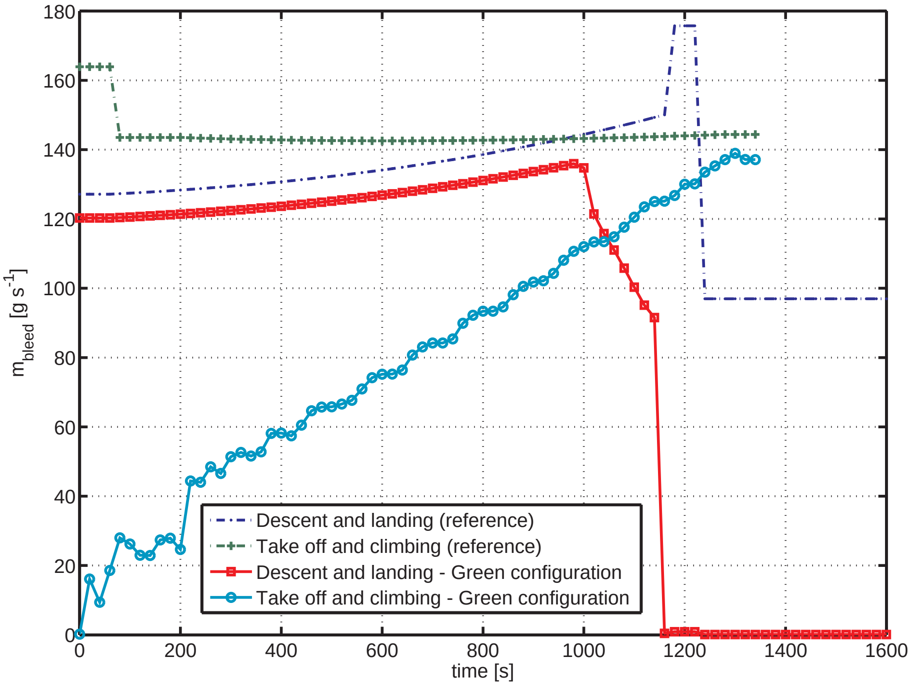

(b) m_{bleed} during take off and descent phase

Figure 3.6: Green anti-ice system architecture simulation results

Chapter 4

Thermal loads

SAE-AIR-1168/3 [2004] describes how to calculate the thermal load of an airplane; the method described is very useful to calculate the maximum heating load and the maximum cooling load, but it does not allow the simulation of the heat load variation during all flight envelope.

The approach herein proposed is based on a time-dependent simulation that allows the calculation of the aircraft external surface temperature T_{skin}.

4.1 Ambient model

4.1.1 Temperature and Pressure

There are several models of the atmosphere (i.e. ICAO [1993], MIL-STD-210-C [1987], MIL-HDBK-310 [1997]) they are based on several years of meteorological observation.

The model used in this document is based on International Standard Atmosphere (ISA) (ICAO [1993]), but is used simplified equations (4.1.1) and (4.1.2) and assumes that the air is a perfect gas ($\gamma = 1.4$ and $R = 287\,\mathrm{J\,kg^{-1}\,K^{-1}}$). All other thermodynamic parameters are calculated from the temperature and pressure.

$$OAT = \begin{cases} 288.15 - 0.0065\text{alt} + \Delta_{\text{ISA}} & \text{if alt} \leq 11000 \\ 216.65 + \Delta_{\text{ISA}} & \text{if alt} > 11000 \end{cases} \tag{4.1.1}$$

$$\text{OAP} = \text{OAP}_{\text{alt}=0}\left(1 - \frac{0.0065\text{alt}}{288.15 + \Delta_{\text{ISA}}}\right)^{5.26} \tag{4.1.2}$$

The model calculates the OAT nd OAP at the various altitudes using the above equations starting from the ground conditions, the user fixes.

4.1.2 Humidity

The air is a mixture of gases. Of all the gases the air is composed, the water vapor is the only one can change state condensing or evaporating in normal ambient conditions. The psychrometry is well explained is several books, herein only the formulas used to model the ambient humidity variation are detailed.

The amount of vapor water in the air is described by the relative humidity (φ) and the specific humidity (χ). The first one is the ratio of the partial water vapor pressure to the saturation pressure of the water vapor at the same conditions (temperature and pressure); the χ is the ratio of the water vapor mass over the mass of moist air.

$$\varphi = \frac{P_{\mathrm{H2O}}}{P_{\mathrm{sat}}} \tag{4.1.3a}$$

$$\chi = \frac{m_{\mathrm{H2O}}}{m_{\text{dry air}} + m_{\mathrm{H2O}}} \tag{4.1.3b}$$

The φ and the χ are linked together by equations 4.1.4.

$$\chi = \frac{0.622 \varphi P_{\mathrm{sat}}}{OAP - P_{\mathrm{sat}} \varphi} \tag{4.1.4a}$$

$$\varphi = \frac{\chi OAP}{P_{\mathrm{sat}}(0.622 + \chi)} \tag{4.1.4b}$$

The χ depends only on the quantity of vapor water inside the mixture; the φ depends on the quantity of vapor water and either on the temperature and on the pressure. The link of φ with the temperature is hidden inside P_{sat}. Several equations have been developed to calculate the P_{sat}; in the present model equation (4.1.5) is used. This equation comes from National Engineering Laboratory [1964] and, as demonstrate by Jones [1994], the results are in close agreement with ASHRAE [1997] data.

$$\begin{aligned}\log_{10}(P_{\mathrm{sat}}) = & 30.59051 - 8.2 \log_{10}(T + 273.16) + \\ & + 0.0024804(T + 273.16) - \frac{3142.31}{T + 273.16}\end{aligned} \tag{4.1.5}$$

The maximum quantity of water vapor can be contained in a mass of moist air is calculated assuming $\varphi = 1$, so then the vapor water partial pressure is equal to the saturation pressure: this condition is defined *saturation conditions*. If the temperature decreases, starting from a saturated conditions, the water vapor starts to condensate and the specific humidity of the air decreases.

The φ, coupled with the OAT and OAP, defines unambiguously the χ on ground. Increasing the altitude the temperature and pressure decrease, but the χ does not change since there are no sources of water vapor[1]; under these

---

[1] if present these sources affect already the ground φ

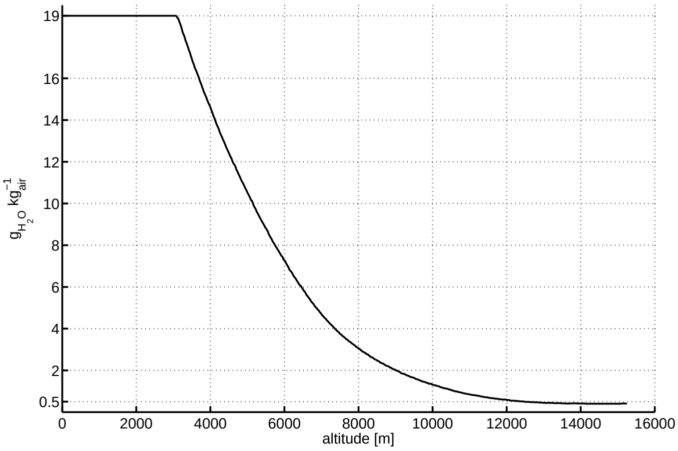

Figure 4.1: Variation of the specific humidity with respect to the altitude (from MIL-HDBK-310 [1997])

hypothesis the φ increases as per equation 4.1.4b. At a certain altitude (or better at certain temperature and pressure) the saturation conditions are reached ($\varphi = 1$); for higher altitude, the χ decreases (water vapor condensation) following the saturation curve.
Figure 4.1 shows the trend of χ reported in MIL-HDBK-310 [1997] which is generated following this approach.

4.1.3 Solar irradiance

Kopp and Lean [2011] determined a total solar irradiance upon earth of $1361\,\mathrm{W\,m^{-2}}$; this number is based on satellite observation and does not takes into account the reduction of the solar irradiance due to atmosphere absorption and scattering. Wendling et al. [2002] gives a curve to estimate the reduction of the solar irradiance at different altitudes.
Curve 4.2 has been obtained applying Wendling et al. [2002] results to the reduction curve of Kopp and Lean [2011] and it reppresent the trend of the solar irradiance per unit of area (G_s) with respect to the altitude.

4.2 Aircraft Heat loads

4.2.1 Solid external walls

The definition of *solid external walls* includes all the non-transparent surfaces of the aircraft fuselage. Figure 4.3 shows the cut-off view of the wall analyzed including the heat transfer phenomena take into account. All the heat flux passes through two thermal nodes; Each node schematize one of

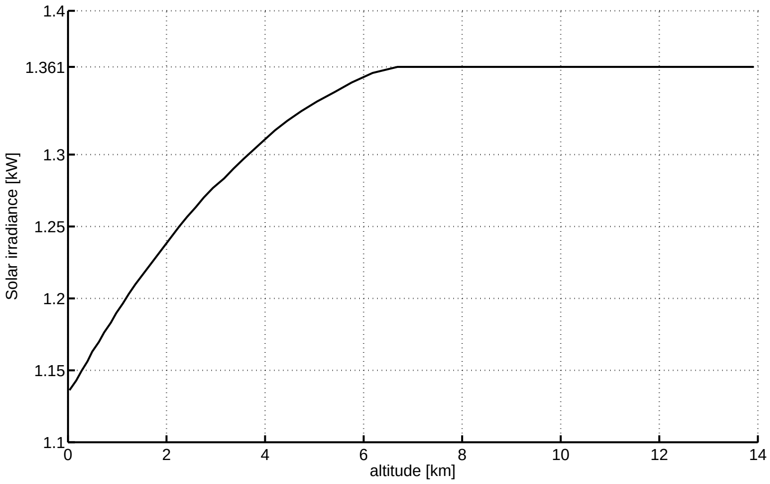

Figure 4.2: Solar irradiation at different altitudes

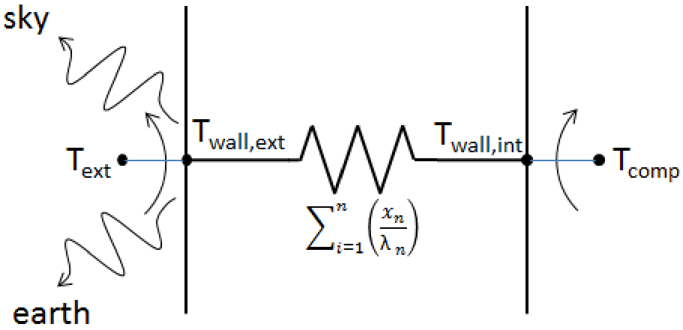

Figure 4.3: Solid wall thermal load schematic

the wall surfaces: one is the external skin surface and the other is the internal skin surface. The temperature of each wall is calculated solving equation (4.2.1) assigning an initial wall temperature.

$$\begin{cases} \frac{dT_{\text{wall,inn}}}{dt} = M_{\text{wall,inn}}^{-1} c_s^{-1} (q_{\text{inn}} - q_{\text{cond}}) \\ \frac{dT_{\text{wall,ext}}}{dt} = M_{\text{wall,ext}}^{-1} c_s^{-1} (q_{\text{ext}} + q_{\text{sky}} + q_{\text{earth}} + q_{\text{sun}} + q_{\text{cond}}) \end{cases} \tag{4.2.1}$$

On the external node there are 5 heat fluxes (q):

- convection with external ambient air (q_{ext})
- radiation with the sky (q_{sky})
- radiation with the earth (q_{earth})
- radiation from the sun (q_{sun})

- conduction with $T_{\text{wall,inn}}$ (q_{cond})

The convection with the external ambient is calculated using equation (4.2.2a) which is valid under the hypothesis detailed in section 4.2.2.
The one-dimensional Fourier's law of thermal conduction (equation (4.2.2e)) is used to calculate the heat transfer through the wall. This equation is used according to what reported in section 4.2.3.
The contribution to the sun radiance to the aircraft surfaces is calculated using equation (4.2.2d). The G_s is calculated according to section 4.1.3. For a cylinder (typical aircraft shape) the Projected area (A_p) is equal to $A_{\text{ext}}\pi^{-1}$.
The radiative heat exchange with the earth and the sky is calculated using equation (4.2.2c) and (4.2.2b), under the assumption detailed in 4.2.4.

$$q_{\text{ext}} = \hat{\alpha_{\text{ext}}} A_{\text{ext}}(T_r - T_{\text{wall,ext}}) \tag{4.2.2a}$$

$$q_{\text{sky}} = \sigma e_w F_{\text{a,1}} A_{\text{ext}}(T^4_{\text{skin,ext}} - 228.15^4) \tag{4.2.2b}$$

$$q_{\text{earth}} = \sigma e_w F_{\text{a,1}} A_{\text{ext}}(T^4_{\text{skin,ext}} - 283.15^4) \tag{4.2.2c}$$

$$q_{\text{sun}} = A_p G_s \tag{4.2.2d}$$

$$q_{\text{cond}} = \sum_i \left(\frac{\hat{k_i}}{x_i}\right) A(T_{\text{skin,ext}} - T_{\text{skin,inn}}) \tag{4.2.2e}$$

The inner node has only 2 heat fluxes since the inner radiative heat exchange is neglected because all the inner surfaces has almost the same temperature[2]:

- conduction with $T_{\text{wall,ext}}$ (q_{cond})
- convection with compartment air (q_{inn})

The conduction is the same described for the external node. The convection is calculated using equation (4.2.3) (see section 4.2.5 for details).

$$q_{\text{inn}} = \hat{\alpha_{\text{inn}}} A_{\text{inn}}(T_{\text{cpt}} - T_{\text{wall,inn}}) \tag{4.2.3}$$

4.2.2 External convective heat exchange

The air flowing on the external surface of an aircraft has a complex path. The airspeed varies locally on the airplane surfaces and depends from the aircraft attitude and speed. Aircraft equipped with propeller and the helicopter rotors contribute to make more complex the aerodynamic path along the fuselage (see Wadcock et al. [2008]). The aerodynamic of the aircraft influences two parameters: the external thermal-convection heat transfer coefficient ($\hat{\alpha_{\text{ext}}}$) and the aerodynamic heating coefficient. These two coefficients are considered a function of the aircraft speed only considering that

---

[2] the radiation from the occupants is included in the occupants heat load calculations

the external skin of the airplane compensates the locally hot and cold spot by conduction along all the external airplane surface.
Experimental and analytical studies show that the aircraft body is comparable to a flat plate, therefore the $\hat{\alpha_{\text{ext}}}$ is calculated using equation 3.1.3. At very low True Air Speed (TAS) (below $15\,\mathrm{m\,s^{-1}}$) SAE-AIR-1168/3 [2004] suggests to use equation (4.2.6) also for the $\hat{\alpha_{\text{ext}}}$.
The relative motion between the aircraft and the air creates a flow boundary layer; the frictional forces between the aircraft and the boundary layer convert the kinetic energy of the moving air into heat. The NASA performed a lot of work to create models that are able to predict this phenomena (i.e. Neumann and Freeman [2011]) in particular to evaluated the ablative shield of atmosphere re-entry vehicles; at speed below mach 1 this phenomena is present but it can be approximated, as suggested by SAE-AIR-1168/3 [2004], calculating the recovery temperature (T_r) with equation (4.2.4) and using it instead of the OAT.

$$T_r = OAT\left(1 + \sqrt[3]{Pr}\left(\frac{\gamma - 1}{2}\right)\mathrm{Ma}^2\right) \tag{4.2.4}$$

4.2.3 Aircraft wall

The fuselage of the aircraft is divided into: external skin, internal skin and structural features.
The internal skin, or liner, is the compartment surface. It is made by composite materials and it has no structural requirements expect the need to withstand the abuse loads of the passengers. For this reason it is usually very thick.
The aircraft loads are sustained by the longeron and the frames which divides the external skin from the internal skin. The semi-monocoque design creates a very complex system of thermal bridges and fins (see figure 4.4(a)); furthermore the space between the external and internal skin, not occupied by the structural frames, is full of electrical wiring, hydraulic ducts and thermal insulation blankets.
The external skin is the thin continuous layer external to the aircraft. It is generally made by different materials, depending on the area which covers.
The complex thermal path here above described is roughly approximated making the following simplifying hypothesis:

- no thermal bridge between adjacent surfaces
- The thermal conduction can change only along the wall thickness direction
- $\nabla T_{\text{cpt}} = 0$
- $\nabla T_r = 0$

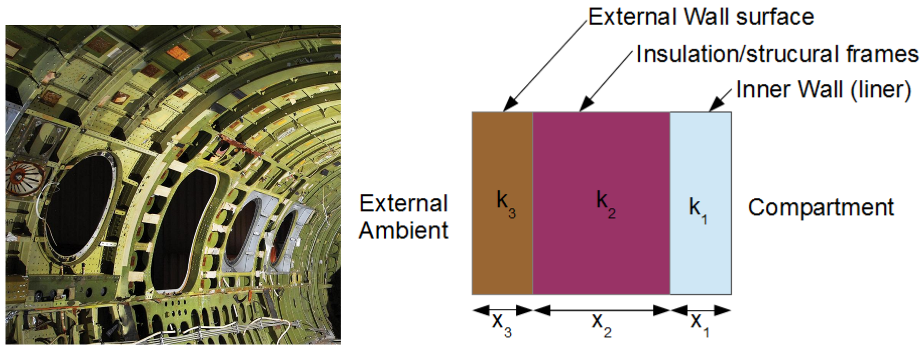

(a) Example of aircraft internal structure

(b) Typical aircraft wall section

Figure 4.4: Aircraft walls

As per the external air flow the error made introducing the above assumption is mitigated by the fact that the external and internal skin of the airplane compensates the locally hot and cold spot by conduction along all the external airplane surface.
The wall of the airplane is schematized as a one-dimensional wall made of various layers of different materials as figure 4.4(b) shows. The overall wall resistance is the sum of the resistance of each single layer as per equation (4.2.5).

$$R = \sum_i \frac{\hat{k}_i}{x_i} \tag{4.2.5}$$

The external wall is made by aluminium ($\hat{k}_t = 205\,\mathrm{W\,m^{-2}\,K^{-1}}$) or composite materials ($\hat{k}_t = 0.55\,\mathrm{W\,m^{-2}\,K^{-1}}$); the inner wall is generally made by plastic materials ($\hat{k}_t = 0.7\,\mathrm{W\,m^{-2}\,K^{-1}}$); the space between the two walls is very complex as previously described, it is convenient to take into account only the insulation layer (i.e. Microlite[3] $\hat{k}_t = 0.04\,\mathrm{W\,m^{-2}\,K^{-1}}$) which has generally a thickness between 25.4 mm to 50.8 mm[4].

4.2.4 Radiative heat exchange

The aircraft is not a black body, and also the surfaces surrounding it (runway, airport buildings, sea, etc.) are not black surfaces. The interaction between gray surfaces is very complex because the path of each ray emitted from each surface has be to be analyzed and the interaction between all the surrounding surfaces has to be considered. This work is done where the radiative heat exchange is the main heat transfer phenomena (i.e. very high temperature

---

[3] see http://www.jm-oem.com/files/pdf/Microlite_AA.pdf

[4] The thickness that has to be considered is the thickness of the material when installed and so compressed

difference between surfaces and/or negligible convection and conduction). These problems are solved using ray-tracing program like the one created by ESA and called ESATAN. The radiance from an aircraft, in particular for the infrared frequency, is a key design parameter for military aircrafts where the IR emission has to be minimized.
For the calculation of the thermal load of an aircraft some considerations simplify the problem. The aircraft interacts by radiation mainly with the sky and the earth. These surfaces creates a box that contains the aircraft: the aircraft has negligible dimensions and shapes with respect to the box surfaces. This geometrical consideration justify the introduction of the assumptions:

- the surface of the airplane is assimilable at a point having a temperature equal to the airplane average surface temperature
- the rays interacts only one time with the airplane surface before being absorbed by the box surfaces

The first assumption is in-line with what has been done for convection and conduction and it is also mitigated by the fact that the external and internal skin of the airplane compensate the locally hot and cold spot by conduction along all the external airplane surface.
A ray emitted directly from the aircraft surface, or a ray bounced against the aircraft surface has a very low probability to hit again the aircraft surface before its energy is absorbed by the other surfaces due to the small dimensions of the airplane surface compared with the surrounding surfaces, and this consideration justify the second hypothesis.
Under those hypothesis the radiative heat exchange between the aircraft and the external world is treated as the radiative heat exchange between a gray body (aircraft) and black bodies (earth and sky). The sky and earth temperatures to be considered are an average and they are:

- sky temperature 228.15 K
- earth temperature 283.15 K

The configuration factor (F_a) varies from surface to surface, depending on the orientation of the surface to the surrounding surfaces, the skin emissivity (e_w) is a function of the surface material and surface painting.

4.2.5 Inner convective heat exchange

The compartment is full of local heat sources (occupants, electronic, galleys, etc.) that creates a nonuniform distribution of the temperature inside the compartment. The air distribution system has to be designed to homogenize the temperature inside the compartment avoiding local temperature spots.

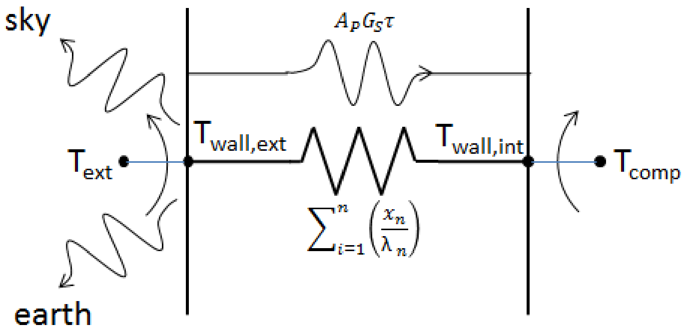

Figure 4.5: transparent thermal model schematic

The air is generally injected from the ceiling of the compartment and recovered from the floor. Under the assumption that the distribution system homogenizes the compartment temperature and airspeeds the compartment can be summarized in a single point having the average temperature of the compartment.

To avoid the discomfort of the occupants the airspeed cannot be very high, and generally is between $0\,\mathrm{m\,s^{-1}}$ to $1\,\mathrm{m\,s^{-1}}$. SAE-AIR-1168/3 [2004] suggests to use (4.2.6) to calculate the inner thermal-convection heat transfer coefficient ($\hat{\alpha_{\text{inn}}}$).

$$\hat{\alpha}_{\text{inn}} = 11.36 + 5.66\vec{v} \tag{4.2.6}$$

4.2.6 Transparencies

The transparencies are all the transparent area of the aircraft from the passengers side windows to the cockpit windshields.

The model of the transparencies is quite similar to the solid wall described in section 4.2.1, but in this case an additional heat flux has to be considered: the sun radiation pass directly through the windows to the compartment (see figure 4.5). The Overall solar transmissivity of transparent areas ($\hat{\tau}$) of the windows material determines the percentage of solar radiation entering directly into the compartment, while the e_w determines the percentage of solar radiation is absorbed by the material. The remaining energy is reflected and absorbed by the sky surrounding the airplane (see section 4.2.4 for the gray body assumptions). Therefore the additional heat flux (q_{solar}) is calculated using equation (4.2.7).

$$q_{\text{solar}} = \hat{\tau} A_p G_s \tag{4.2.7}$$

q_{solar} is an additional heat load and does not enters into the calculation of the transparencies wall temperatures.

4.2.7 The electrical equipments

The electrical equipments are one of the most important heat sources; there are a number of different type of electrical equipments installed on-board, starting from the ones used to passengers comfort and relax (i.e. cabin lights, monitors, film projection) arriving to the ones necessary for the flights (radios, cockpit multi-functional displays, radar). The electrical equipments are generally spread across all the airplane and uses the cabin cooling loop for their thermal control. In some cases, in particular when the heat load is high or their cooling is a flight critical function, they are segregated in an area of the airplane and a separate cooling loop is dedicated to the thermal control of this bay. In case of fly-by-wire commands, the cooling of the flight computers is a critical task for the airplane safety and the cooling loops are redundant.

The heat load of the electrical sources corresponds to the electrical power drained by these equipments. Please note that since the refrigerators on medium aircraft reject heat directly into the cabin, the heat load has to be considered into overall aircraft heat load calculation is the maximum one.

4.2.8 The passengers and the crews

The occupants of an ambient are another heat source. The human body converts the into mechanical (body movements) and electrical (brain signals) work the food we eat. Unlikely this conversion has a very poor efficiency and almost the energy is wasted in heat generation. The human body regulates its own temperature by exchanging heat with the surrounding air by convection, radiation and water evaporation. That means that the human body is a source of sensible and latent heat.

ASHRAE [1987] provides two graphs to estimate the heat load due to the crew and the passengers; the first graph (figure 4.6(a)) provides the sensible heat load and the second (figure 4.6(b)) provides the moisture loss at various compartment temperatures and at various metabolic rates.

4.2.9 Galleys

The galleys are the flying kitchens; they are essentially a framework incorporating storage space, a work surface, and various items of insert equipment for the storage and preparation of food for in-flight feeding. They are equipped with ovens, liquid containers, hot cups and refrigerators. Hot cups and ovens produce very-low term additional heat loads and they could be neglected in the aircraft overall heat load calculations; the refrigerators can generate a non-negligible heat load. The small aircrafts and helicopters use dry ice as heat sink for the refrigerators, in this case the refrigerators are not an additional heat load. Medium and large aircrafts use active cooling systems to preserve the food and cool down the beverages. On medium aircrafts

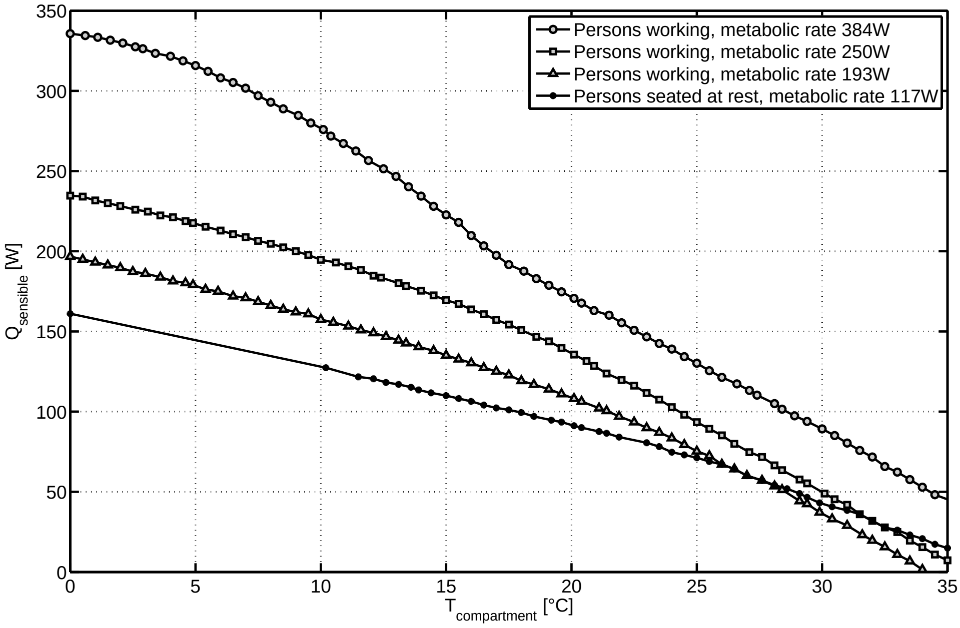

(a) Sensible heat loss by radiation and convection

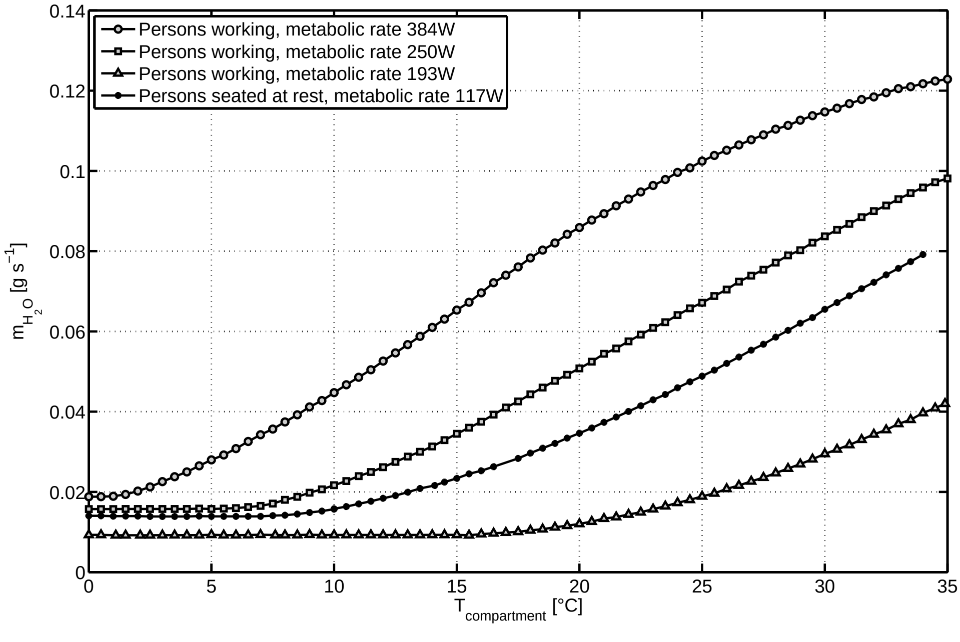

(b) Moisture loss from human body

Figure 4.6: ASHRAE guide curves for occupants (for average man 1.81 m^2)

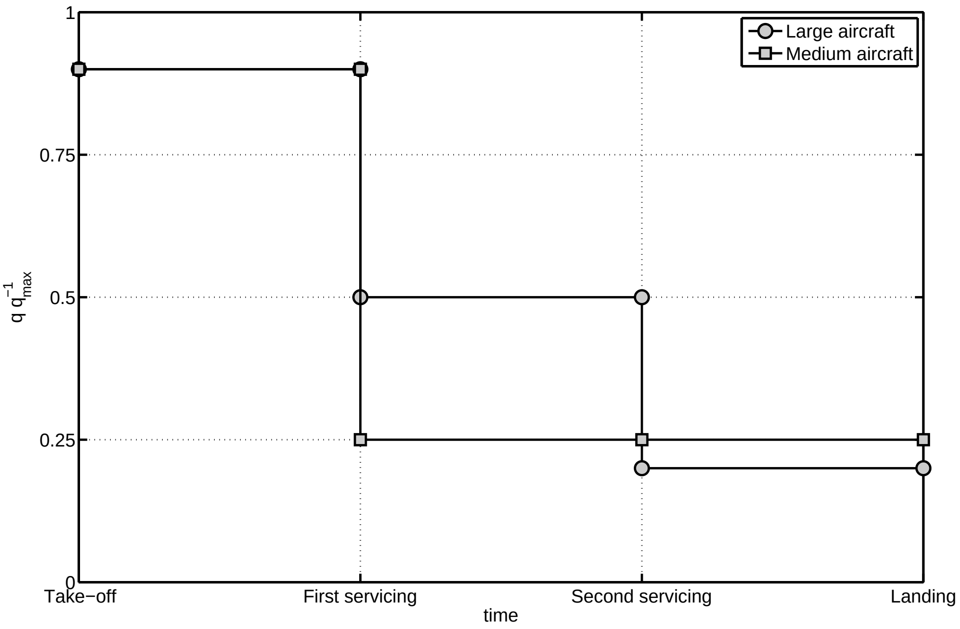

Figure 4.7: Refrigerators heat load typical profile

the galley cooling system is a vapor cycle system that reject heat into the cabin; this additional heat sources have to be taken into account in the overall heat load computation. On big aircrafts the refrigerator cooling system is centralized and the single refrigerators are cooled using a secondary fluid (like Thermera® or Galden®); the Centralized Refrigerator Unit (CRU) is a stand-alone unit that uses the external air to cool down the secondary fluid. Generally the CRUs are based on vapor cycle system.

Figure 4.7 shows the typical heat load for a CRUs during the flight (large aircraft curve). After the take-off the crew serve the first meal (lunch or dinner); most of the food is served at this time, so after the servicing a number of refrigerators are empty refrigerators and they are switched off decreasing the CRU heat load. The second servicing is generally a snack or a breakfast and also after this servicing other refrigerator are switched off. There are always some refrigerators continuously works to keep cool the beverages and the non-served meals.

On medium aircraft, since generally the mission time is shorter, there is only one servicing.

4.2.10 Adjacent compartments

Not all the aircraft is thermal controlled, and also some compartments are controlled at different temperatures.

The passengers compartment is generally divided in cabin (the area for the

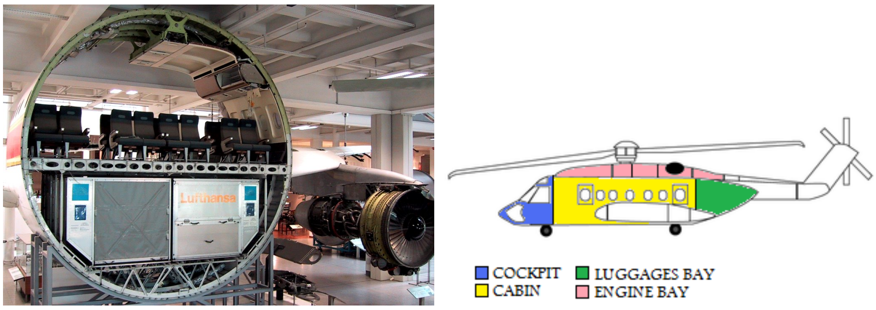

(a) A330 center fuselage frame section **(b)** Helicopter compartments

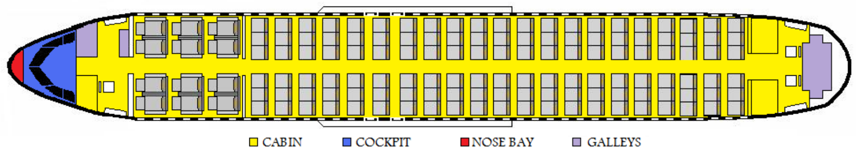

(c) A320 compartments

Figure 4.8: Location of aircraft compartments

Compartment	Temperature °C
Nose bay	70
Engine bay	110
Luggage compartment	70
Avionic bay	70

Table 4.1: Compartments typical temperatures

passengers) and cockpit (pilots zone). The two compartments are divided by a wall and the temperature of the two compartment can be set to different values.

The nose is generally used to install radar and other avionic equipments. The bay is not actively thermal controlled. On helicopter and small/medium aircraft the rear wall of the cabin divides the cabin by the luggage compartment. On big aircraft the floor of the cabin separates the passenger area from the cargo bay (see figure 4.8(a)). The ceiling of the helicopter cabin divides the cabin from the engine bay.

If there are no detailed information about the temperatures of these compartments, the value of table 4.1 can be used as first approximation. The value of table 4.1 is not a function of the OAT since it is assumed that the heat load of the equipment is sufficient to warm up the compartment.

The convection heat exchange coefficients are calculated using equation (4.2.6), considering an airspeed of $1\,\mathrm{m\,s^{-1}}$.

4.2.11 Ventilation requirement

The regulations impose a minimum fresh air flow for each occupant; this is to guarantee a good quality of the air inside the compartments. FAR 29.831[5] requires that in normal operation the fresh air flow should be at least $4.5\,\mathrm{g\,s^{-1}}$ for the passengers and $5.6\,\mathrm{g\,s^{-1}}$ for the crew.

The fresh air can be bled from the engines or directly drawn by external ambient using a fan. In the first case the heat load generated by the hot air entering into the compartment has a great impact on the overall aircraft heat load; in the second case also the heat load of the fan has to be considered (generally around 1.2 kW).

The fresh air flow rate contributes either on the sensible heat load and on the latent heat load since the air enters into the compartment having the same specific humidity of the outside ambient. The good practice indicates that the relative humidity inside the compartments should not exceed the 50 %.

The sensible heat load is estimated using equation (4.2.8a) and the latent heat using equation (4.2.8b).

$$\begin{aligned} q_{\mathrm{sens,vent}} &= \dot{m}_{\mathrm{vent}} c_p \left(T_{\mathrm{cpt}} - T_{\mathrm{in}}\right) \qquad (4.2.8a) \\ q_{\mathrm{lat,vent}} &= \dot{m}_{\mathrm{vent}} \left(2501e3 \left(\chi_{\mathrm{amb}} - \chi_{\mathrm{cpt}}\right) + \right. \\ &\quad \left. +1875 \left(T_{\mathrm{in}} \chi_{\mathrm{amb}} - T_{\mathrm{cpt}} \chi_{\mathrm{cpt}}\right)\right) \qquad (4.2.8b) \end{aligned}$$

The temperature in equation (4.2.8b) are expressed in °C.

4.2.12 Pressurization

The *OAP* decreases with the altitude and in particular the oxygen partial pressure decreases. Low partial pressure means low quantity of oxygen into the same volume of air, thus lower quantity of oxygen inhaled and exhaled by the human body. Generally all humans are able to withstand an air pressure corresponding to an altitude of 3000 m without experience any issue; over this altitude the body can start to fill a discomfort and the first symptoms of the hypoxia could be present due to the low oxygen contained into the air. The capability to withstand low pressure varies from people to people, as underlined by Muhm et al. [2007] and depends also from the climbing rate.

To flight above 3000 m the aircraft cabin and cockpit needs to be pressurized or the occupants has to use the oxygen masks.

---

[5] FAR 29 is applicable only to civilian helicopters, however similar requirements apply also to aircraft

The setting of the cabin pressure and the compartment pressure rate of change is selected by the crew when the airplane is on ground. Generally the value is set from 2000 m to 3000 m[6].
The cabin pressurization is obtained injecting pressurized air into the compartment and modulating the differential pressure between the compartments and the external ambient with dedicated valves (called outflow valves). These valves need a minimum flow rate to control the compartment pressure, however this value is usually lower than the ventilation requirement.
The injection of pressurized air creates a thermal load as described in section 4.2.11.

4.3 Tilt Rotor

All helicopter manufacturers are working to improves the maximum cruise speed of their vehicles. Each manufacturers is proposing different solutions, but only the tilt rotor is going to be certified in the next years. The tilt rotor (i.e. Bell V22 or AgustaWestland AW609) has the capability of vertical take-off and landing, but in cruise mode it is an aircraft. For thermal loads the tilt rotor is an interesting vehicle to be analyzed since it combines the characteristics of either the airplanes and the helicopters; in particular:

- it is a pressurized vehicle since it maximum cruise altitude is 25 000 ft
- up to 5000 ft the minimum speed is 0 kn (hovering)
- the maximum speed is 275 kn[7]

The model is based on AgustaWestland AW609. Dimensions and operative envelope are coming from commercial brochures[8]. The aircraft has been divided into four zones: AFT Avionic bay, CAB/CKP compartment[9], FWD avionic bay, baggage compartment. The main assumed characteristics of the compartments are shown in table 4.2. Only the CAB/CKP compartment is pressurized and the surface of the windows is assumed equal to the 8 % of the whole CAB surface. The skin of the aircraft is made by composite materials ($\hat{k_t} = 0.55\,\mathrm{W\,m^{-2}\,K^{-1}}$) with an average thickness of 1.5 mm; The cabin compartment is also insulated using thermal blankets having a thickness of 50.8 mm and a thermal conductivity ($\hat{k_t}$) of $0.04\,\mathrm{W\,m^{-2}\,K^{-1}}$. The emissivity and the absorptance of the external surface are 0.87 (black painted surface as reported in Henninger [1984]); the transmissivity of the transparencies is 0.79 (standard value for plexiglass). The aircraft is modeled as a cylinder

---

[6] lower altitude values create high stress on the airplane structure that requires bigger and heavier frames

[7] helicopter maximum speed is generally around 150 kn

[8] ref. to http://www.agustawestland.com/product/aw609

[9] from now called CAB

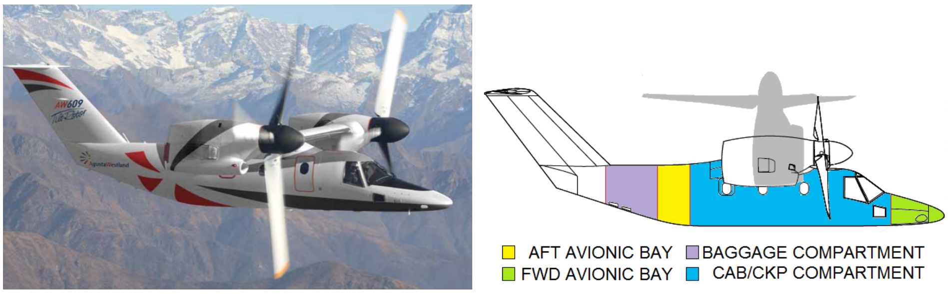

(a) AgustaWestland AW609 **(b)** general dimensions

Figure 4.9: AgustaWestland AW609 general characteristics

Compartment	A_{ext} m^2	Mass kg	Volume m^3
CAB	30	400	11
AFT avionic bay	5	250	3
FWD avionic bay	8	300	5
Baggage compartment	8	300	8

Table 4.2: Compartments main physical characteristics

so the projected surface is the total surface area divided by π, the shape factor for radiance to the sky and to the earth is 0.5. The bulkhead between the FWD avionic bay and the CAB has a surface of $1.5\,\text{m}^2$. The bulkheads between the CAB and the AFT avionic bay and the AFT avionic bay and the baggage compartment have the same area: $2\,\text{m}^2$. All the bulkheads are made by aluminium having a thickness of 2 mm with no thermal insulation applied. The fresh air is always provided through the bleed air line, and both the AFT and FWD avionic bay are cooled using the external air.

The FWD avionic bay has an electrical load of 2 kW, while the AFT avionic bay has an electrical load of 5 kW. The CAB electrical heat load is equal to the load of the FWD avionic bay.

4.3.1 Mathematical model

A Simulink® model has been created to calculate the thermal loads and the temperatures of the various aircraft compartments. The model is based on equations presented in section 4.2; a variable-order solver for stiff problems, based on the numerical differentiation formulas, has been used (ode15s).

The temperature of the bleed air entering into the compartment is assumed equal to 50 °C, and the flow rate is assumed equal to $0.042\,\text{m}^3\,\text{s}^{-1}$. The cooling flow rate of the avionic compartments is $0.15\,\text{m}^3\,\text{s}^{-1}$.

4.3.2 Results

The boundary conditions that creates the highest compartment thermal load are:

- $h = 0\,\mathrm{ft}$
- TAS $= 0\,\mathrm{kn}$
- maximum number of occupants
- full solar radiation
- maximum cabin temperature (commonly 27 °C)[10]
- highest applicable OAT (ΔISA $= 25\,^{\circ}\mathrm{C}$)

In these conditions (ΔISA $= 25\,^{\circ}\mathrm{C}$) the q_{cab} is 9 kW divided as shown in figure 4.10. The fresh air injected in to the cabin creates a total thermal load of 2.5 kW, and with the occupants (total heat load 1.8 kW) is the major source of heat; also the load due to electrical equipment is very high and a reallocation of some of the electrical components in the avionic bays should be right solution since the temperature of these two compartments do not reach very high values ($T_{\mathrm{AFT}} = 52\,^{\circ}\mathrm{C}$, $T_{\mathrm{FWD}} = 64\,^{\circ}\mathrm{C}$, $T_{\mathrm{BAG}} = 48\,^{\circ}\mathrm{C}$). The 50.8 mm insulation thickness reduce the thermal load through the walls (around 0.6 kW), but it does not influence the thermal load due to the solar radiation through the cabin windows which increases the thermal load of more than 1 kW. The reallocation of the electrical equipments (250 W into the FWD avionic bay and 500 W into the AFT avionic bay) bring a reduction of the cabin heat load of the 10 % without an appreciable increase of the compartment temperatures ($T_{\mathrm{AFT}} = 54\,^{\circ}\mathrm{C}$, $T_{\mathrm{FWD}} = 66\,^{\circ}\mathrm{C}$, $T_{\mathrm{BAG}} = 49\,^{\circ}\mathrm{C}$) and thus of the thermal load due to adjacent compartments: the location of the electrical equipment in dedicated bay is the best solution (where applicable) since these equipments can be easily cooled down with the external air or, if the loads are to high, with dedicated thermal control loops.

Pang et al. [2012] shows that an improved air distribution system had the potential to save energy by decreasing the amount of fresh air without significantly affecting air quality and thermal comfort. However this approach requires a lot of tests to demonstrate to authority the capability of air distribution layout to keep the air surrounding the occupants fresh and clean.

The boundary conditions that creates the lowest compartment thermal load are:

- maximum operating altitude (i.e. 25 kft)

---

[10] to maximize the thermal load the temperature should be the minimum one, but it is not technically a reasonable requirement

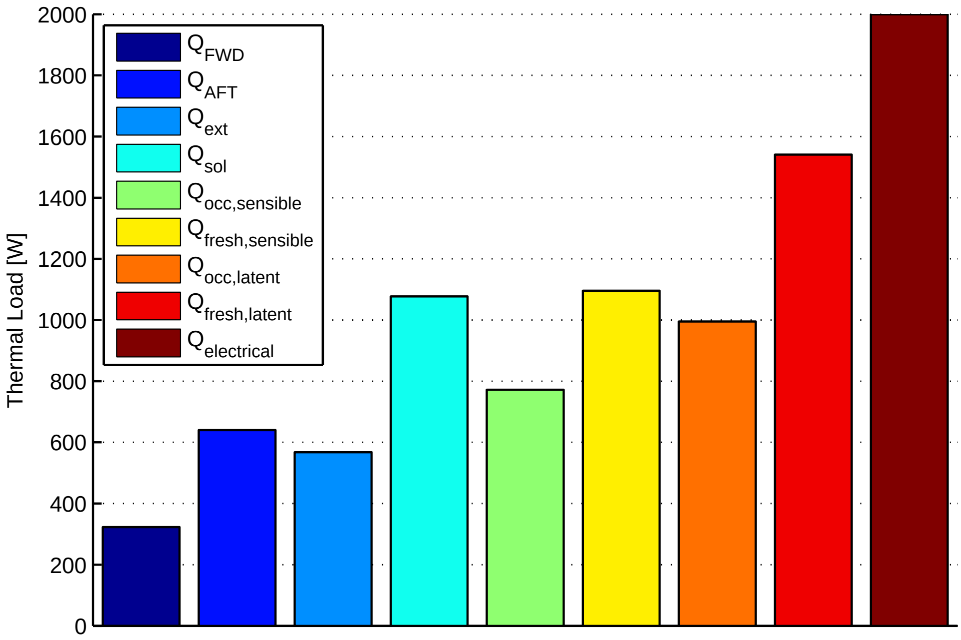

Figure 4.10: Tilt rotor hot day cabin thermal load. h=0 ft, ΔISA = 25 °C, $T_{\mathrm{CAB}} = 27\,°\mathrm{C}$

- maximum cruise speed (i.e. 275 kn)
- minimum number of occupants (only the crew to pilot the aircraft)
- night flight (no solar radiation)
- minimum cabin temperature (commonly 18 °C)[11]
- lowest applicable OAT ($\Delta\mathrm{ISA} = -35\,°\mathrm{C}$)

The lowest compartment thermal load is with the aircraft flying at the maximum altitude, with no passengers and the minimum number of crew members to pilot the aircraft at the lowest applicable OAT. In the above conditions the cabin thermal load is around -0.3 kW; the electrical and fresh air sources compensate the heat exchanged (q) exits from the cabin to the other compartments ($T_{\mathrm{AFT}} = -35\,°\mathrm{C}$, $T_{\mathrm{FWD}} = -27\,°\mathrm{C}$, $T_{\mathrm{BAG}} = -53\,°\mathrm{C}$) and to the ambient (see figure 4.11). A conservative approach is to consider that the fresh air is entering into the cabin at the same temperature of the compartment, in such way the fresh air contribution (1.7 kW) is deleted and the cabin heating thermal load reaches -2.0 kW.

All the boundary parameters listed above act in the thermal load equations in the same way, or to increase the heat load or to decrease the heat load;

---

[11] to minimize the thermal load the temperature should be the maximum one, but it is not technically a reasonable requirement

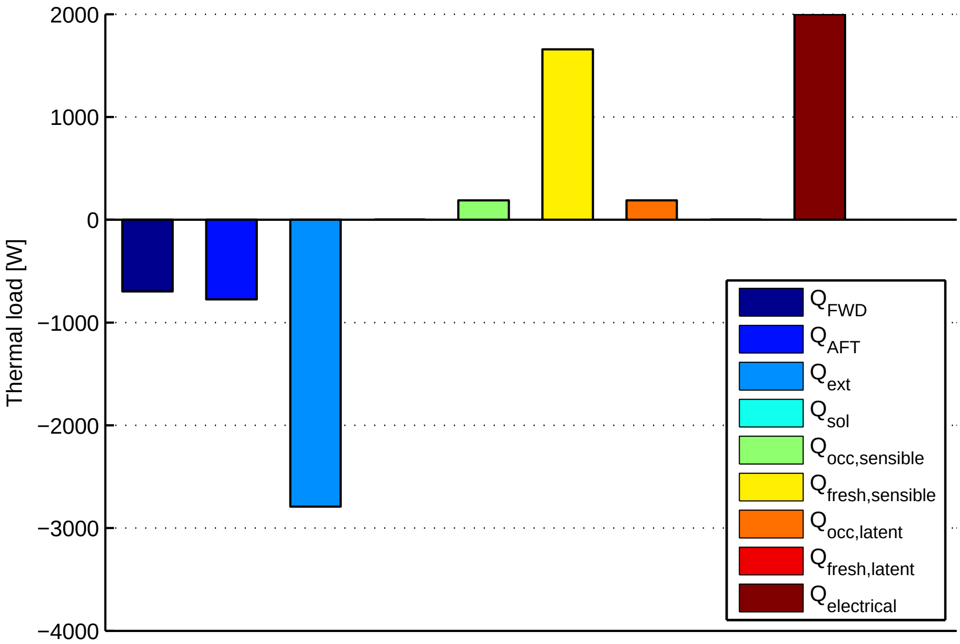

Figure 4.11: Tilt rotor cold day cabin thermal load. h=25 000 ft, $\Delta\text{ISA} = -30\,°\text{C}$, $T_{\text{CAB}} = 18\,°\text{C}$

the speed influences two parameters: the T_r and the external convective heat transfer coefficient ($\hat{\alpha_{\text{ext}}}$).

At low speed the $\hat{\alpha_{\text{ext}}}$ is low and so the heat transfer to the ambient is also low; increasing the speed the $\hat{\alpha_{\text{ext}}}$ increases as the q to the external ambient; also T_r increases, but until $T_r < T_{\text{wall,ext}}$ the contribution of $\hat{\alpha_{\text{ext}}}$ outnumbers the increase of T_r. At high speed the aerodynamic heating is high as also the $\hat{\alpha_{\text{ext}}}$; in these conditions the $T_r = T_{\text{wall,ext}}$, and so any increase of speed means a cabin thermal load increase (see equation (4.2.4) combined with equation (4.2.2a)). The minimum speed such that $T_r = T_{\text{wall,ext}}$ is the speed minimize the cabin thermal load. For the aircraft under analysis it happens for an aircraft speed of 80 kn (see figure 4.12). This speed is probably lower than the aircraft stall speed (around 110 kn), and so this is the speed to be considered in the calculations for the heating load. Figure 4.12 shows also that the cabin heat load increases with the increase of the speed (over a certain speed); this condition is not a continuous operating conditions for the aircraft but only a very short term conditions (i.e. for landing or take-off), for this reason is normal practice to consider the second maximum which correspond to the aircraft stopped on ground.

The cabin load does not go below 0 W even at high altitude in an extreme cold day during daylight time and with full passengers and crew loads (figure 4.13): The cooling system has to operate during all the mission. Figure 4.13 shows also how the cabin thermal load decreases very fast at high OATs.

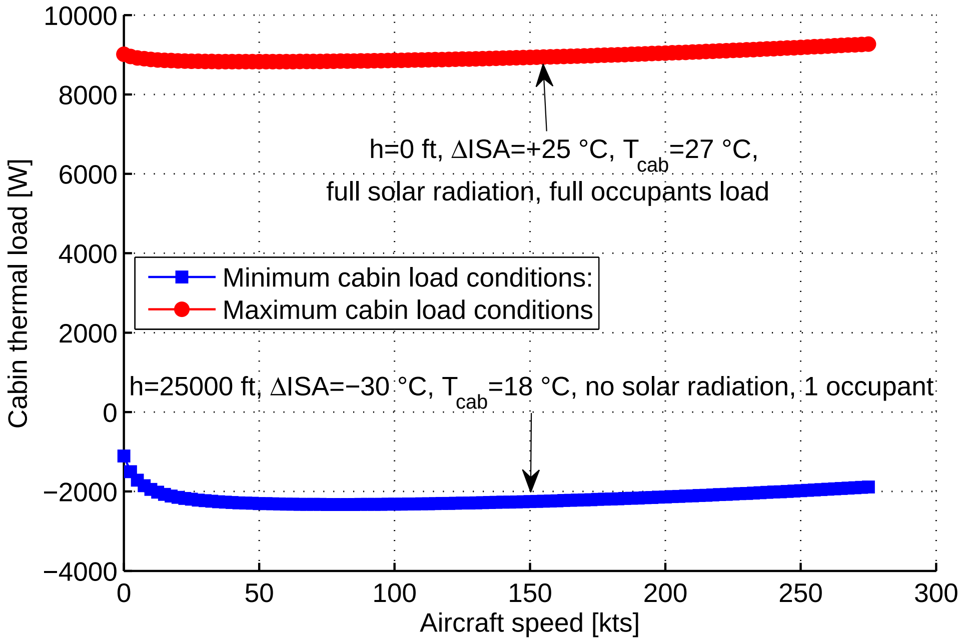

Figure 4.12: Effects of the speed on the cabin thermal load

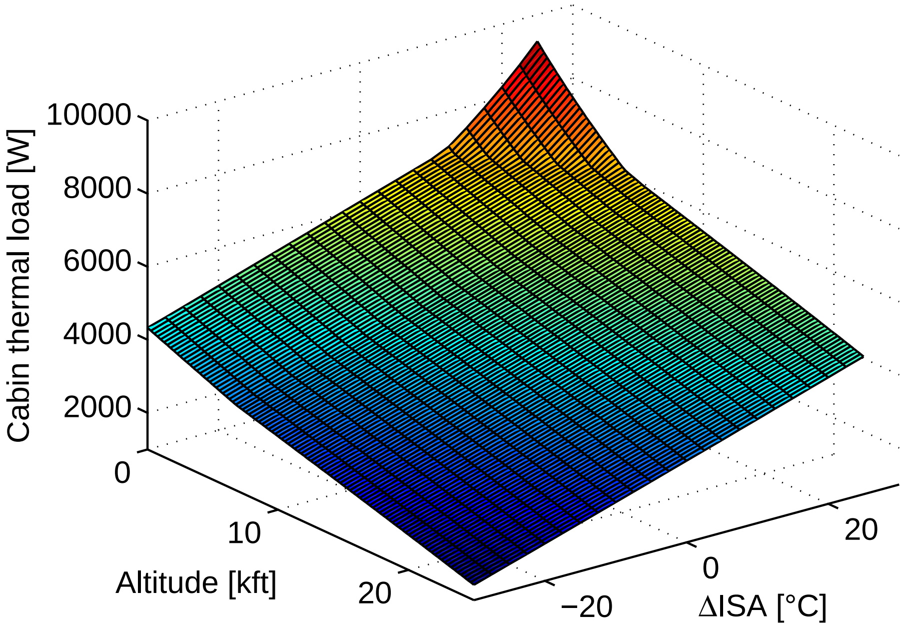

Figure 4.13: Cabin thermal load at different altitude and OATs

4.4 Aircraft temperature

In all previous paragraphs the compartment temperature is implicitly assumed as the average temperature of the compartment. This definition implies that the air distribution system is able to create an uniform air temperature into the compartment. The experimental studies performed by Kühn et al. [2009] and and Bianco et al. [2009], show that the flow field in aircraft cabin is very complex and affect by the internal layout of the aircraft, but also shows a good uniformity of the temperature inside the compartment. These results are also confirmed by Pang et al. [2012].
These articles support the assumption of the average compartment temperature for thermal load calculation but also support the experience on military aircraft, as stated in JSSG-2009 [1998], which underlines that this temperature is not a good parameter to establish cooling and heating requirements. In fact the thermal comfort of the occupants of a compartment, as studied by Fanger [1972], is influenced by several parameters:

- Air Temperature (Dry-Bulb)
- Relative Humidity
- Air Velocity
- Radiation (Mean Radiant Temperature)
- Metabolic Rate
- Clothing Insulation

The average temperature does not take into account all these parameters. Either JSSG-2009 [1998] and MIL-E-18927E [1983] suggest to use for large volumes the Wet Bulb Globe Temperature (WBGT) to determine cooling and heating requirements. The WBGT is determined using an 5 cm black globe sphere placed in the vicinity of the crew shoulders or heads; the temperature of the globe ($T_{\text{black globe}}$) is a function of the solar radiation, air velocity and compartment air temperature. The WBGT is calculated using equation (4.4.1).

$$\text{WBGT} = 0.7T_{\text{wet bulb, cpt}} + 0.2T_{\text{black globe}} + 0.1T_{\text{dry air, cpt}} \tag{4.4.1}$$

MIL-E-18927E [1983] indicates a range from 15 °C to 27 °C for continuous exposure (time greater than 1 h), as show in figure 4.14. These numbers are compatible with the ones reported in the MIL-STD-1472G [2012], which is the standard suggested as reference by JSSG-2009 [1998] for large aircraft.
WBGT takes into account all the aforementioned parameters, but has the drawback that is difficult to be understood and evaluated. Several authors proposed different equations to evaluate more easily the comfort conditions,

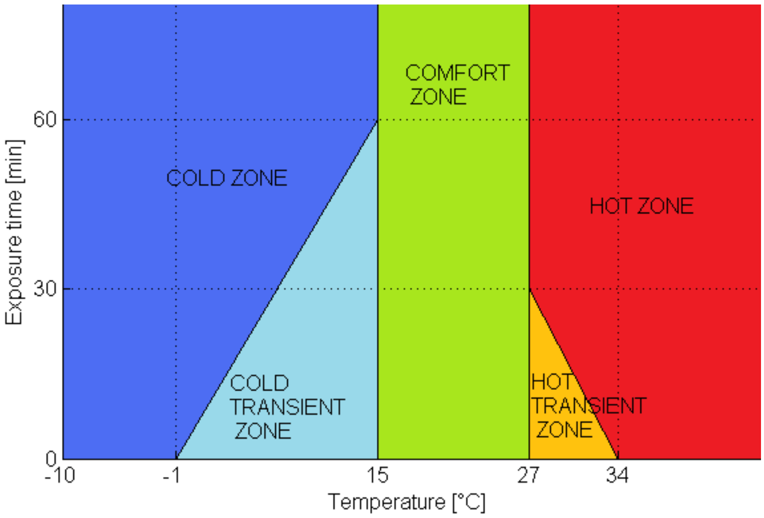

Figure 4.14: Compartment acceptable temperature values at different time exposure (as per MIL-E-18927E [1983])

and Epstein and Moran [2006] shows that there is a very good correlation between these equations and the WBGT; in particular for aircraft Nunneley and Stribley [1979] suggests equation (4.4.2) to approximate the WBGT.

$$\overline{\text{WBGT}} = 0.83T_{\text{wet bulb, cpt}} + 0.35T_{\text{dry air, cpt}} + 5.08 \tag{4.4.2}$$

JSSG-2009 [1998] suggests another formula for small volume which is based on experiences on military aircrafts. The Pilot Envelope Temperature (PET) is defined as the arithmetical average temperature measurements taken about the envelope occupied by the crew, for early design and analysis purposes equation (4.4.3) is suggested.

$$\text{PET} = 0.15T_{\text{air,in,cpt}} + 0.85T_{\text{air,out,cpt}} \tag{4.4.3}$$

the PET has the disadvantage that it does not consider the air humidity and the radiation effect, but it can be easily implemented also in the control loops just installing a temperature sensor at the inlet of the compartment (i.e. air vent inlets) at one at the outlet (i.e. near the cabin pressurization valves or the evaporator inlet). For large aircraft the coefficients could be revised to decrease the effect of the jet impingements on the human body.

Chapter 5

ECS: Air cycles

5.1 Introduction

The air cycles are widely used for airplane conditioning since they combine lightness, small envelope and simplicity; they also provide fresh pressurized air needful to maintain the comfort conditions for cabin occupants. On the other hand, the air cycle are not efficient wasting a lot of energy.
In the last years the cost of the fuel progressively increased, driving the airplane manufacturers to look for any possibility of fuel consumption reduction. The environmental control systems is one of the key energy users. Berlowitz [2010] shows that for a 40 MW engine, the power used for the pneumatic secondary power systems (ECS and anti-ice system) is around 1.2 MW, when all other secondary power systems (Electrical, hydraulic and mechanical systems) uses only 540 kW. Evans [1991] studied how the bleed air usage, influence the performances of an aircraft engine: he found that the specific fuel consumption increases approximately of 1 % for each percentage of bleed extraction.

5.2 Equipments mathematical model

Several equipments compose an air cycle: pneumatic valves, heat exchangers, Air Cycle Machines (ACMs), fans, etc. The mathematical model of some of these equipments has been already described and analyzed. In this section the mathematical model of the remaining equipments is briefly presented.

5.2.1 Electrical fan

The Environmental Control System (ECS) widely uses electrical fans to force the air flow. The electrical fan for aeronautic application are mainly divided

into direct current motor fan and alternative current motor fan. The type of fan depends only on the type of electrical supply available for the ECS. The fan manufacturers generally supply a map to summarize the performance of the item. The maps reports the pressure rise at various volumetric flow rates for a fixed density. Figure 5.1 shows a typical curve trend.
From the performance curve is possible to calculate the working point of the fan at different densities (thus different temperature), applying the affinity laws or Rateau's invariants (equations (5.2.1) report the invariant for a fan having the wheel radius fixed)[1].

$$\dot{V} = \dot{V}_{\text{ref}} \frac{\omega}{\omega_{\text{ref}}} \tag{5.2.1a}$$

$$\Delta P = \Delta P_{\text{ref}} \frac{\omega^2 \rho}{\omega_{\text{ref}}^2 \rho_{\text{ref}}} \tag{5.2.1b}$$

The electrical power consumption is calculated using equation (5.2.2) where the efficiency of the fan (η_{fan}) is in almost the cases around 0.5.

$$E = \frac{\dot{V} \Delta P}{\eta_{\text{fan}}} \tag{5.2.2}$$

The motor of the fan is cooled down by the same air it is moving, so the temperature at the fan outlet is higher than the inlet one. The temperature at fan outlet is calculated assuming that all the electrical power (E) is converted into thermal energy (equation (5.2.3)).

$$T_{\text{out,fan}} = T_{\text{in,fan}} + \frac{E}{\dot{m} c_p} \tag{5.2.3}$$

Generally the fan is a commercial component not developed ad hoc for the application. The selection is done overlapping the pressure drop of the line where the fan has to be installed, with the fan performance curve: the pressure drop curve has to cross the fan performance curve in the green zone (see 5.1).

5.2.2 Air Cycle Machine

The ACM is the core of a air cycle. The ACMs are divided into 3 main types:

- 2 wheels (the turbine drive a compressor or a fan)
- 3 wheels (the turbine drive a compressor and a fan)

---

[1] The use of the Rateau's invariant for ω very different from the ω_{ref} could leads to incorrect evaluation

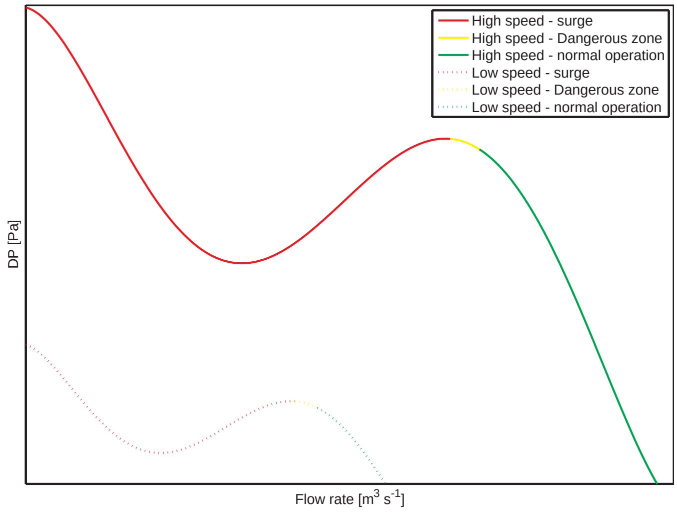

Figure 5.1: Fan typical performance map

- 4 wheels (the turbine is a 2 stages turbine, one stage drives a compressor, the other a fan)

The 2 wheels ACM is the simplest ACM, the first wheel is a turbine, the second wheel could be either a fan (i.e. for a simple cycle) or a compressor; in the last case it requires the use of an electrical fan to move the external air for the HXs.

The 3 wheels ACM solves the issue of the additional electrical fan, splicing a fan on the ACM shaft; in this way the power generated by the turbine is used to move either the compressor and the fan. The advantages are the reduction the weight and of the electrical budget of the system; the drawbacks are that the compressor and fan speeds have to be the same (maybe not the optimum for both, but a compromise), and it add some constrains in the system packaging.

The 4 wheels ACM split the expansion into 2 stage: an high pressure turbine which drives the compressor and a low pressure turbine which drives the fan. In this way the fan and the compressor are free to run at different speeds optimizing their performances.

Turbine

The air, which enters into the turbine, expands creating work and reducing its temperature. The expansion process is well approximated as an adiabatic process[2] the temperature at turbine outlet and the work available on the turbine shaft are calculated using respectively equation (5.2.4a) and 5.2.4b.

---

[2] The approximation is particulary true since the air flows very quickly into the machine having no the time to exchange heat with the machine surfaces

$$T_{2,\text{iso}} = T_1 \left(\frac{P_2}{P_1}\right)^{\frac{\gamma-1}{\gamma}} \tag{5.2.4a}$$

$$W_{\text{iso}} = \dot{m} c_p T_1 \left(1 - \left(\frac{P_2}{P_1}\right)^{\frac{\gamma-1}{\gamma}}\right) \tag{5.2.4b}$$

The expansion process, even if well approximated by an isentropic process, has some irreversibility; the isentropic efficiency (defined for an expansion process by equation (5.2.5)) correlates the isoentropic expansion with the real expansion.

$$\eta_{\text{iso,ex}} = \frac{W_{\text{iso}}}{W_{\text{real}}} = \frac{T_1 - T_{2,\text{iso}}}{T_1 - T_2} \tag{5.2.5}$$

The equations for the real expansion, (5.2.6), are obtained introducing equation (5.2.5) into equations (5.2.4).

$$T_2 = T_1 + \eta_{\text{iso,ex}} T_1 \left(\left(\frac{P_2}{P_1}\right)^{\frac{\gamma-1}{\gamma}} - 1\right) \tag{5.2.6a}$$

$$W_{\text{ex}} = \eta_{\text{iso,ex}} \dot{m} c_p T_1 \left(1 - \left(\frac{P_2}{P_1}\right)^{\frac{\gamma-1}{\gamma}}\right) \tag{5.2.6b}$$

The efficiency of the turbine is generally reported on a map as a function of the corrected flow rate ($\dot{m}_{\text{corr}}$) and of the turbine corrected speed (ω_{corr}). Figure 5.2(b) shows a typical turbine efficiency map. There is a second map used to summarizes the performance of the turbine: it reports $\dot{m}_{\text{corr}}$ as a function of the turbine pressure ratio and ω_{corr} (see figure 5.2(a)).

$$\dot{m}_{\text{corr}} = \frac{\dot{m}\sqrt{T_1}}{P_1} \tag{5.2.7a}$$

$$\omega_{\text{corr}} = \omega \left(\frac{T_1}{288.15}\right)^{-\frac{1}{2}} \tag{5.2.7b}$$

The results of equation (5.2.6a) is the temperature reachable at the turbine outlet in case that the humidity of the air does not condensate during the expansion process: it is called dry air temperature (T_{dry}), and it is the minimum achievable temperature at the turbine outlet at those boundary conditions.

In case that the air moisture condensates in the expansion process, part of the work is used for the state change, and so the turbine outlet temperature in wet conditions (T_{wet}) is higher than T_{dry}. The wet conditions are calculated assuming that the φ at the turbine outlet is 100 %. T_{wet} is computed

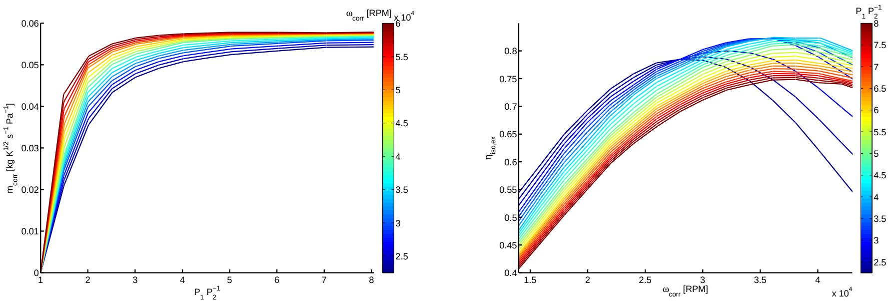

(a) flow coefficient map **(b)** efficiency map

Figure 5.2: Turbine maps

Figure 5.3: Icing condition at turbine outlet

solving the implicit equation (5.2.8)[3].

$$\frac{W_{\text{ex}}}{m_{\text{air}}} = c_{p\text{dry,air}}(T_1 - T_{\text{wet}}) + c_L(\chi_1 - \frac{0.622 P_{\text{sat}}}{P - P_{\text{sat}}}) + \\ + c_{pH_2O,\text{vap}}(T_1\chi_1 - T_{\text{wet}}\frac{0.622 P_{\text{sat}}}{P - P_{\text{sat}}}) \qquad (5.2.8)$$

If T_{wet} is greater than T_{dry}, the temperature at the turbine outlet is equal to T_{dry}, otherwise the temperature at the turbine outlet is equal to T_{wet}, and equation (5.2.9) estimates the free water at the turbine outlet.

$$m_{H_2O,\text{free}} = m_{\text{air}}(\chi_1 - \chi_{\text{wet}}) \qquad (5.2.9)$$

The condensation inside the turbine damages the turbine itself. The free water impingement against the airfoils abrades the blade surfaces reducing the efficiency of the turbine; the effects are more serious if the temperature goes below 0 °C and the water becomes ice. The ice darts can also damage the equipment installed downstream the turbine (i.e. heat exchanger).
The presence of free water at the system outlet (i.e. passengers jets) has to be avoided using nets or devices to stop the carryover water.
Some system configurations avoid this dangerous conditions.

---

[3] According to equation (4.1.5), P_{sat} is a function only of T_{wet}

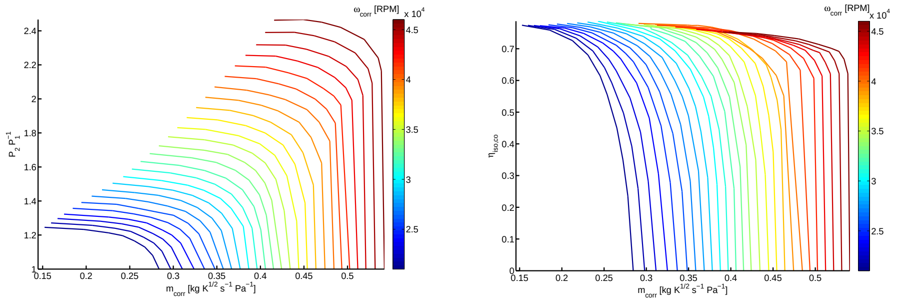

(a) Pressure ratio map **(b)** efficiency map

Figure 5.4: Compressor maps

Compressor

The compressor transforms the mechanical work available into pneumatic work by increasing the pressure of the air. Unfortunately the pressure increase is coupled also with a temperature increase. The equations describes the ideal evolution of the fluid between the inlet and the outlet port of the compressor are the same used for the turbine (see (5.2.4); The isentropic efficiency is calculated using equation (5.2.10), thus the equations to calculate the real evolution of the fluid into the compressor are equations (5.2.11).

$$\eta_{\text{iso,co}} = \frac{T_{2,\text{iso}} - T_1}{T_2 - T_1} \tag{5.2.10}$$

$$T_2 = T_1 + \frac{T_1}{\eta_{\text{iso,co}}} \left(\left(\frac{P_2}{P_1} \right)^{\frac{\gamma-1}{\gamma}} - 1 \right) \tag{5.2.11a}$$

$$W_{\text{co}} = \frac{\dot{m} c_p T_1}{\eta_{\text{iso,co}}} \left(1 - \left(\frac{P_2}{P_1} \right)^{\frac{\gamma-1}{\gamma}} \right) \tag{5.2.11b}$$

The performance of the compressors are summarized into two maps: one map reports the $\eta_{\text{iso,co}}$ the other reports the pressure ratio as a function of the $\dot{m}_{\text{corr}}$ and of the ω_{corr} (see figure 5.4).

ACM shaft

The speed at which the ACM rotates is calculated applying the second law of Newton to the shaft connecting the two machines.

$$J\frac{d\omega}{dt} + c\omega = \tau_{\text{tu}} - \tau_{\text{co}} \tag{5.2.12}$$

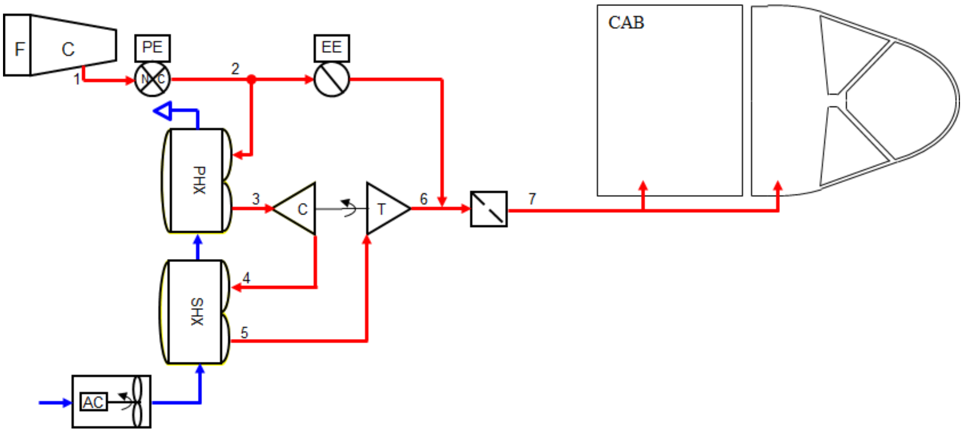

Figure 5.5: Air cycle - Bootstrap system schematic

Where moment of inertia (J) takes is the sum of all the rotary inertia of the ACM, so it includes also the inertia of the turbine disk and of the compressor disk.

5.3 Bootstrap cycle

Figure 5.5 shows the schematic of a bootstrap cycle. The air bled by the engines passes through a PRSOV (1-2); the valve limits the maximum downstream pressure allowing a reduction of the thickness of the downstream item external walls and also it limits the speed of the ACM.

Downstream the valve there is the first HX: the Primary Heat Exchanger (PHX). This HX is generally made of stainless steel (due to high temperature of the bleed air). The PHX reduces the bleed air temperature (2-3) exchanging heat with the external air.

The air cooled into the PHX arrives to the ACM compressor, where the mechanical work of the turbine is converted into pressure (3-4). This compression is useful especially in idle conditions when the turbine pressure ratio is low (since the bleed pressure is low) and the heat load is high (i.e. parking conditions).

A Secondary Heat Exchanger (SHX), installed downstream the compressor, further decreases the bleed air temperature (4-5). The more compact solution for the system is to use the same fan either for the PHX and the SHX; in this configuration the fan is installed upstream the two HXs since the discharge temperature is too high for standard fans, the first HX seeing the external air is the SHX and the second is the PHX. In this way the logarithmic temperature across the 2 HXs is maximized for both the items, optimizing the performance of the system.

The bleed air exiting the SHX expands into the turbine creating work on

the ACM shaft and reducing the bleed air temperature (5-6).
The turbine cold air is mixed with the hot air of the bypass line (6-7); the control loop commands a butterfly valve to keep the temperature entering into the compartments inside the range allowed by the international regulations (i.e. FAR, [FAA, 2012]). This range is generally from 2 °C to 71 °C.
The air humidity could condensate during the expansion process; in this case there is some free water at the turbine outlet. A water separator is installed downstream the turbine (6-7) to remove the water and prevent that the droplet arrives into the compartments.

5.3.1 Mathematical model

A 0d model has been created to analyze the behavior of a bootstrap cycle and to identify possible improvements.
The model used assumes that the pressure at the bleed port, at which the ECS is connected, varies linearly with the Ξ command (see equation (5.3.1a)) and it reaches a maximum bleed pressure of 1700 kPa[4]. The temperature is calculated assuming an isentropic compression (see equation (5.3.1b)).

$$P_{\text{bleed}} = \frac{\Xi}{100}(\beta_{\text{bleed,max}} P_{\text{amb}}) \tag{5.3.1a}$$

$$T_{\text{bleed}} = OAT \left(\frac{P_{\text{bleed}}}{P_{\text{amb}}}\right)^{\frac{\gamma-1}{\gamma}} \tag{5.3.1b}$$

The characteristics of the HXs are detailed in table 5.1. The efficiency of the turbine has been set to 0.8 and the compressor efficiency has been set to 0.7. The fan used is an aerospace commercial item.
The by-pass valve is controlled by a P.I.D. to maintain a minimum cabin inlet temperature ($T_{\text{in,cab}}$) of 2 °C.

5.3.2 Mathematical model results

The efficiency of the cycle (η_{bs}) is defined as the ratio between the maximum heat load removable by the system and the energy spent to compress the air into the engine (see equation (5.3.2))[5]. The air flow rate enters into the cabin ($m_{\text{in,cab}}$) is lower than the air bled from the engine (m_{bleed}), because part of the air is used to cool down the ACM bearings and part of the air is used to push out the the free water at the turbine outlet.

$$\eta_{\text{bs}} = \frac{\dot{m}_{\text{in,cab}}(T_{\text{in,cab}} - OAT)}{\dot{m}_{\text{bleed}}(T_{\text{bleed}} - OAT)} \tag{5.3.2}$$

---

[4] typical number for small airplane or helicopter engines

[5] this formulation neglects the electrical power consumption of the fans

Parameter	Unit	PHX	SHX
LNF	mm	250.0	250.0
LH	mm	203.0	203.0
LC	mm	150.0	150.0
Fin Type		Wavy	Wavy
fh_{hot}	mm	5	5
fpi_{hot}	in^{-1}	28	28
ft_{hot}	mm	0.1	0.1
fh_{cold}	mm	15	15
fpi_{cold}	in^{-1}	20	20
ft_{cold}	mm	0.1	0.1
$Npass$		2	2
ppt	mm	0.4	0.4
Material		Al	AISI347
Fluid Cold side		air	air
Fluid Hot side		air	air

Table 5.1: Geometrical characteristics of the HXs installed in the bootstrap system

The cooling capacity is calculated applying first principle of thermodynamic to the compartment (control volume). A compartment temperature of 25 °C and a compartment pressure of 101.325 kPa have been considered for the calculation.

Figure 5.6(a) shows the thermodynamic diagram $\log P - h$ of the bootstrap system in a standard hot hay (OAT=40 °C and φ=50 %)) at various Ξ. At high throttle the pressure at bleed port is reduced by the PRSOV; this transformation is adiabatic, therefore the energy (pressure) can be spent into the turbine to cool the air is reduced, but the energy that cannot be converted (temperature) is still at high level: this means a great reduction of the efficiency of the cycle (see figure 5.6(b)). The performance of the two heat exchangers changes with respect to the bleed air temperature: higher bleed temperature means higher logarithmic mean temperature, and so more energy exchange when the LMTD is high. This behavior partially compensates the energy wasted in the PRSOV, in fact the turbine inlet conditions are quite constant.

The expansion in the turbine, in presence of humidity, is the second contributor to the poor efficiency of the cycle. Part of the energy created by the expansion in the turbine is used to condensate the water vapor entrained into the air, and so the efficiency of the transformation is dramatically reduced (check on figure 5.6(a) the turbine outlet conditions why dry air and with wet air). The increase of temperature into the distribution ducts promotes

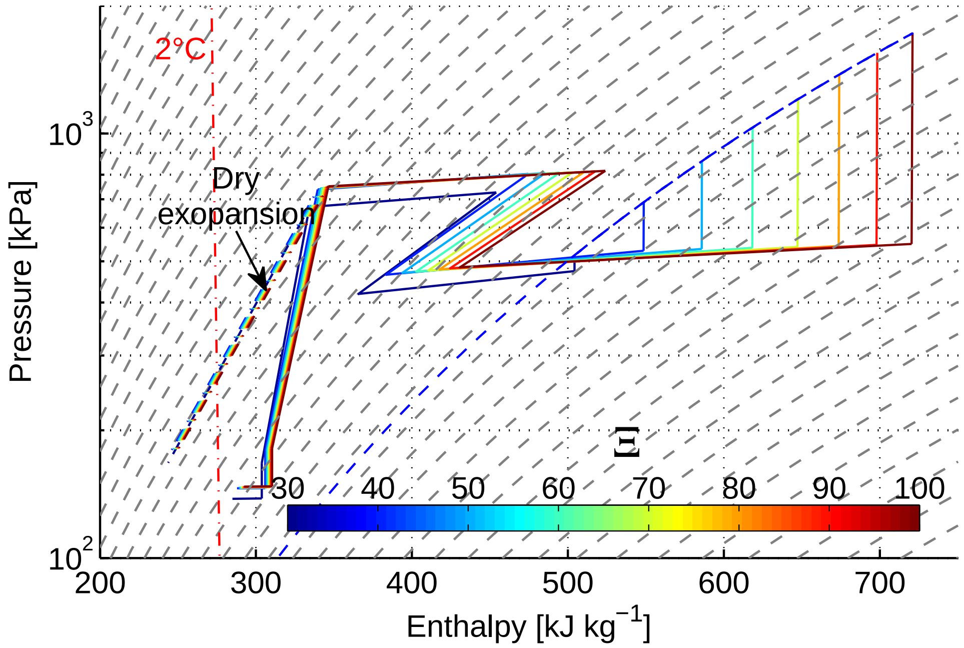

(a) thermodynamic diagram log P-h

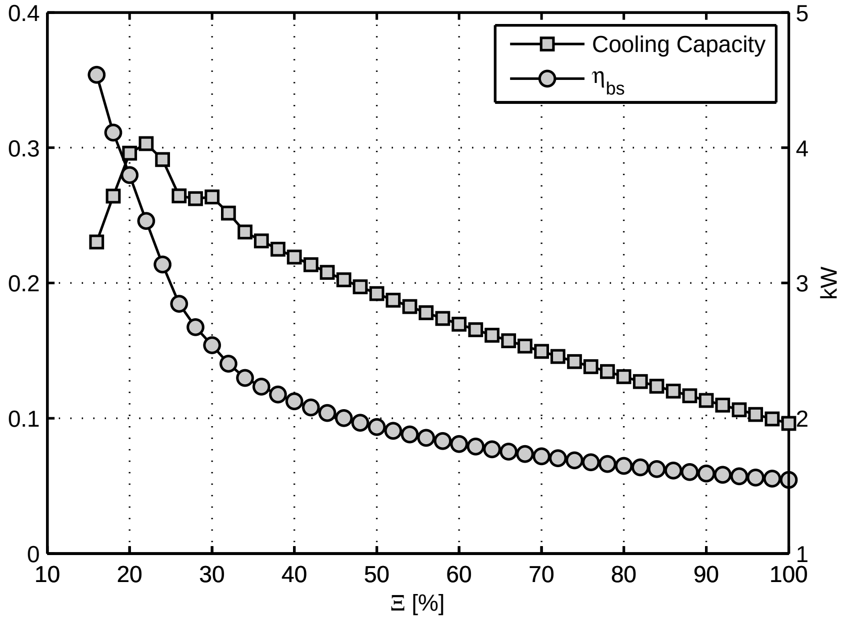

(b) cooling capacity and η_{bs}

Figure 5.6: Bootstrap cycle simulation results at various Ξ, on ground and with OAT=40 °C, φ=50 %

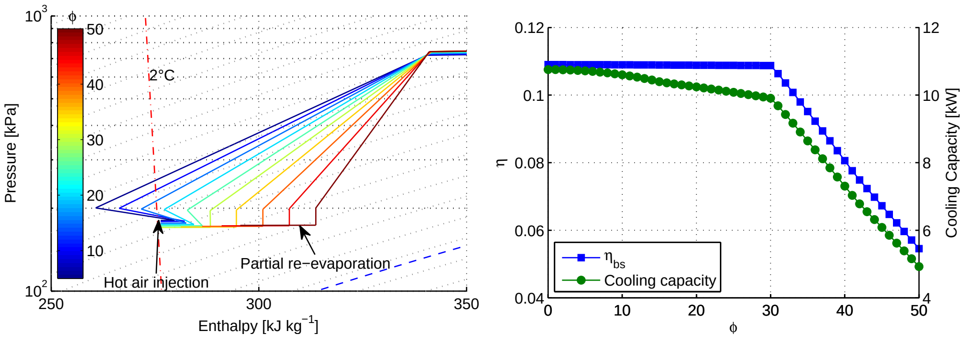

(a) Turbine expansion **(b)** η_{bs}

Figure 5.7: humidity influence on a bootstrap cycle.
On ground, Δ_{ISA}=25 °C, Ξ=75 %

the evaporation of the free water, which has not been not removed by the water separator installed downstream the turbine. The evaporation process allows a partial recover of the energy wasted to condensate the water. There are a lot of factors influence the re-evaporation of the free water (i.e. air-speed, the routing of the distribution ducts, compartment temperature) and in particular when no hot air is injected after the turbine and the ambient relative humidity is very high (i.e. South-east countries conditions) not all the free water evaporates before entering into the compartments, and some water is sprayed directly inside the compartments.

Figure 5.7 shows the turbine expansion and the efficiency of the system change with respect to the air humidity;

The optimum working point is when the engine pressure is equal to the PRSOV regulation point[6]; in this case the PRSOV is full open and the pressure drops are minimized, the removable heat load reaches the maximum and the efficiency is a little less of the 15 %; the predicted value of efficiency is in according also with [Moir and Seabridge, 2008] that identify an average efficiency of the 10 % for air cycles. After the optimum point the cooling capacity of the system drops since the reduction of the turbine pressure ratio penalizes the performance more heavier than the gain of system overall efficiency.

The optimum point of the loop can be moved and the cooling capacity of the system can be increased simply modifying the PRSOV setting point: if the regulated pressure increases, the cooling capacity increases, otherwise it decreases. The thermodynamic designer is not free of set whatever pressure downstream the valve, but he has to take into account mainly 2 facts:

- Compressor outlet pressure

---

[6] in the case under analysis this happens when Ξ is around the 23 %

- Proof and burst pressure requirements
- Engine bleed flow rate limitation

The PRSOV pressure increase means an increase of the bleed air flow rate that can exceed the maximum allowed; the increase of the flow rate has also the effect of increase the temperature at the compressor inlet[7] and therefore the temperature at the compressor outlet can achieve the technologic limits for aluminum use (around 250 °C) means a weight increase due to the use of stainless steel. The international regulations ([FAA, 2012]) ask that all the components have to withstand without permanent deformation or damages a pressure which is 1.5 times the maximum operative one (proof pressure test) and have to withstand without burst a pressure which is 3 times the maximum operative one (burst pressure test). The increase of PRSOV pressure regulation shifts to higher maximum operative ressure all the components of the system. This means that the wall thicknesses of the ducts, of the heat exchangers and of the air cycle machine have to be increased increasing obviously the weight of the system reducing either the payload or the range of the aircraft.

The simulations performed at various OAT fixing the Ξ (50 %) show the effects of the hot air injection (see figure 5.8(a)). For OAT lower than 36 °C the turbine outlet wet temperature is lower than 2 °C, and so the by-pass valve opens to keep the temperature of the air entering into the compartment around the minimum allowed value. The opening of the by-pass valve increases the flow rate of the air bled from the engine increasing the cooling capacity of the system. On the other hand the efficiency of the cycle drops since the system can obtain the same cooling capacity at lower bleed flow rate (but the cabin inlet minimum temperature requirement is not meet). Figure 5.8(b) shows clearly this behavior: around $OAT = 36\,^{\circ}\mathrm{C}$ there is a change is the slope of the cooling capacity curve and the maximum point for the efficiency of the system.

5.4 Optimized bootstrap cycles

5.4.1 Improved parzialization method

The by-pass valve is used also to modulate the cooling capacity of the system: if the compartment temperature is below the required value, the valve opens increasing the temperature at cabin inlet, and so decreasing the cooling capacity of the system. Figure 5.10(b) shows this behavior. At low cabin thermal loads the by-pass valve is open and the temperature entering into

---

[7] The PHX dimensions are fixed (generally the PHX is much bigger as possible and so it can be assumed that a bleed air flow rate reflects into a PHX outlet temperature increase

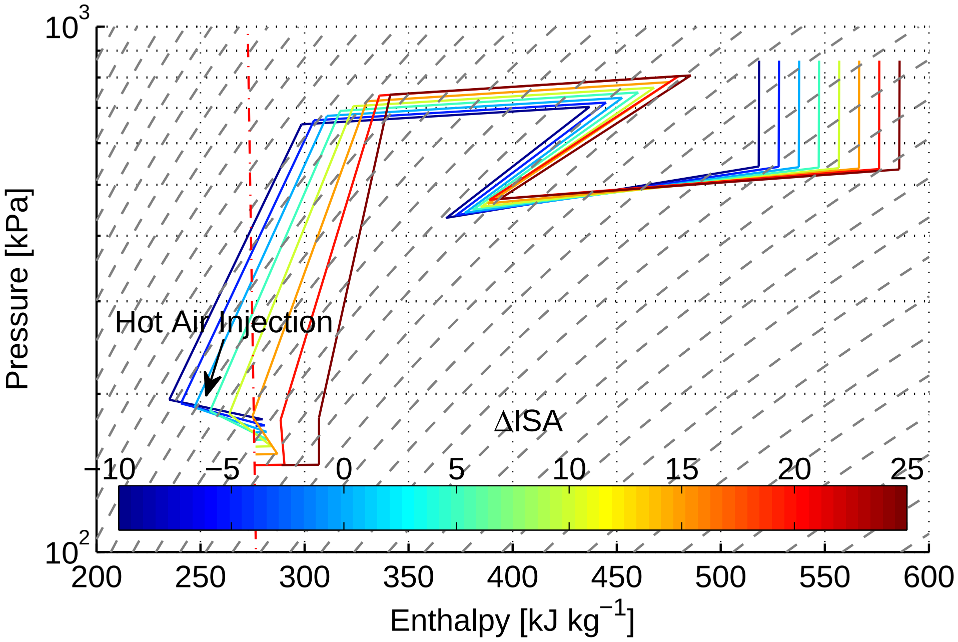

(a) thermodynamic diagram log P-h

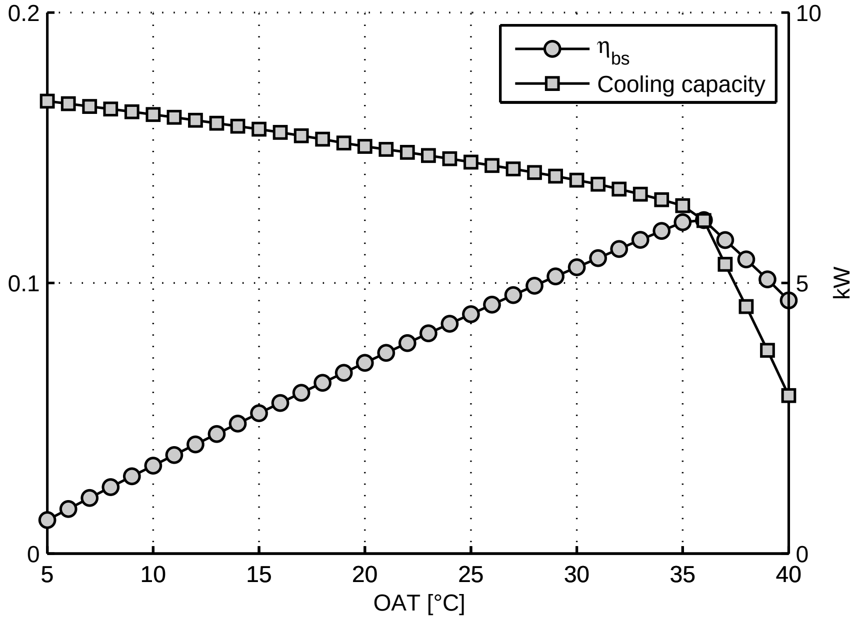

(b) cooling capacity and η_{bs}

Figure 5.8: Bootstrap cycle simulation results at various OAT, on ground and with Ξ=50 %, φ=50 %

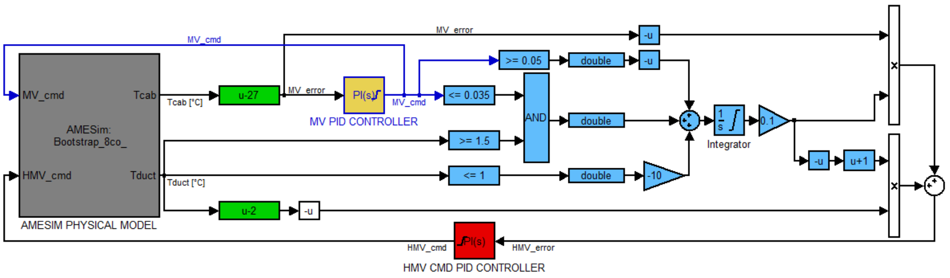

Figure 5.9: Bootstrap cycle control law. The same control logic is used either with the standard architecture and the compressor inlet valve architecture. In the first case the MV PID controller is fixed to 1

the cabin is higher than 2 °C; increasing the heat load the valve progressively closes reducing the cabin inlet temperature and increasing the efficiency of the cycle, when the heat load is too high the valve stops to close maintaining a cabin inlet temperature of 2 °C; at this point the cabin temperature increases since the system is not more able to provide enough cooling power.

A possible strategy to reduce the cooling capacity of the system with keeping the efficiency as high as possible is obtained introducing a valve between the PHX outlet and the compressor inlet. This modulating valve has two effects: it reduces the turbine pressure ratio, thus the ACM speed and the turbine outlet temperature, and reduce the flow rate entering into the ACM branch of the system. The drawback is a reduction of the maximum cooling capacity of the system due to the additional pressure drop (minimized using a butterfly valve).

A rough control logic has been built to control the two valves (see figure 5.9), keeping as target a compartment temperature of 27 °C and a cabin inlet minimum temperature of 2 °C. The control law uses two PID controller to generate the command signal to the valves; the command to the modulating valve (the one in series to the ACM) lies only the compartment temperature; the command to the hot modulating valve (the one which bypass the ACM) depends mainly from the compartment inlet temperature, but if the modulating is near the full close position, and the temperature of the air entering into the compartment is above 2 °C the PID commands the valve to open increasing the compartment inlet temperature and the compartment temperature.

A batch of simulations has been performed on ground with an OAT of 25 °C, a Ξ of 70 % and changing only the compartment thermal load.

The developed logic well controls the temperature giving priority to the cabin inlet temperature requirement (see figure 5.10(b)); the additional valve permits a reduction of the bleed flow rate, and so the efficiency of the system when it is not working with full thermal loads (see 5.10(a)). There is no gain

of maximum efficiency of the system.
The analysis of the thermodynamic cycle of the new proposed architecture (figure 5.10(c)) gives some interesting information. The use of the modulating valve minimizes the hot air injection, and reduces the air bled from the engine. The mass flow reduction means a reduction of the hot fluid flow rate into the PHX, thus the efficiency of the PHX increases determining a lower compressor inlet temperature . Also the SHX hot flow rate decreases, but in this case the increased efficiency has not a big impact on the cycle due to the low mean logarithmic temperature present on this HX. On both the HXs is visible the effect of a lower hot fluid flow rate on the pressure drop.

5.4.2 Engine port switch and variable PRSOV

The main contribution to the inefficiency of the cycle is the PRSOV pressure reduction and, if present the modulating valve pressure loss, (see figure 5.8(a) and figure 5.10(c)): the system utilizes only a part of the energy available and waste the remaining as pressure drops.
The efficiency of the cycle is optimized if the conditions at bleed engine port does not change with the throttle, and remains fixed at the optimum level for the ECS. This conditions can be obtained: continuously changing the stage of the engine compressor at which the air is bled. This solution cannot be adopted since it is too invasive for engine; the engine is generally equipped with 2 bleed ports: one port at high compressor stage, and one at low compressor stage. The high pressure port is used when the aircraft throttle is low, the low pressure port is used when the throttle is high.
A modified PRSOV is installed on the high pressure bleed port. The pressure of the reference chamber is controlled by a relief valve that read the PRSOV upstream pressure: when the upstream pressure is above the cracking point the relief valve opens venting the reference chamber and so closing the valve, viceversa when the upstream pressure is below the cracking point, the relief valve is closed pressurizing the reference chamber opening the valve. On the low pressure port is installed a check valve to prevent back flow to the engine when the high bleed port is open.
Two low pressure ports have been considered a very low pressure port (max pressure 600 kPa) and an intermediate pressure port (max pressure 1000 kPa).
The use of a low pressure port increases the efficiency of the cycle, but reduces the cooling capability of the system (the maximum cooling capability is near the full throttle condition); the intermediate port is a give-and-take between efficiency and cooling capability, the maximum cooling capability is obtained near Ξ 60 % and the maximum efficiency is around the 45 %. The transition between the high pressure stage and the lower pressure stage happens when Ξ is around the 40 % and the discontinuity generated by the

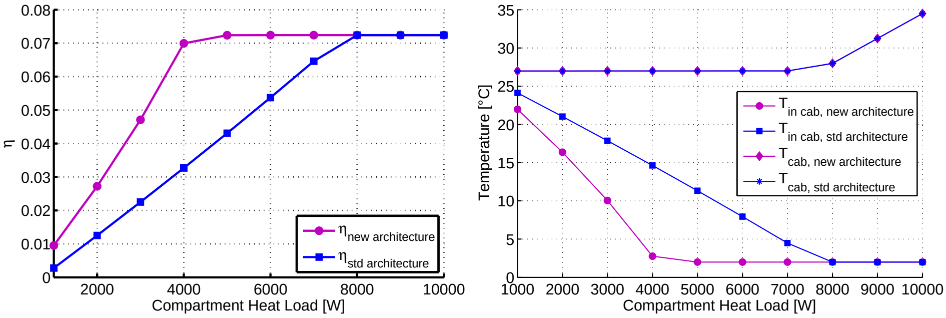

(a) Efficiency **(b)** Controlled temperatures

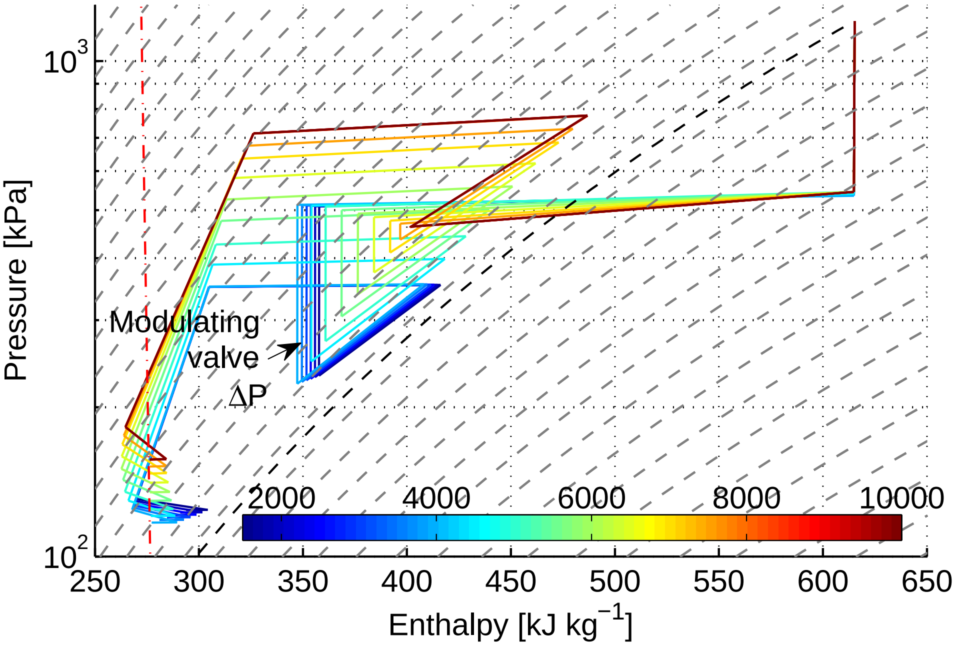

(c) Thermodynamic diagram

Figure 5.10: Bootstrap system performance at various loads. Simulations performed with an *OAT* of 25 °C and a Ξ of 70 %

port switch is clear visible either in figure 5.11(a) and 5.11(b).
The cabin temperature is fixed (27 °C), up to when the system is able to provide air at the minimum allowed temperature (2 °C) the performance of the system are linked only to the mass flow rate. The turbine is the item limits the flow rate, if the rotational speed of the ACM increases also the system flow rate increases. The ACM speed is determined by the equilibrium point between power absorbed by the compressor and power generated by the turbine (see equation (5.2.12)), so increasing the pressure ratio across the turbine the (equation (5.2.6b)) ACM speed increases and also the system flow rate.
The pressure ratio across the turbine is obtained by increasing the PRSOV setting point.
The increase of the bleed flow rate has two main drawbacks:

- the ϵ of the HXs decreases
- the temperature rise across the compressor increases

Both these two drawbacks impacts the turbine inlet temperature and, according to equation (5.2.6a) the turbine outlet temperature. Up to when the turbine outlet wet temperature is lower than 2 °C, the cooling capacity of the system increase if the flow rate increase, but the cooling capacity falls down as soon as the turbine outlet wet temperature is higher than 2 °C (see figure 5.12(b)).

5.5 Bleed-less air cycle

The characteristics (Pressure and temperature) of the air bled from the engine change with the variation of the throttle; a PRSOV is installed upstream the ECS to limit the pressure inside the circuit. The pressure drop created by this valve is one of the big contributor of the poor efficiency of a bootstrap cycle. In previous paragraph a traditional way to improve the efficiency has been analyzed, but there is a more invasive option that can be adopted: use a bleed-less approach.
Various studies have been performed to develop the idea of an all, or at more, electrical aircraft. **?** summarizes the main resources activities performed. The european project More Electrical Open Technologies (MOET) proposes a solution based on a combination of a Vapor Cycle cooling System and an Air Cycle Cooling System. Boeing is the first aircraft manufacturer develops a complete electrical aircraft.
To create an bootstrap cycle bleed-less a compressor driven by an electrical motor has to be installed. This compressor can modulate the pressure at the PHX inlet by changing its own rotational speed, and so there is no need of PRSOV. The additional weight due to the compressor is partially mitigate by the use of an aluminium PHX (now usable since the temperatures are

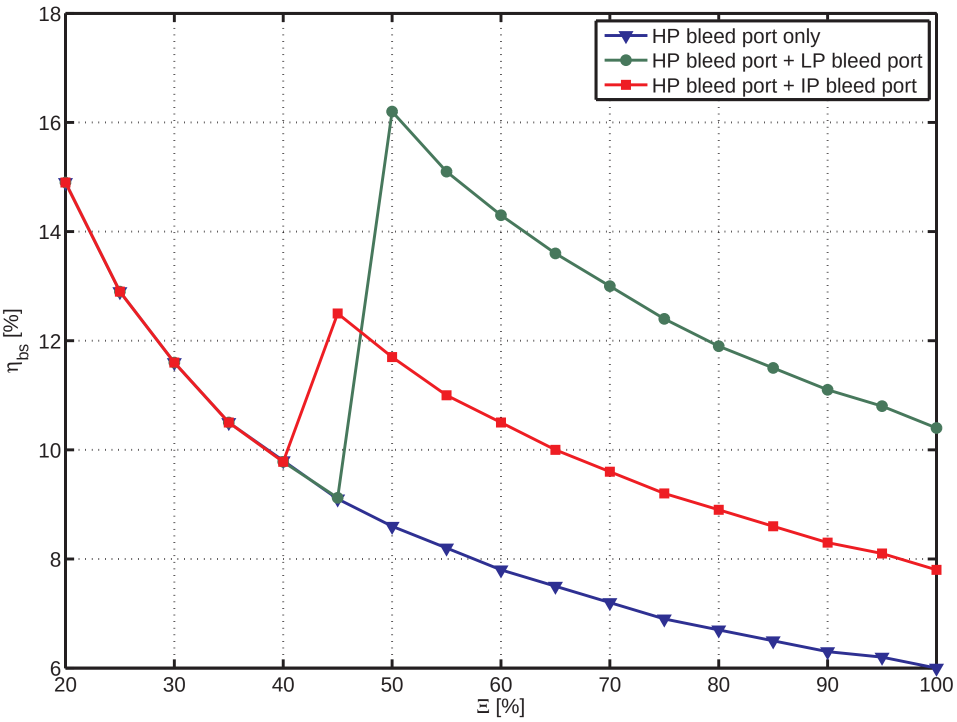

(a) η_{bs}

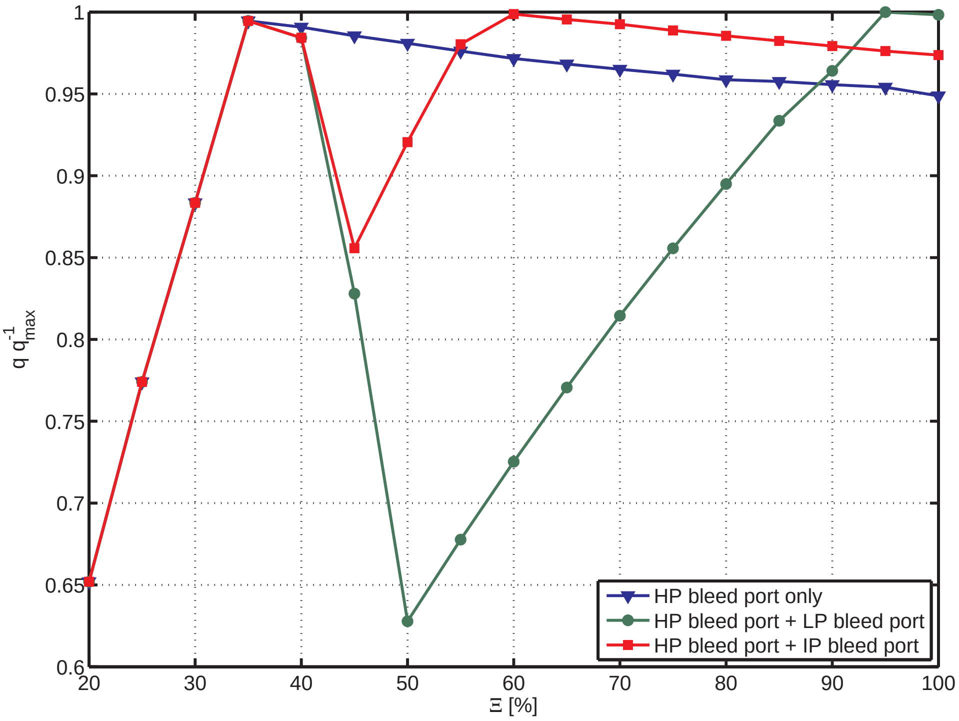

(b) Cooling Capacity

Figure 5.11: Bootstrap cycle performance at various bleed ports

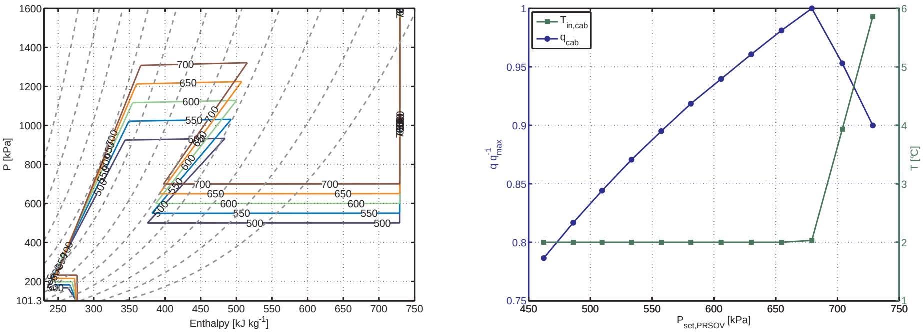

(a) Thermodynamic cycles P-h

(b) Q_{CAB} and $T_{\mathrm{IN,CAB}}$

Figure 5.12: Bootstrap cycle performance at various regulated pressure. Simulation performed setting the ambient absolute humidity to 13 g kg^{-1}, the Ξ to the 95 % and the OAT equal to 45 °C

drastically reduced). In the mathematical model the new compressor process is assumed as a polytropic process having a coefficient of 1.5.

Figure 5.13 shows the schematic of the system; figure 5.14 shows the comparison between a traditional bootstrap cycle with an engine working with Ξ around the 70 % and a bleed-less cycle at the same external conditions (OAT=40 °C, φ=50 % and on ground).

In the conditions simulated, the normal bootstrap cycle pays in addition to the PRSOV the condensation effect at the turbine outlet, and it is not able to arrive at a compartment inlet temperature of 2 °C; at the end the efficiency is around the 7 %. The bleed-less cycle can modulate the primary compressor performance, reducing the air flow rate and decreasing the compartment inlet temperature, in such way the overall efficiency is increased arriving at the 25 %.

The bleed-less bootstrap cycle is three times more efficient than a standard bootstrap cycle. The strategy to use the primary compressor to modulate the cooling capacity of the system is the best way to control the system but it cannot guarantee the coverage of all the envelope, since the compressor can be brought to work in un-safe conditions (surge or chocking), the system still need a by-pass valve, but its use is limited to the operational envelope corners.

5.6 Performance evaluation on a Oil & gas mission profile

The performance of a standard bootstrap and a bleedless cycle are analyzed on a typical Oil & Gas mission profile, using as heat load the model of the

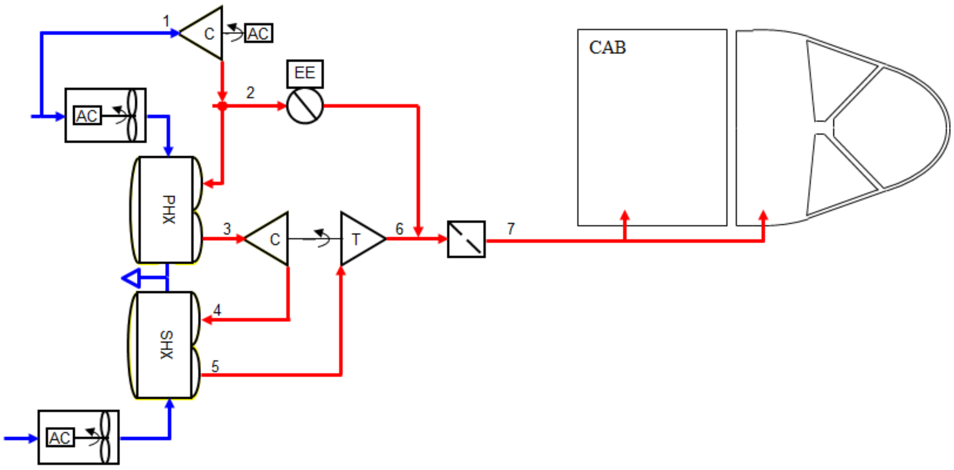

Figure 5.13: Bleedless bootstrap cycle sketch

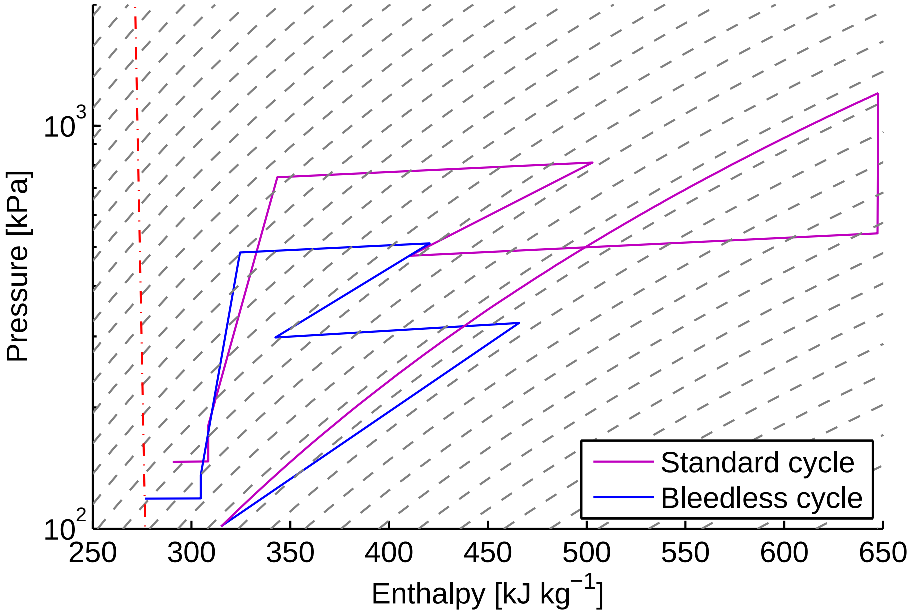

Figure 5.14: Bootstrap bleed-less cycle vs. bootstrap standard cycle. Comparison of the thermodynamic diagrams of the two approaches. The OAT is 40 °C and the φ is 50 %, the Ξ is the 70 %

tilt rotor described in section 4.3.
The mission profile has eight phases:

Pre-flight
The aircraft is on ground making the preliminary check for the flight and waiting the clearance for take-off. The duration of this phase is 5 min.

Take-off
The aircraft start to climb and to accelerate. The climb rate is fixed at $1500\,\mathrm{ft\,min^{-1}}$ and the speed at the end of the phase (time span 1 min) is 220 kn.

Climb
The aircraft climbs to the cruise altitude of 22 500 ft keeping a climb rate of $1500\,\mathrm{ft\,min^{-1}}$ and a speed of 220 kn.

Cruise
The aircraft continues the flight at constant speed (220 kn) and altitude (22 500 ft) for 120 min.

Descent
The aircraft descents to the destination airport, at constant speed (220 kn) and at with a constant descent ratio of $750\,\mathrm{ft\,min^{-1}}$. This phase ends when the aircraft reaches an altitude of 1500 ft.

Airport circuit
The aircraft waits 10 min into the airport traffic circuit its own landing slot. The speed of the aircraft is reduced at 150 kn.

Landing
the aircraft pass into rotorcraft configuration reducing to 0 kn its speed within 80 s. At this point it lands on the airport surface (descent rate equal to $750\,\mathrm{ft\,min^{-1}}$).

Taxi
The aircraft moves to the parking are and switch off all the equipments (duration 3 min.

At sea level the relative humidity is 50 %, and the *OAT* is 40 °C. The variation of the ambient conditions with the altitude follow the model described in section 4.1.

5.6.1 Control laws

The systems have two control laws:

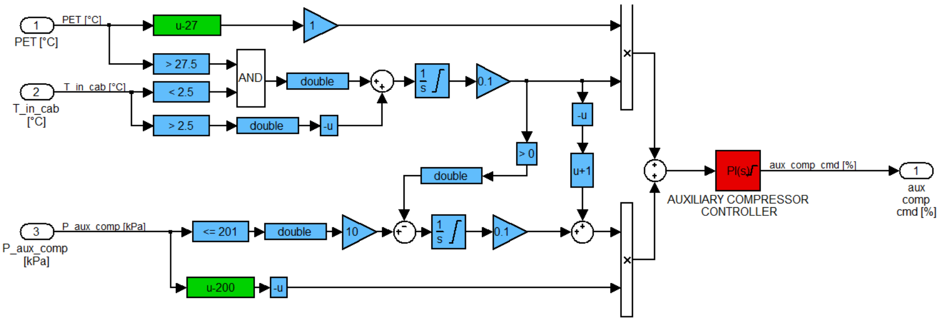

Figure 5.15: Auxiliary compressor control law

- one controls the compartment temperature and the compartment inlet temperature
- one controls the pressure at the inlet of the system.

This last control is made by the PRSOV in the standard bootstrap cycle, and by the variable auxiliary compressor in the bleedless cycle. Both the controls are set to preserve the pressurization function. The PRSOV has been set to limit the pressure at 200 kPa gauge, while a small control law adjusts the speed of the compressor to maintain the pressure at compressor outlet higher than 195 kPa.

The control logic drives the system is simple (see figure 5.9): it adjusts the by-pass valve setting to maintain the selected compartment temperature (27 °C); if the compartment inlet temperature falls below 2 °C the logic acts to avoid the undercoming of this threshold. The passage from one target temperature to another is managed introducing a linear interpolation between the two temperatures. The control law is a PI with a limited output and using the clamping as anti-windup method.

The control law manages the auxiliary compressor speed is still a PI, but in this case the anti-windup method is done by back-calculation using a back calculation coefficient equal to the integrating coefficient. The first target of this control law is to maximize the efficiency of the cycle keeping as low as possible the compressor pressure (lower branch of the figure 5.15 schematic), but enough high to preserve the pressurization function ($P_{\text{target}} = 200\,\text{kPa}$). If the system is not able to provide the required cooling power, thus PET $> T_{\text{target}} \& T_{\text{in,cab}} < 2.1\,°\text{C}$), the control law increases the auxiliary compressor speed increasing the cooling capacity of the system (higher branch of the schematic). To avoid discontinuities in the auxiliary compressor command, the changeover between the two philosophies is done within 10 s increasing linearly the influence of the new target on the PID, while the old target decreases following the same rule.

5.6.2 Results

The efficiency defined with equation (5.3.2) is not very useful in this case where the OAT varies from 40 °C to −5 °C, but changing the OAT with the compartment temperature, as shown in equation (5.6.1), the issue is solved.

$$\eta_{\mathrm{bs}^*} = \frac{\dot{m}_{\mathrm{in,cab}}(T_{\mathrm{in,cab}} - T_{\mathrm{cab}})}{\dot{m}_{\mathrm{bleed}}(T_{\mathrm{bleed}} - OAT)} \tag{5.6.1}$$

The standard bootstrap cycle waste a lot of energy when the aircraft is on-ground (see blue curve of 5.16(c)). The temperature is delivered at the compartment inlet around 6 °C. The bleedless bootstrap cycle is more efficient and the temperature at the compartment inlet is near the minimum allowed value (2 °C), in such way the flow rate is minimized as the energy consumption.

During the fly phases (take-off, climb, cruise, descent and landing) both the system increases their maximum cooling capacity since the OAT and the external air φ descreases with the respect of the altitude. The same two parameters drive also the compartment thermal load which also decreases reducing the demand of cooling power. The two systems react at the decreased request of cooling capacity increasing the temperature of the air entering into the compartment, thus opening the by-pass valve. The efficiency of the cyles falls (see figure 5.16(b)). The bleedless cycle efficiency drops faster than the standard system since the auxiliary compressor speed increases to maintain the minimum allowed pressure.

Figure 5.16(a) shows how the developed control laws for both the systems maintain the compartment temperature within ±0.5 °C the target temperature (27 °C). The standard bootstrap cycle balance perfectly the compartment requirement and its own cooling capability; the bleedless system is less accurate expecially when both the control laws acts to control the compartment temperature. In fact after the take-off and just before landing there is a small increasing in the compartment heat load (see paragraph 4.3.2), the system is not more able to keep the compartment temperature since the by-pass valve control law adjust the by-pass valve opening to avoid the undercoming of the threshold on the cabin inlet temperature; the control law on the auxiliary compressor increases the speed of the unit to provide more cooling capacity, thus adjusting the compartment temperature. The simultaneous work of the two control law creates the small overshoot.

The benefits of the bleedless cycle are clearly shown in figure 5.16(b), but they became even higher if we look at the whole mission. SAE-AIR-1168/8 [2004] gives the equations for a preliminary evaluation of the fuel penalty. The hypothesis behind the SAE-AIR-1168/8 [2004] formulas are mainly:

- Air vehicle weight is assumed fixed, and degradation in range occurs as a result of weight displacing fuel

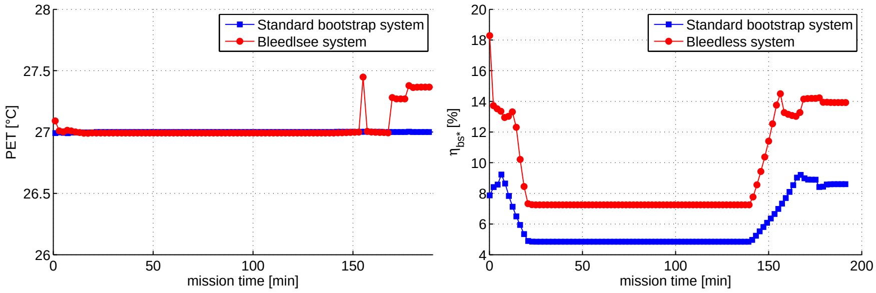

(a) PETs **(b)** cycle efficiencies

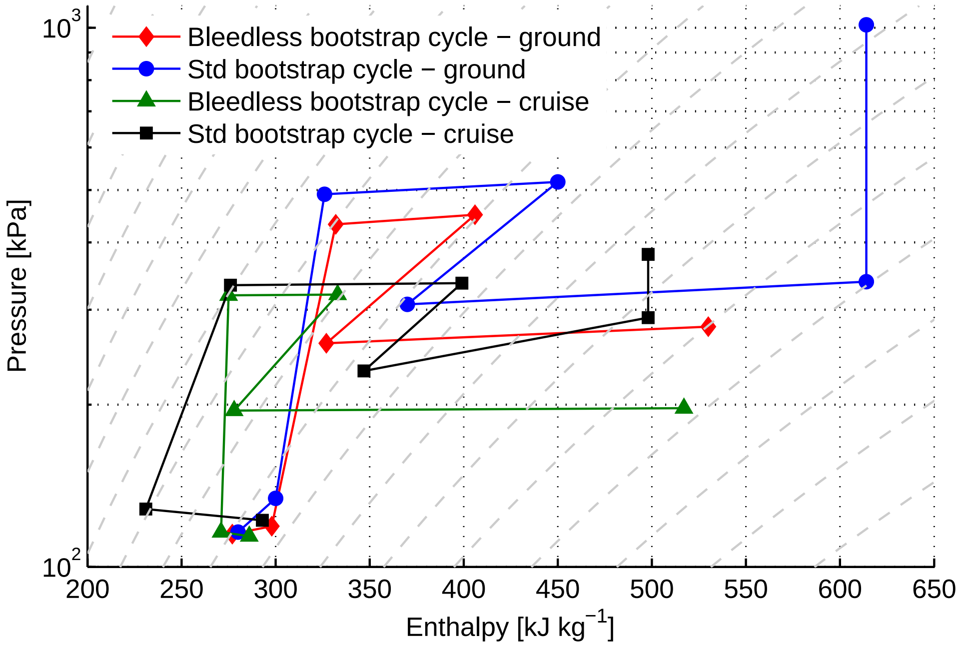

(c) thermodynamic diagrams

Figure 5.16: Oil & Gas mission simulation results

- Range is assumed fixed, and the resultant take-off weight penalty id added to the total airplane weight

In addition to the above hypothesis, we considering also that:

- the bleedless system is heavier than the standard bootstrap cycle of 25 kg. This weight includes the additional auxiliary compressor mitigated by the PHX made in alluminium instead of stainless steel.
- The RAM scopes of the two system are identical
- the Lift to drag ratio (L/D) of the airplane is 6
- the Specific Fuel Consumption for thrust (SFC_t) is $3\,\mathrm{lb\,h^{-1}\,lb^{-1}}$
- the Specific Fuel Consumption for power (SFC_p) is $0.5\,\mathrm{lb\,h^{-1}\,hp^{-1}}$
- all the calculations are done using the average values of bleed air extraction, bleed air temperature and electrical power consumption

The Take-off fuel weight penalty ($W_{\mathrm{f,0}}$) due to horsepower extraction is calculated using equation (5.6.2); the result of this equation is an estimation of fuel quantity used to generate the electrical power which provides energy to the system.

$$W_{\mathrm{f,0}} = \frac{W_{\mathrm{el}}\mathrm{L/D}SFC_p}{SFC_t}\left(\exp\left(\frac{SFC_t t_{\mathrm{fl}}/3600}{\mathrm{L/D}}\right) - 1\right) \tag{5.6.2}$$

Equation (5.6.3) estimates the increase of the $W_{\mathrm{f,0}}$ due to the bleed air extraction. Equation (5.6.3) is quite different respect to the one presented in SAE-AIR-1168/8 [2004], where the denominator of the temperature ratio is 1111 K instead of the maximum bleed temperature ($T_{\mathrm{bleed,max}}$). The $W_{\mathrm{f,0}}$ due to fixed weight is calculated using equation (5.6.4).

$$W_{\mathrm{f,0}} = 0.0335\frac{\mathrm{L/D}T_{\mathrm{bleed}}m_{\mathrm{bleed}}}{SFC_t T_{\mathrm{bleed,max}}}\left(\exp\left(\frac{SFC_t t_{\mathrm{fl}}/3600}{\mathrm{L/D}}\right) - 1\right) \tag{5.6.3}$$

$$W_{\mathrm{f,0}} = M_{\mathrm{fix}}\left(\exp\left(\frac{SFC_t t_{\mathrm{fl}}/3600}{\mathrm{L/D}}\right) - 1\right) \tag{5.6.4}$$

The total system take-off fuel weight penalty of the bleedless system for the Oil & Gas mission considered is the 45 % less than the standard bootstrap cycle.

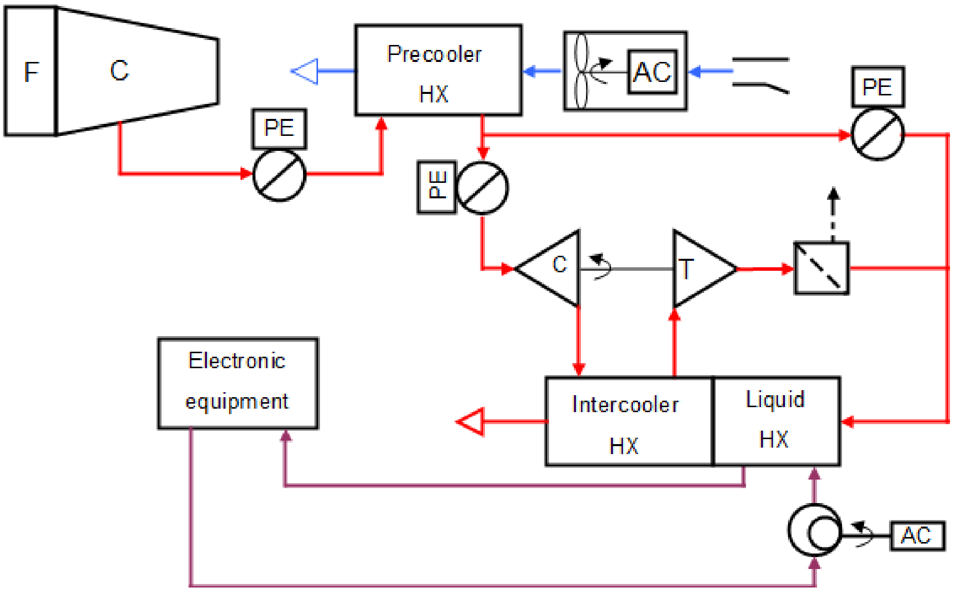

Figure 5.17: Bootstrap cycle for electronic cooling sketch

5.7 Air cycle for electronic cooling

The cooling of the electronic equipment is generally performed using the external air; in some cases, where the electric power is high, the external air is not sufficient and a dedicated cooling system is required to control the temperature of the equipment.

The use of a liquid loop to distribute the cold secondary fluid at the equipments gives a lot of benefits in terms of flexibility and installation.

Figure 5.17 shows a possible design for a bootstrap cycle dedicated to electronic cooling. The pressurized air bled from the engine is controlled by a PRSOV to limit the maximum pressure of the air circuit. a PHX reduces the temperature of the air entering into the ACM compressor. After the compressor another HX is installed. After the turbine the extreme cold air enters into a air-to-liquid HX where the secondary fluid is cooled. The air exits from the air-to-liquid HX is still at low temperature (compared with ambient temperature) and so it is used to cool down the air after the compression; in such way a part of the energy is recovered increasing the efficiency of the cycle. The partialization valve is installed before the compressor limiting the flow rate to the air cycle machine. This approach is applicable in this case since the system has not to provide a minimium flow rate as happens in the system used to cabin cooling.

Parameter	Unit	Value
Loop volume	m^3	100
Electronic thermal capacitance	$\mathrm{kJ\,K^{-1}}$	50
Liquid c_p	$\mathrm{J\,kg^{-1}\,K^{-1}}$	3084

Table 5.2: electronic equipment liquid loop data

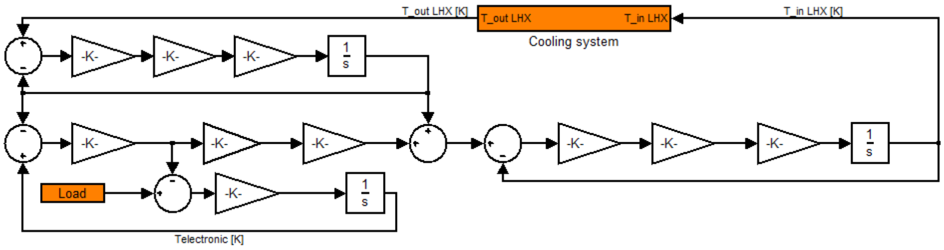

Figure 5.18: Liquid loop Simulink model

5.7.1 The mathematical model

Also in this case a mathematical model has been created to study the behavior of this architecture.The model is widely based on the model described in section 5.3.

The liquid loop is roughly modeled. The pump is assumed able to provide a flow rate of $250\,\mathrm{g\,s^{-1}}$, adding 1 kW to the thermal load of the loop. The liquid is pumped into a reservoir and then it goes into the air-to-liquid HX. The performarce of the HX has been calculated using the model detailed in section 2, and validated as shown in figure 2.6. The liquid, cooled by the HX, arrives to the electronic equipment. The interface between the electronic equipment and the liquid is a cold plate having the product between the overall heat transfer coefficient and the heat exchange area equal to $500\,\mathrm{W\,K^{-1}}$. The circit is closed on the pump. The main characteristics of the liquid loop are reported in table 5.2 and the model is shown in figure 5.18.

The cooling capacity is controlled modulating the system flow rate thanks to a regulating valve installed downstream the turbine. The control valve is located here to avoid possible issues due to the coupling of the two control valves (the modulating valve and the PRSOV).

5.7.2 Performance on the Oil & Gas mission profile

The behavior of the system is analyzed simulating the same mission profile of section 5.6. All the liquid inside the secondary loop is at 70 °C at the starting of the simulation. The Δ_{ISA} is 25 °C and the φ is 45 %.

When the system is switched on, the electronic is kept off until the temperature of the liquid at the air-to-liquid HX reaches 40 °C. The system cools down the loop in 5 min. The temperature of the electronic equipment stabilizes around 48 °C, when the equipment is switched on: the system is not able to provide air enough cold to further decrease the payload temperature. The temperature at the turbine outlet progressively decreases with the increase of the altitude (climbing phase), and the equipment temperature follows this trend. When the equipment reaches 30 °C the control system starts to increase the turbine backpressure modulating the HX air temperature and flow rate. After a small undershoot the electronic temperature is kept at 30 °C without issues. During the descent phase the temperature of the OAT increases again and the temperature of the equipment increases again as during the initial phase.

The behavior of the PRSOV is also interesting. When the aircraft is on ground the piston stroke is around 1.5 mm; during the climb the stroke increases to compensate the pressure reduction from the engine. When the system starts to regulate the cooling capacity (around flight time 18 min), the trend of the PRSOV piston stroke has a discontinuity; the valve reacts to the flow rate reduction , thus to the decreased pressure drop across the main piston, closing the piston keeping under control the downstream pressure. After this discontinuity the valve return to regulary control the pressure. During the descent and landing phases this discontinuity is not present because the turbine backpressure follows a more regular trend.

Figure 5.19(d) shows the comparison between the proposed control strategy and a system with a standard partialization philosophy (by-pass valve); at full power (aircraft on ground) both the system has the same bleed flow rate consumption; but during the flight the proposed system control the temperature reducing the bleed air flow rate, thus the fuel consumption (see equation (5.6.3)). The proposed system reduces the bleed air consumption of the 30 %.

5.7.3 PRSOV behavioir

The proposed control strategy reduces drammatically the fuel consumption, but could bring some issue on the PRSOV stability. In fact, as show in figure 5.20, if the flow rate is reduced below a certain threshold[8], the valve is not more able to control the pressure and the piston hammers again the ends stroke. This issue is linked to the response time of the volume downstream the valve respect to the response time of the valve reference chamber (smaller volume downstream the valve increases the stability of the system). To avoid this instability the intervention of the modulating valve has to be limited to a minimum value. If the cooling capacity has to be further reduced, the

---

[8] this threshold is a function of the system volume

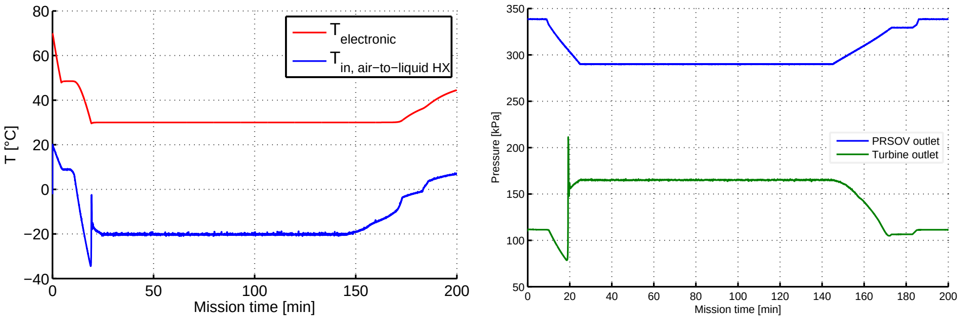

(a) Temperature trends

(b) Pressure trends

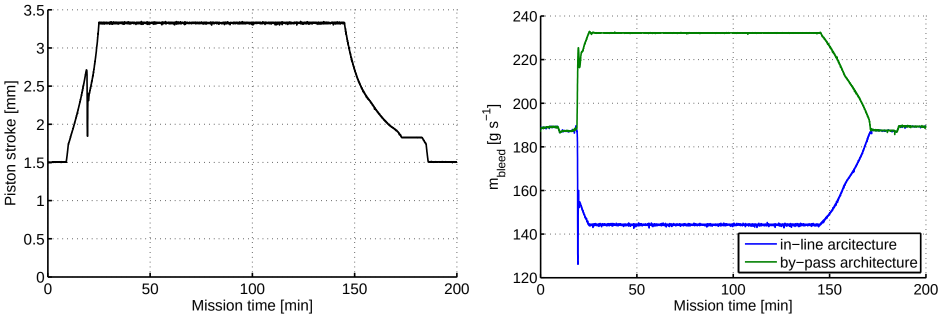

(c) PRSOV piston stroke

(d) bleed air extraction

Figure 5.19: Electronic cooling behavior on a Oil & Gas mission profile

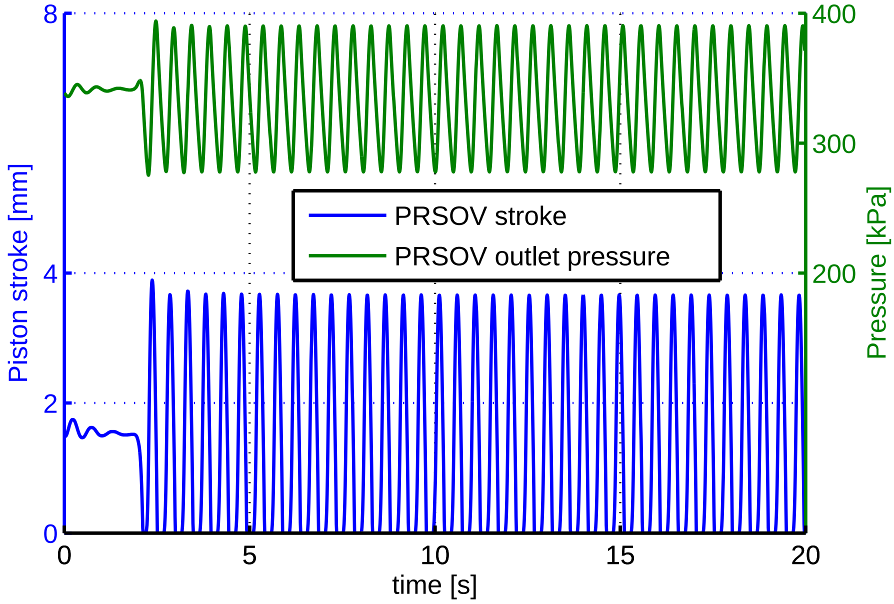

Figure 5.20: Electronic cooling system PRSOV instability. Simulation performed on ground and in ISA conditions.

system has to close the modulating valve opening at the same time the by pass valve to preserve the minimum flow rate the PRSOV needs to avoid instability: in this way the reduction of fuel consumption is obtained and the breakage of the PRSOV is avoided.

The PRSOV setting point on a normal bootstrap cycle is selected to avoid to exceed a temperature of 250 °C at the compressor outlet in the worst operating conditions (ground, Δ_{ISA} 25 °C). Figure 5.21 reports this operating point in red for the regerative architecture under analysis. This operating point is not the optimum one; figure 5.21 shows the optimum setting point (in terms of performance) correponds to another setting of the PRSOV. This behavior is due to the use of a regenerative HX increases the efficiency of the system, but it implies that the performance of the system are not monotone; the temperature at the air-to-liquid HX inlet depends from the ACM performances which are linked to the temperature at the regenerative HX inlet which lie on the temperature at the air-to-liquid HX inlet: the circle is closed.

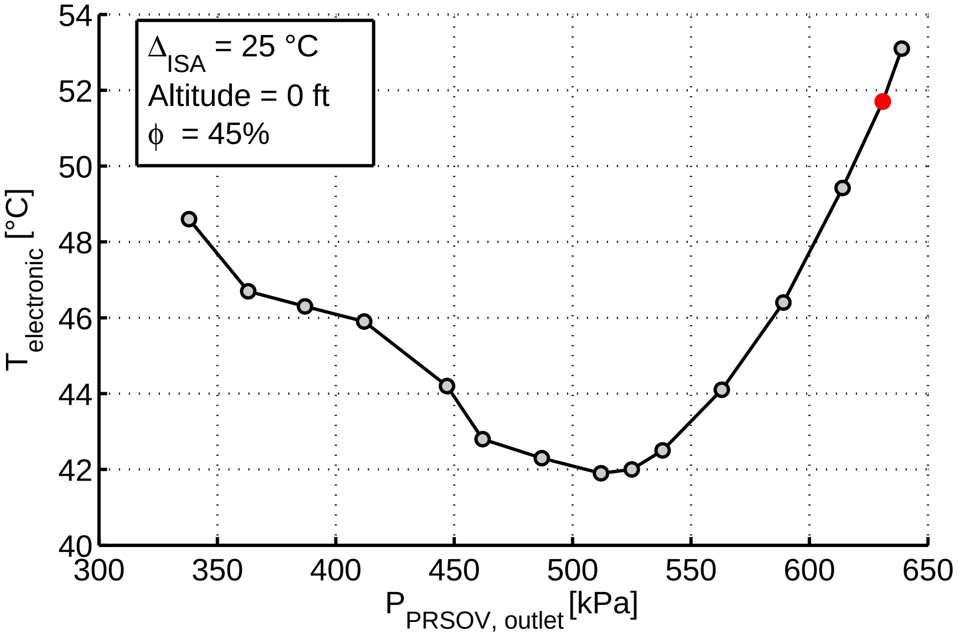

Figure 5.21: Electronic cooling system optimum setting. The red point corresponds to the PRSOV maximize the compressor outlet temperature (250 °C)

Chapter 6

ECS: Vapor Cycle Systems

6.1 Introduction

The VCSs are widely used to the thermal control of the helicopters and small aircrafts which do not need a pressurization system. On the large aircraft the VCSs are used to cool the galleys and the electronic systems.

6.2 Equipment mathematical models

A VCS consists mainly of the following parts:

- compressor
- condenser
- evaporator
- expansion device
- fans
- control valves
- accumulator
- filter

All these components are modelled as "black boxes" using correlation data supplied by the component manufacturers. In the following paragraphs a brief explanation of the main system component function and how they are modeled is presented.

6.2.1 Compressor

The compressor converts the mechanical energy into fluid energy increasing the pressure of the gas. There are various type of compressors, in this work we selected a scroll compressor. The scroll compressor uses two scrolls, one fixed and one orbiting, to create several gas pockets. The volume of the pocket decreases gradually from the suction to the discharge thanks to an eccentric relative movement of the orbiting scroll respect to the fixed scroll. The gas into the pocket is compressed by the volume change. The scroll compressors are widely used in the economized cycles where some cool gas refrigerant is injected in an intermediate compression phase increasing the efficiency of the process. Spazian [2009] developed a mathematical model to describe the compression process of an economized scroll compressor. The model is based on the work of Chen et al. [2002b,a] and Wang et al. [2005]. Some tests have been performed to verify the prediction of the model. The mathematical model results shows a great affinity with the experimental results (see figure 6.1). The mathematical model has been used to create the compressor performance curves used in the VCS model. The curves have been obtained fixing to $0\,\mathrm{g\,s^{-1}}$ the flow rate on the economized port obtaining in this way a non-economized compressor.

6.2.2 Condenser

The condenser plays a fundamental role in the performance of a VCS, it rejects the heat of the system (compressor heat load plus evaporator heat load) to the ambient condensing the refrigerant.
Three parameters drive the selection of the HX:

- low weight
- small envelope
- high efficiency

The aluminum minichannels condensers and the microchannel condensers perfectly respond to the above characteristics. Those technologies are widely used in the automotive field. Figure 6.2 shows a schematic of a flat tube and fins type condenser. A row of flat tubes, having an external thickness of about 1 mm, is brazed between two cylindrical collectors. The refrigerant flows inside the collectors and the tubes. A very thin fin is brazed inside the tubes to enhance the heat exchanged on the refrigerant side, while another fin, brazed between the tubes, improves the heat exchange efficiency on the air side. The result is a very large total surface exposed to the fluids which allows an overall efficiency comparable to the plate & fin design.
A lot of work has done to create trustable models that are able to reproduce the behavior of those type of heat exchanger. Asinari [2004] describes one

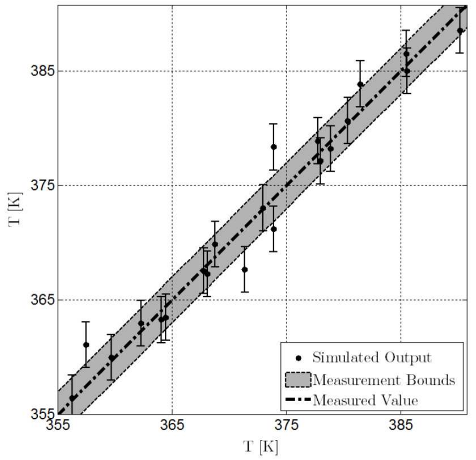

(a) Discharge temperature

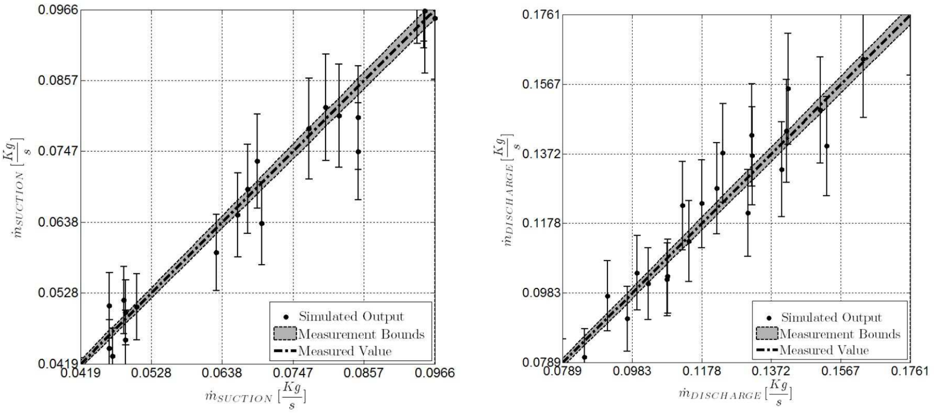

(b) Suction flow rate **(c)** Discharge flow rate

Figure 6.1: Comparison between compressor mathematical model and experimental results

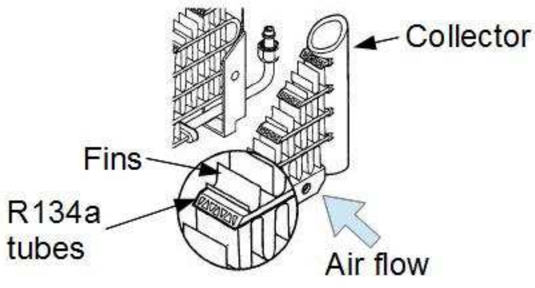

Figure 6.2: Condenser sketch

Parameter	Unit	Value
finned tube width	mm	600
finned tube depth	mm	12
collector cross-sectional area	mm^2	380
R134a side cross-sectional area per tube	mm^2	16.9
R134a side hydraulic diameter	mm	4.64
fin pitch	mm	3
fin thickness	mm	0.12
tube periodicity	mm	10.14
external tube height	mm	1.93

Table 6.1: condenser geometrical characteristics

of the most trustable model, and Martínez-Ballester et al. [2011, 2012a,b] presented another mathematical model to predict the performance of microchannels HXs. In the present work the condenser is roughly modeled using the standard model of AMEsim (see LMS Imagine S.A. [2012]); the program uses for the external heat exchange an empirical formulation based on basic Nusselt number (Nu) formulation (equation (6.2.1)); the refrigerant heat exchange is computed using the correlations suggested by Martínez-Ballester et al. [2012a] for pressure drops and condensation. The coefficients of equation (6.2.1) has been trimmed to match author experimental results.

$$\mathrm{Nu} = 0.04\mathrm{Re}^{1.2}\mathrm{Pr}^{0.45} \tag{6.2.1}$$

The main characteristics of the condenser are reported in table 6.1.

6.2.3 Evaporator

The evaporator plays the opposite role of the condenser: it absorbs heat from the external ambient cooling down the fluid which flows externally to the unit (generally air). There are several types of evaporators, but as for the condenser the microchannels HXs are the best compromise in terms of low weight and high performances[1].

The main characteristics of the evaporator are reported in table 6.2, and the performance curve (obtained from manufacturer data) are shown in figure 6.3.

6.2.4 EXV

The EXV plays the same role of a thermostatic expansion valve (TXV): it laminates the refrigerant which arrives from the compressor regulating

---

[1] The only current limitation is the burst pressure which is not full compatible with aeronautic standards

Parameter	Unit	Value
finned tube width	mm	308
finned tube height	mm	200
finned tube depth	mm	45
surface area	dm^2	5.1
fins density	fins fins/dm	75
fin thickness	mm	0.12

Table 6.2: evaporator geometrical characteristics. The refrigerant side has three passages, the first and the third ones have 16 tubes, the second 11

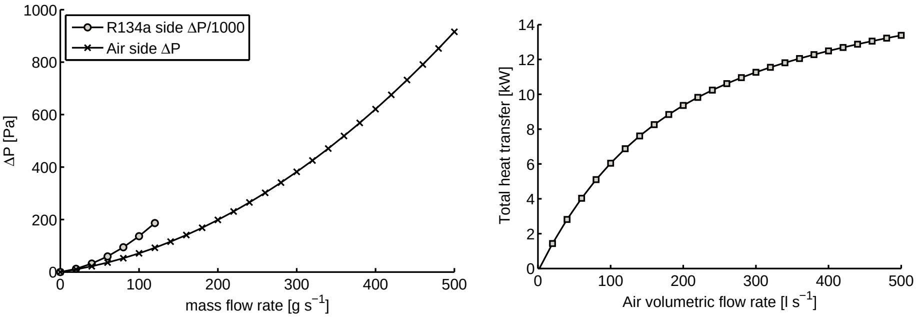

(a) Pressure drops **(b)** Total heat transfer

Figure 6.3: Evaporator maps

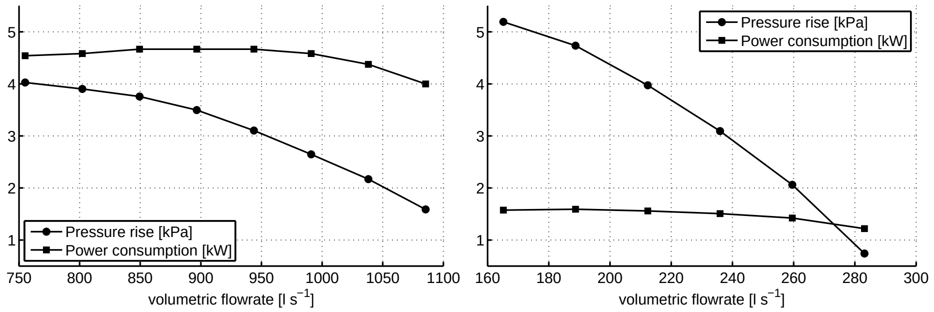

(a) Condenser fan **(b)** Evaporator fan

Figure 6.4: VCS fan performance curves in standard conditions ($\rho = 1.225\,\mathrm{kg\,m^{-3}}$).
The data is from http://hsapps.utc.com/hspsfans/

the evaporator pressure to maintain a set Superheating (SH). The TXVs are full pneumatic valve, while the EXVs are electromechanical valves and the command to the valve is provided by an external digital controller. An electrical stepper motor moves a pin which opens or closes the refrigerant passage, the external controller gives the command to the motor reading the pressure and temperature at the compressor suction port.

The EXV is more flexible than a standard TXV, since the digital controller allows the use of complex control logic which can regulates different parameters in the various operational phases. As example the EXV can be kept closed during the start-up to reduce the load on the compressor motor, then during the normal operation the valve can modulate the compartment temperature by increasing or decreasing the target SH; the control logic can also incorporate an additional operational mode to prevent the extreme low pressure operation (in this case the control law is closed directly on the suction pressure).

The valve is modeled as an orifice (see equations (1.2.3) and (1.2.4) for gas, Bernoulli equation for liquid) with a variable flow area.

6.2.5 Fans

The condenser and evaporator fans are modeled as described in section Section 5.2.1. The selected fans are made by Hamilton-Sundtrand and their performance maps are shown in figure 6.4(a) and 6.4(b).

6.3 VCS for Cabin cooling

The mathematical model has been used to study the performance of a VCS system during a typical mission profile, including also the pull down phase. The VCS controls the temperature of a passenger/crew compartment: the target temperature is set to 27 °C, and the Δ_{ISA} is fixed to 25 °C (OAT on ground equal to 40 °C).

A mission profile similar to the one used for the bootstrap cycle (section 5.6) has been adopted for the hereunder described simulations (see figure 6.6); the only difference between the two profiles is the time on-ground before the flight: in these cases the time has been increased since the thermal load of the passenger compartment is higher and the system needs more time to perform the pull down.

The thermal load of the passenger compartments has been simulated using the model described in section 4.3. The passengers entering into the compartment only when the compartment temperature is below 30 °C while the crew is onboard from the start of the simulation. An additional load of 1 kW is added at the same time that the passengers enters into the compartment to take into account of the additional electronic components which are

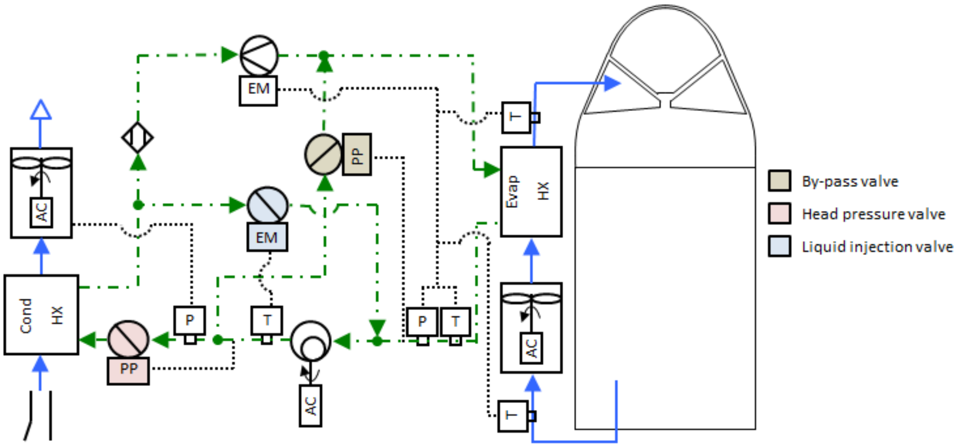

Figure 6.5: VCS schematic. This sketch includes all the features which are describes in the following sections

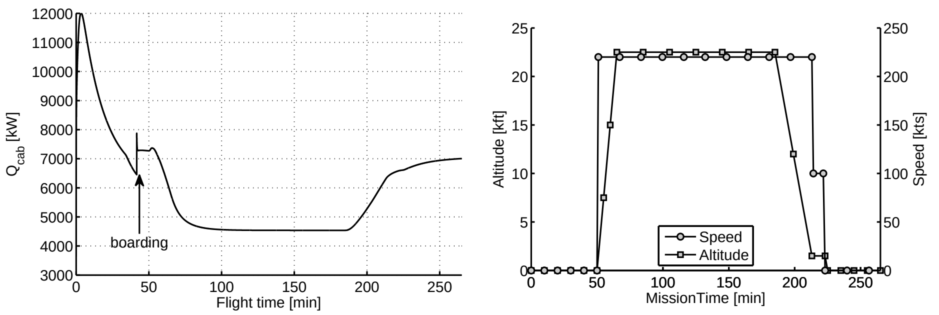

(a) Compartment thermal load profile

(b) Altitude and speed profile

Figure 6.6: VCS mission profile. Note on figure 6.6(a) that after 40 min from the start there is a discontinuity due to the boarding of the passengers

switched on for the passenger entertainment. At $t = 0\,\mathrm{s}$ the temperature of all the surfaces and of the air into the compartments is 70 °C.

6.3.1 Fixed displacement compressor

The first architecture analysed is a simple VCS architecture with a fixed displacement compressor, a variable speed condenser fan (to maintain a minimum compressor discharge pressure, see section 6.5) and an EXV to control the cooling capacity. The EXV opening is controlled by two PIDs: the first one modulates the EXV opening controlling the SH, the second monitors the compartment temperature and it changes the target SH of the first PID increasing or decreasing the cooling capacity of the VCS. The use of an EXV allows also to minimize the SH (the minimum value in the simulations is set to 2 °C) maximizing the performance of the system.

The VCS provides the maximum cooling capacity (SH at the minimum allowed value) while the aircraft is on ground performing the pull down in an acceptable time: the compartment temperature reaches 27 °C within 40 min from the start of the simulation. The boarding of the passengers (around simulation time 40 min) creates a negligible increase of the PET (less than 1 °C). The PET gradually returns to the target value during the first part of the climb (the *OAT* decreases and so the performance of the system increases), and then the control gradually decreases the cooling capacity of the system increasing the target SH; in the descent phase the target SH decreases returning to the minimum allowed value just before the aircraft landing.

The combined action of the 2 controls does not show any instability and either the PET and the SH are kept at the target values. The low COP, figure 6.7(b) shows, is due to the reduced dimensions of the HX; the control strategy does not reduces the COP, it keeps the COP more or less constant.

The architecture studied works perfectly if only the cooling performance are analyzed, but a deeper look to the thermodynamic cycle shows some aspects that can dramatically reduce the reliability of the compressor. The compressor suction pressure falls down to 100 kPa during the cruise phase and at the same time the SH increases over 35 °C. Studies performed by several authors (see as example Schlager et al. [1990], Biancardi et al. [1996] and Cremaschi et al. [2005]) and ECS manufacturers experience show that low pressure and high temperature at the evaporator outlet negatively perturbs the oil circulation and thus negatively affects the life of the compressor.

This issue is mitigated creating a dummy thermal load on the evaporator. This additional load is obtained injecting hot R134a at the evaporator inlet just after the expansion valve. A pneumatic valve is installed to modulate the hot gas injection (i.e. a Danfoss CPCE).

The by-pass line keeps the suction pressure at 200 kPa reducing at the same time the SH and the compressor discharge temperature ($T_{out,comp}$). The introduction of the line and of the additional valve does not compromise the stability of the system (only a small oscillation is present when the aircraft reaches the cruise altitude). A COP reduction counterbalance all the advantages of the by-pass (see figure 6.8(b)).

The $T_{out,comp}$ still rises over 120 °C during the mission. Most of the oils used for HVAC applications starts to degrade over 120 °C: low time exposure is a marginal risk, but continuous exposure at high temperature compromises the oil properties reducing the lubrication effect and thus the life of the compressor.

The liquid R134a exits from the condenser can be used to cool down the R134a at the compressor inlet. An electronic valve modulates the flow rate on the liquid injection line which connects the condenser outlet with the

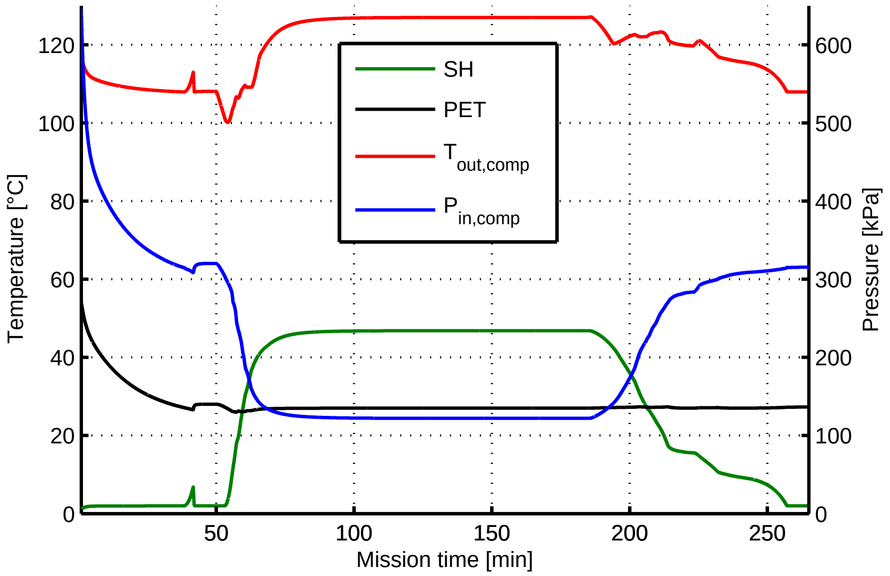

(a) Temperatures and pressure

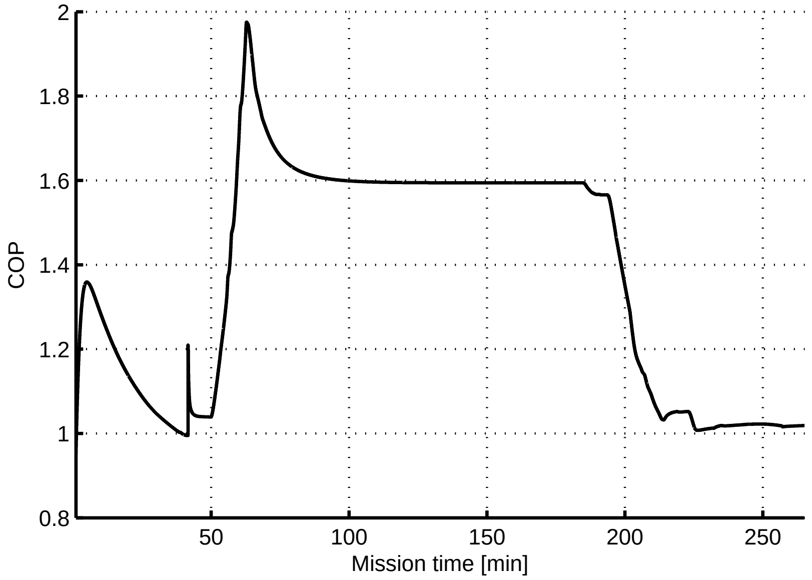

(b) COP

Figure 6.7: Standard VCS behavior

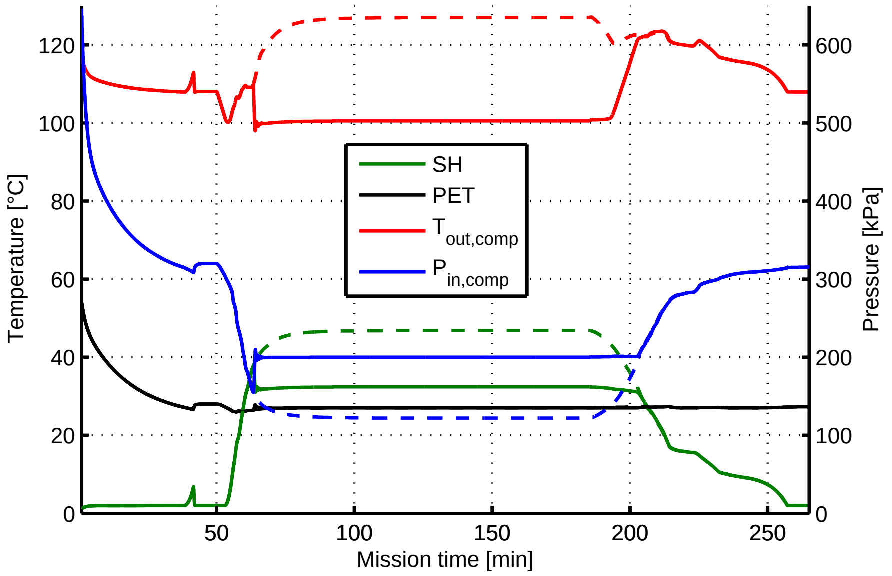

(a) Temperatures and pressure

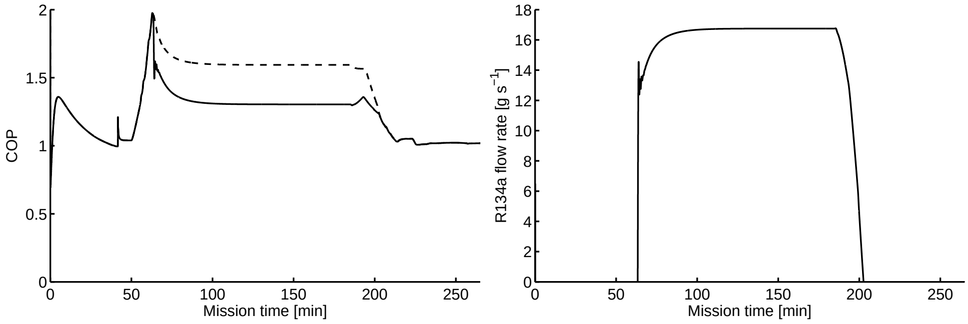

(b) COP **(c)** by-pass line R134a flow rate

Figure 6.8: Behavior of the VCS with bypass line. The dashed lines show the trends that are reported in figure 6.7

compressor inlet: when the compressor discharge temperature rises over 110 °C the valve opens, injecting cold R134a at the compressor inlet and so limiting the compressor discharge temperature.

Figure 6.9(c) shows the R134a flow rate through the liquid injection line during the mission. The liquid injection line is progressively opened during the descent phase when the SH is still high (low thermal load) but the suction pressure is above the minimum threshold and so the by-pass line is closed. The valve limits the compressor discharge temperature peak; the opening of the liquid injection line does not change neither the COP (figure 6.10(b)) nor the performance of the system (figure 6.9(c)): the EXV compensates the liquid line injection reducing the target SH.

6.3.2 Variable compressor displacement

In the previous paragraph the behavior of a system equipped with a fixed displacement compressor has been analyzed; the use of an EXV combined with other technical solutions allows a good control of the PET also if the thermal load is low. However the COP remains at low level even during the cruise phase at low OAT.

The cruise phase is the longer flight phase and so the reduction of the electrical power drained by the generators during this phase bring great advantages in terms of fuel consumption (see equation (5.6.2) for the fuel penalty due to electrical power consumption).

The VCS is equipped with a large compressor to provide enough cooling when the aircraft is on ground, but a compressor with a smaller displacement is certainly sufficient during all the rest of the mission. This approach suggests the use of a variable displacement compressor.

The displacement of a compressor is controlled or changing the rotational speed of the compressor or changing the piston stroke. The first solution is compatible with all the compressor types (screw, scroll, piston, etc.) while the second one is feasible only using a wobble-plate compressor. Since the first approach is applicable to a wider selection of compressor than the first one, the use of a variable speed motor/compressor has been studied.

Figure 6.5 shows the VCS architecture. An EXV still controls the SH, while all other tricks discussed in the above paragraph are not incorporated. A variable speed motor drives the compressor; the motor speed can be set from 400 rpm to 3500 rpm. The lower speed of the motor is not set to 0 rpm to assure a minimum R134a flow rate and especially a minimum oil flow rate through the compressor. The EXV is set to maintain a SH of 2 °C.

The compressor works at the maximum displacement during the pull down. There is a small speed reduction just before the boarding of the passengers, but the additional heat load generates a fast motor acceleration back to the maximum speed. As soon as the OAT decreases (climbing phase) the COP rises up (better condenser performance), the control logic progressively

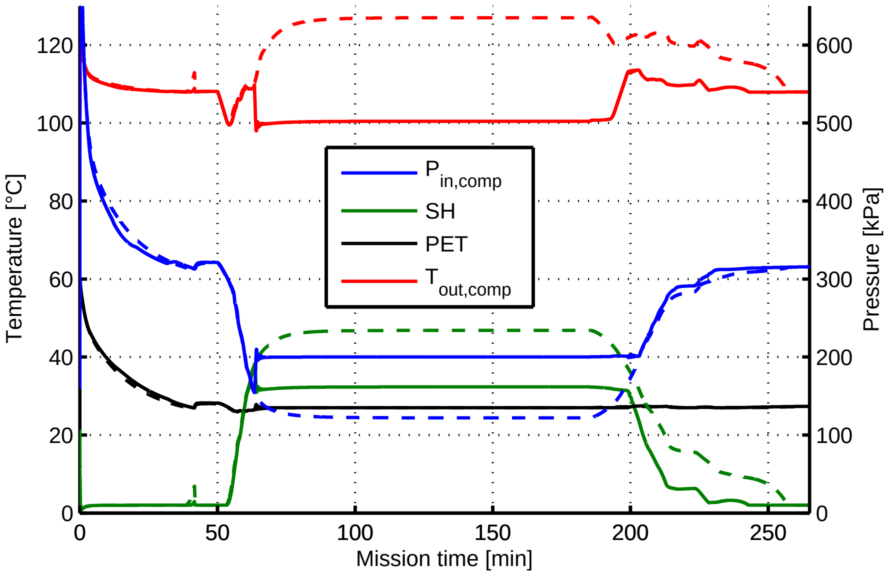

(a) Temperatures and pressure

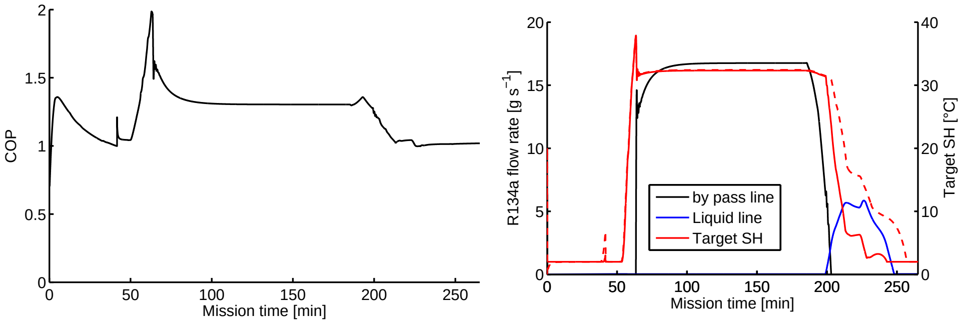

(b) COP

(c) by-pass line R134a flow rate

Figure 6.9: Behavior of the VCS with bypass line and liquid injection line. The dashed lines show the trends that are reported in figure 6.8

reduces the speed of the compressor modulating the cooling capacity of the system without impacting the COP.
This cooling capacity control is very interesting since is able either to minimize the electrical power consumption of the system during the flight phases and to provide all the needed cooling capacity when it is required[2].

6.3.3 Operation at low Δ_{ISA}

In the cruise phase the speed of the compressor arrives near to the minimum allowed. Figure 6.11 shows the limits of this architecture: at low Δ_{ISA} this architecture is not able to maintain the target temperature (too high cooling capacity).
The working envelope of the system can be expanded incorporating the heating sub-system. The heating function is done on small unpressurized aircraft using electrical heaters, while on bigger aircraft (especially if they are pressurized) some air is bled from the engines and blown into the compartment. A small plate and fins HX is used to cool down the air to acceptable levels[3]. The bleed air flow rate can be modulated to increase or decrease the cabin heat load, controlling the compartment temperature. Generally the best place to inject the hot air is between the evaporator fan and the evaporator.
The behavior of the proposed architecture is studied utilizing the usual mission profile; in this case only the Δ_{ISA} is fixed to $-10\,^{\circ}\mathrm{C}$. The model assumes that the bleed air enters into the compartment at a temperature of $50\,^{\circ}\mathrm{C}$ and the bleed flow rate range is from $61.6\,\mathrm{g\,s^{-1}}$[4] to $200\,\mathrm{g\,s^{-1}}$.
The VCS works at low speed when the aircraft is on ground, but it is still able to control the compartment temperature. During the climbing phase compressor speed reaches the minimum allowed and the bleed air control valve starts to open increasing the bleed air flow rate into the compartment. The temperature is well controlled during the cruise phases thanks to the use of the bleed air. The bleed air flow rate returns to the minimum value at the end of the descent phase, the compressor slightly accelerate to increase a little bit the cooling capacity when the aircraft touches again the ground. The injection of the bleed air just before the evaporator creates an additional heat load to the evaporator and so it helps to avoid low suction pressure issues. The integration of the cooling sub-system and the heating sub-system has also the benefit to create a smooth transition between the full heating mode (VCS switched off) and the full cooling mode (bleed flow rate set to the minimum[5].

---

[2] Please note that the use of a wobble-plate compressor externally or internally controlled will have the same advantages of the compressor speed modulation since both the methods acts on the m_{R134a}

[3] civilian regulation limits the temperature of the air entering into passenger compartments to $70\,^{\circ}\mathrm{C}$

[4] $5.6\,\mathrm{g\,s^{-1}}$ for each occupants, see section 4.2.11

[5] the minimum is generally set to respect the minimum fresh air requirement imposed

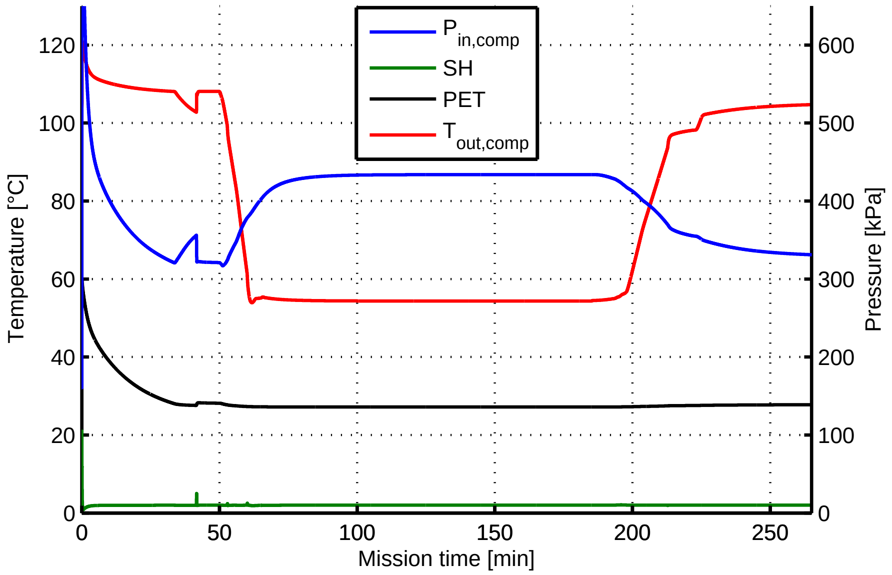

(a) Temperatures and pressure

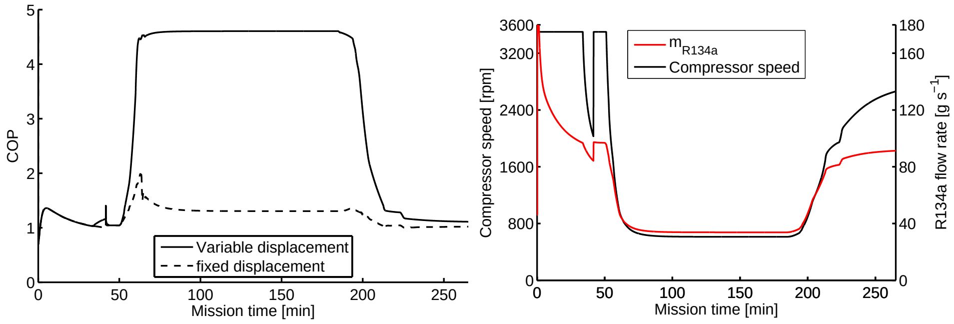

(b) COP **(c)** by-pass line R134a flow rate

Figure 6.10: Behavior of the VCS with variable displacement compressor. The dashed line shows the trends that are reported in figure 6.9

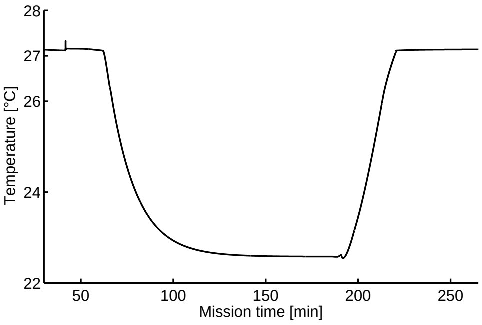

Figure 6.11: Behavior of the VCS with variable displacement compressor at Δ_{ISA}=−10 °C

6.4 Electronic cooling system

The thermal load of the passenger compartments is linked to the *OAT*, generally speaking at low *OAT* there is no need of any cooling system. The electronic generates a thermal load which is not dependent from the *OAT* and so there is always the need of use a cooling system to control the temperature of the electronic components. The electronic thermal load can rapidly change during a mission (i.e. RADAR switching off), and the cooling system shall be able to operate in a wide range of thermal load even at low condensing temperatures.

The variable displacement architecture is the best in terms of COP, but it needs some additional features to manage extremely low thermal loads. In the case of passenger compartments, the use of the bleed air permits to control the low thermal loads without switching off the compressor, on electronic cooling the bleed air is generally not available. When the compressor reaches the minimum allowed displacement the target SH of the EXV can be increased to further decrease the cooling capacity of the system.

This approach philosophy has been verified on the usual mission profile ($\Delta_{\mathrm{ISA}} = -15\,°\mathrm{C}$), removing the electronic thermal load for 30 min as soon as the aircraft reaches the cruise altitude. A minimum thermal load is still present due to electrical components of the system (liquid pump, evaporation fan).

The pull down is done providing the maximum cooling capacity then, when the target temperature of the electronic load is achieved (30 °C), the compressor speed is reduced. The compressor progressively slows down during the climbing phase controlling the electronic temperature without modify the SH setting. The SH setting is increased when the heat load is removed; the compressor displacement reduction is not sufficient to control the temperature, and the target SH is increased to decrease the cooling capacity

---

by the civilian regulations

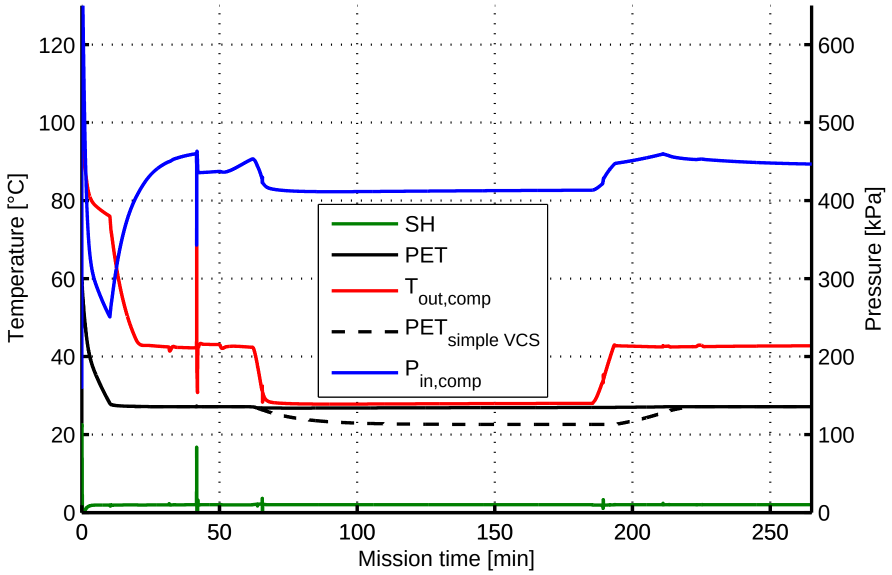

(a) Temperatures and pressure

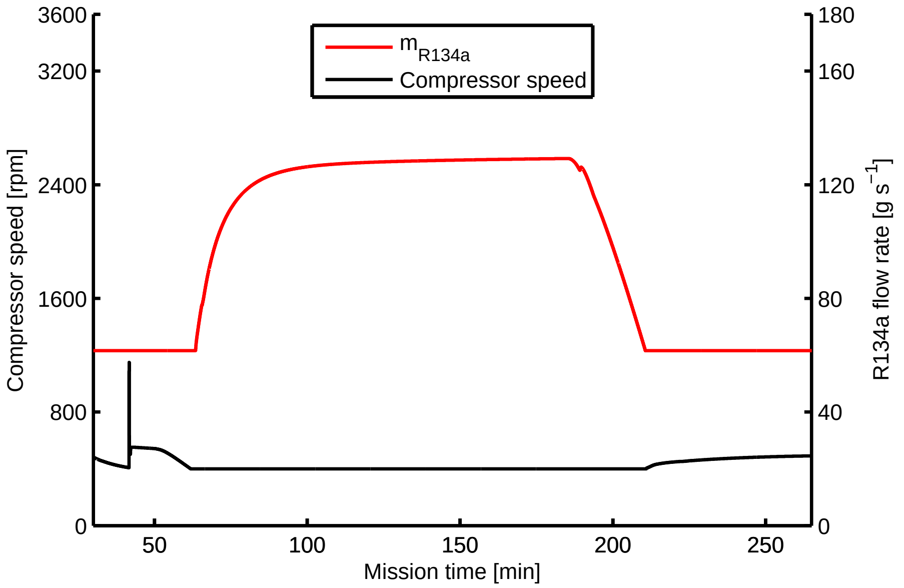

(b) by-pass line R134a flow rate

Figure 6.12: Behavior of the VCS with variable displacement compressor and integrated heating sub-system at $\Delta_{ISA}=-10\,°C$. The dashed line shows the trends that are reported in figure 6.11

of the VCS. There are some oscillation due to the EXV action, but this transient does not generate any dangerous operation condition. The EXV action keeps the electronic load temperature within 1 °C from the setting point. The low R134a flow rate is sufficient to avoid high compressor discharge temperatures.
The SH returns rapidly to the minimum allowed value (2 °C) when the load is restore, since the modulation of the compressor displacement is sufficient to control the electronic load temperature.

6.5 Operations at extreme low condensation temperatures

There are case where the compartment thermal load is still positive also at very low *OAT* (see section 4.3.2, or electronic cooling), in these cases the VCS operates at very low condensing temperatures (down to −32 °C) and the cycle risks to collapse (suction pressure equal to discharge pressure).
A variable speed condenser fan solves this issue. The VCS controller modulates the speed of the fan, closing the control loop on the compressor discharge pressure; the reduction of the condenser air flow rate implies a drop of the condenser performance (heat rejected), thus an increase of the compressor discharge pressure.
Generally a valve is also installed between the compressor and the condenser as secondary device to avoid the drop of the compressor discharge pressure. This valve (i.e. a KVR Danfoss valve) opens upon a rise in pressure on the compressor side, when the pressure at the compressor outlet reaches the minimum allowed value (in the simulations 700 kPa) the valve closes increasing the pressure drop on the line and so keeping stable the compressor outlet pressure. The valve is set to maintain a minimum discharge pressure which is lower than the threshold set on the controller, so it works only in case of an issue on the main device (the condenser fan).
The compressor discharge pressure influences the COP: high discharge pressure means high power consumption and so low COP. The figure 6.13 shows the comparison between a mission with a minimum discharge pressure set to 800 kPa and the same mission profile with a minimum discharge pressure of 1000 kPa (the simulations are base on a variable speed compressor architecture). The influence of the discharge pressure on the COP is clearly visible during the cruise phase (this is the phase where the control operates): a reduction of the 20 % of the discharge pressure bring an increase of the COP around the 26 %.

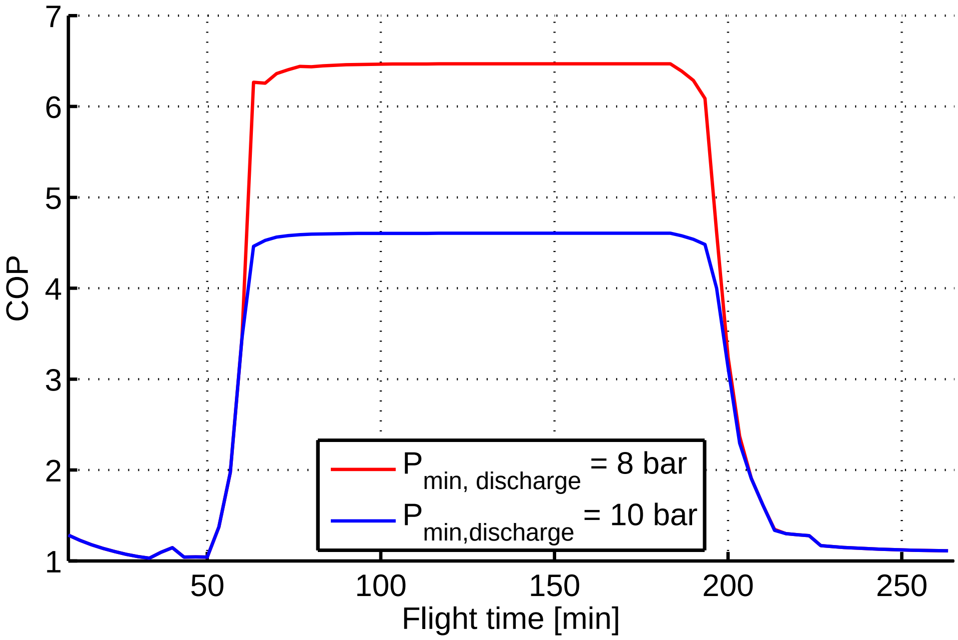

Figure 6.13: COP comparison at different minimum discharge pressures

Chapter 7

Conclusions

The inline pneumatic valves are widely used to regulate the subsystems which uses air bled from the engine; there is a lack of information in literature on those key components since almost of the knowledge is based on the experience of valve manufacturers. A detailed mathematical model of the inline pneumatic valves has been created and discussed; the model uses the fundamental thermodynamic and mechanical differential equations to simulates the dynamic behavior of the valves. A test campaign has been conducted with the aim of validate the valve model; the test rig was characterized by three high frequency pressure sensors able to measure the fast response of the valve (in some cases the response time is lower than 0.5 s). The mathematical model results match the experimental results within the experimental uncertainty, demonstrating the goodness of the developed model.

The developed and validated model has been used to study the behavior of the valve and its subcomponents. The effects of the air pressure and temperature on the relief valve cracking point are described and then propagated to the whole valve model; the substitution of the relief valve with a proportional solenoid to eliminate the air pressure and temperature effects has been analyzed and the benefits highlighted. The model predicts a valve instability if the valve upstream pressure and valve downstream pressure ratio is too high. The model clearly pointed out the reason of instability and the proposed piston shape (trapezoidal) rises the maximum operating pressure of the valve.

The air bled from the engine is still used to warm up the leading edge of nacelles and wings, since this approach is the most reliable ones. Three different architectures of anti-ice system are presented and their performance simulated (using the valve model created), with particular attention to the impacts on the fuel consumption of the aircraft. An active control of the leading edge temperature, performed using a valve equipped with a proportional solenoid, cuts the fuel consumption due to the anti-ice system of the 40 % during the takeoff phase and of the 30 % in the descent phase. The active control has also the advantage of reduce the leading edge temperature allowing the use of lighter materials.

Another key components for the bleed air circuit are the plate and fins compact heat exchangers. This family of heat exchangers is a subject of the scientific research since a long time. The Kays and London [1984] is still the starting point for each engineer who approach this world. Also for the compact heat exchangers a mathematical model able to predicts the performance of the unit has been created. The model is based on the approach proposed by Kays and London [1984], improving the developed models including some neglected aspects of the real construction of the heat exchangers have been introduced (i.e. blocking bars, end plates) and some empirical correlations for the wavy fins. Some tests have been performed to verify the performance of the model, in particular three different heat exchangers have been tested. The mathematical model is able to predicts the performance of the heat exchangers with a confidence suitable for almost the industrial applications.

A 0d dynamic thermal model of an airplane is explained and used into the simulation of the Environmental Control Systems. The model shows that even at low Outside Air Temperatures the compartment heat load could be positive requiring the intervention of the cooling system to maintain the temperature inside the desired range.

All the aforementioned models have been introduced in a mathematical model of a whole Environmental Control System. The first architectures analyzed are based on the reverse Brayton-Joule cycle. The behavior of a standard bootstrap cycle is presented and used to determine the areas of improvement. A new control strategy based on a valve installed in series to the air cycle machine allows to preserve the efficiency of the cycle also in case of low heat loads; the simulations performed on a system used to cool down the aircraft electronic highlighted a limitation in the use of this technique, linked to some instability phenomena of the valves. To improve the efficiency of a reverse Brayton-Joule cycle, the system has to be independent from the engines: this is the bleedless approach. This revolutionary approach, already used on the Boeing 787, uses an auxiliary compressor to compress the air for the Environmental Control System. The impacts of these approach on the aircraft fuel consumption has been analyzed proposing the use of a variable speed compressor to modulate the cooling capacity of the system: the fuel penalty of a bleedless system is the 45 % lower than the fuel penalty of a standard air cycle.

The study of the Environmental Control Systems for aircraft ends with the analysis of the Vapor Cycle Systems. The Vapor Cycle System analyzed is equipped with a variable speed condenser fan to control the condensation pressure at low Outside Air Temperature, and with an Electronic Expansion Valve to control the cooling capacity of the system. The effects of the introduction of two pneumatic valves to avoid unsafe compressor working conditions (low suction pressure and high discharge temperature) have been analyzed. The valves marginally negatively affect the Coefficient Of Performance of the cycle, but are able to avoid the continuous switching on and off of the compressor also in low heat load conditions (cruise phase). A variable displacement compressor (variable speed motor or wobble plate piston compressor) is the best solution to control the cooling capacity of the system maximizing the Coefficient Of Performance during the cruise phase. The coupling of a variable displacement compressor with the heating sub-system allows the system performance also in case of low Outside Air Temperature. In case that the Vapor Cycle System is used to cool some electronics, the simulations shows that use of a variable speed compressor has to be coupled with a variable Superheating control strategy to avoid the compressor switching off in case that all the electronic thermal load is removed.

Bibliography

B.W. Andersen. *The Analysis and Design of Pneumatic Systems.* Krieger, 2001.

ASHRAE. *1987 ASHRAE handbook - Heating, ventilating, and air-conditioning systems and applications.* American Society of Heating, Refrigerating and Air-conditioning Engineers, Incorporated, 1987.

ASHRAE. *ASHRAE Handbook.* American Society of Heating, Refrigerating and Air-conditioning Engineers, Incorporated, 1997.

P. Asinari. Finite-volume and finite-element hybrid technique for the calculation of complex heat exchangers by semiexplicit method for wall temperature linked equations (sewtle). *Numerical Heat Transfer, Part B: Fundamentals*, 45(3):221–248, 2004.

Ilan Berlowitz. All/more electric aircraft engine & airframe system implementation. In *the 9th Israeli Symposium on Jet Engines and Gas Turbines*, October 2010.

John J. Bertin. *Aerodynamics for engineers.* Prentice Hall, Upper Saddle River, NJ 07458, 4^{th} edition, 2002. ISBN 0-13-064633-4.

F.R Biancardi, Michels H.H., T.H. Sienel, and D.R. Pandy. Study of lubricant circulation in hvac systems. description of technical effort and results. Utrc technical report, United Technologies Research Center, East Hartford, CT., 1996.

V. Bianco, O. Manca, S. Nardini, and M. Roma. Numerical invesxtigation of transient thermal and fluidynamic fields in an executive aircraft cabin. *Applied Thermal Engineering*, 29(16):3418 – 3425, 2009.

C. Bonacina, A. Cavallini, and L. Mattarolo. *Trasmissione del calore.* CLEUP, Padova, Italy, 3^{rd} edition, 1989. ISBN 88-7178-20-2.

Y. Chen, N.P. Halm, J.E. Braun, and E.A. Groll. Mathematical modeling of scroll compressors - part ii: Overall scroll compressor modeling. *International Journal of Refrigeration*, 25(6):751–764, 2002a.

Y. Chen, N.P. Halm, E.A. Groll, and J.E. Braun. Mathematical modeling of scroll compressors - part i: Compression process modeling. *International Journal of Refrigeration*, 25(6):731–750, 2002b.

L. Cremaschi, Y. Hwang, and R. Radermacher. Experimental investigation of oil retention in air conditioning systems. *International Journal of Refrigeration*, 28(7):1018–1028, 2005.

Y. Epstein and D.S. Moran. Thermal comfort and the heat stress indices. *Industrial Health*, 44(3), 2006.

Alison B Evans. The effects of compressor seventh-stage bleed air extraction on performance of the f100-pw-220 afterburning turbofan engine. Contractor Report-Final CR-179447, NASA, February 1991.

FAA. *Code of Federal Regulations, Title 14 - Aeronautics and Space.* Division of the Federal Register, 2012.

P.O. Fanger. *Thermal Comfort, Analysis and Applications in Environmental Engineering.* McGraw-Hill, 1972.

Claudio Garcia. Comparison of friction models applied to a control valve. *Control Engineering Practice*, 16(10):1231 – 1243, 2008.

R. J. Goldstein, A. I. Behbahani, and K.K. Heppelmann. Streamwise distribution of the recovery factor and the local heat transfer coefficient for an impinging circular jet. *Heat mass transfer*, 1986.

John H Henninger. *Solar absorptance and thermal emittance of some common spacecraft thermal-control coatings.* Number 1121 in NASA reference publication. NASA Scientific and Technical Information Branch, Washington, D.C., April 1984.

Liu HHT and J. Hua. Three-dimensional integrated thermodynamic simulation for wing anti-icing system. *Journal of Aircraft*, 41(6):1291–1297, 2004.

ICAO. Manual of the ICAO standard atmosphere (extended to 80 kilometres (262 500 feet)). Doc 7488-CD, 1993.

W.P. Jones. A review of cibse psychrometry. *Building Ser. Eng. Res. Technol.*, 15(4):189–198, 1994.

JSSG-2009. *Department of defense joint services specification guide: air vehicle subsystems.* US Department of Defense, October 1998.

S. Kato. Solution for aircraft anti-icing system simulation by a modified perturbation method. *Journal of Aircraft*, 43(2):544–54, 2006.

W.M. Kays and A. L. London. *Compact Heat Exchanger.* Krieger, Malabar Florida 32950, 3^{rd} edition, 1984. ISBN 1-57524-060-2.

SJ Kline and FA McClintock. Describing uncertainties in single-sample experiments. *Mechanical engineering*, 75:3–8, January 1953.

G. Kopp and J. L. Lean. A new, lower value of total solar irradiance: Evidence and climate significance. *Geophysical Research Letters*, 38:1706, jan 2011.

M. Kühn, J. Bosbach, and C. Wagner. Experimental parametric study of forced and mixed convection in a passenger aircraft cabin mock-up. *Building and Environment*, 44(5):961 – 970, 2009.

E.W. Lemmon, M.L. Huber, and M.O. McLinden. Nist standard reference database 23: Reference fluid thermodynamic and transport properties-refprop, version 9.0. National Institute of Standards and Technology, Standard Reference Data Program, Gaithersburg,, 2010.

LMS Imagine S.A. *AMESim® User's Guides*, 2012.

S. Martínez-Ballester, J.-M. Corberán, J. Gonzálvez-Maciá, and P.A. Domanski. Impact of classical assumptions in modelling a microchannel gas cooler. *International Journal of Refrigeration*, 34(8):1898–1910, 2011.

S. Martínez-Ballester, J.-M. Corberán, and J. Gonzálvez-Maciá. Numerical model for microchannel condensers and gas coolers: Part i - model description and validation. *International Journal of Refrigeration*, 2012a.

S. Martínez-Ballester, J.-M. Corberán, and J. Gonzálvez-Maciá. Numerical model for microchannel condensers and gas coolers: Part ii - simulation studies and model comparison. *International Journal of Refrigeration*, 2012b.

Jeanne G. Mason, J. Walter Strapp, and Philip Chow. The ice particle threat to engines in flight. In *44th AIAA Aerospace Sciences Meeting and Exhibit*, January 9-12 2006.

Kaviany Massoud. *Principles of convective heat trasfer.* Mechanical Engineering. Springer, New York, 2 edition, 2001. ISBN 0-387-95162-8.

MIL-E-18927E. *Military specification: Envitonmental Control Systems, aircraft, general requirements for.* US Department of Defense, August 1983.

MIL-HDBK-310. *Global Climatic Data for Developing Military Products.* US Department of Defense, 1997.

MIL-STD-1472G. *Department of defense design criteria standard: human engineering.* US Department of Defense, January 2012.

MIL-STD-210-C. *Climatic information to determine design and test requirements for military systems and equipment.* US Department of Defense, 1987.

I. Moir and A. Seabridge. *Aircraft Systems: Mechanical, Electrical and Avionics Subsystems Integration.* Aerospace Series. Wiley, 2008. ISBN 9780470059968.

J. Michael Muhm, Paul B. Rock, Dianne L. McMullin, Stephen P. Jones, I.L. Lu, Kyle D. Eilers, David R. Space, and Aleksandra McMullen. Effect of aircraft-cabin altitude on passenger discomfort. *New England Journal of Medicine*, 357(1):18–27, 2007.

National Engineering Laboratory. *physical properties of water and steam,* 0-800 °C*,* 01000 bar. H.M.S.O., 1964.

Richard D. Neumann and Delma C. Freeman. The experimental measurement of aerodynamic heating about complex shapes at supersonic mach numbers. In *Thermal amd Fluids Analysis Workshop (TFAWS 2011).* NASA, January 2011.

SH. Nunneley and F. Stribley. Fighter index of thermal stress (fits): guidance for hot weather aircraft operations. *Aviation, Space, and Environmental Medicine*, 50(6), 1979.

Liping Pang, Jie Xu, Lei Fang, Mengmeng Gong, Hua Zhang, and Yu Zhang. Evaluation of an improved air distribution system for aircraft cabin. *Building and Environment*, 2012.

M. P. C. Pellissier, W. G. Habashi, and A. Pueyo. Optimization via fensap-ice of aircraft hot-air anti-icing systems. *Journal of Aircraft*, 48(1):265–276, 2011.

SAE-AIR-1168/3. *Aerothermodynamic Systems Engineering and Design.* SAE aerospace, 2004.

SAE-AIR-1168/8. *Aircraft Fueel Weight Penalty Due to Air Conditioning.* SAE aerospace, 2004.

L.M. Schlager, M.B. Pate, and A.E. Bergles. Oil quantity measurements in smooth and micro-fin tubes during evaporation and condensation of refrigerant-oil mixtures. Number pt 2, pages 465–469, 1990.

K. Ramesh Shah and P. Sekulić Dušan. *Fundamentals of heat exchanger design.* John Wiley & Sons, 1^{st} edition, 2003. ISBN 0-471-32171-0.

A. Spazian. Experimental and numerical analysis of a scroll compressor in an economized cycle for aeronautic applications. Master thesis, University of Padova, 2009.

A. Wadcock, L. Ewing, E. Solis, M. Potsdam, and G. Rojagopalan. Rotorcraft downwash flow field study to understand the aerodynamics of helicopter brownout. In *AHS Southwest Region Technical Specialists*. NASA, October 2008.

B. Wang, X. Li, and W. Shi. A general geometrical model of scroll compressors based on discretional initial angles of involute. *International Journal of Refrigeration*, 28(6):958–966, 2005.

P. Wendling et al. Aerosol radiation interaction in the cloudless atmosphere during lace 98 2. aerosol-induced solar irradiance changes determined from airborne pyranometer measurements and calculations. *Journal of geophysical research*, 107:8131, 2002.